2013

Low Velocity Impact Behavior and Modeling of Loose-Knit Polymer Composite Materials

Jeremy Payne
Lehigh University

Low Velocity Impact Behavior and Modeling of Loose-Knit Polymer Composite Materials

Jeremy Payne

A Dissertation

Presented to the Graduate and Research Committee of

Lehigh University

In Candidacy for the Degree of

Doctor of Philosophy

Mechanical Engineering

Lehigh University

Bethlehem, PA

May, 2013

LEHIGH UNIVERSITY

Bethlehem, Pennsylvania

_____

Approved and recommended for acceptance as a dissertation in partial fulfillment of the requirements for the degree of Doctor of Philosophy.

_____	_____
Defense Date	**Herman F. Nied, Ph.D.** **Dissertation Advisor**
_____	
Accepted Date	**Committee Members**
	_____
	D. Gary Harlow, Ph.D.
	_____
	John Coulter, Ph.D.
	_____
	Raymond Pearson, Ph.D.

Acknowledgements

I would like to thank Professor Herman Nied for his insight and support during my graduate school career. His guidance made it possible to push through to accomplish the goals set forth. The rest of my committee, Professors D. Gary Harlow, John Coulter and Raymond Pearson also deserve recognition for always providing assistance when called upon.

I would also like to thank Tammy Yang from GAF for her input and support throughout the modeling portion of this project. She provided invaluable insight into the commercial roofing industry as well as assistance with material testing facilities, techniques and results.

Next, I would like to thank the Department of Mechanical Engineering, as well as GAF, for their financial support during my studies. Without this support I would have not been able to continue on with my education to this point.

Finally, I need to thank my family members, close friends, and fiancée who have been with me throughout my educational endeavors. Without their love and support this journey would have been far too difficult.

Contents

List of Figures

List of Tables

Abstract

An investigation into knitted reinforced polymer composites was performed with emphasis on the impact behavior associated with this material type. Overviews of knitting terminology and some applications available for knitted reinforced polymer composites are presented. Impact performance characteristics are examined with emphasis on testing and evaluation techniques available. Large deformation behavior was observed in testing and modeling areas with elastomeric polymer materials being the main subject of discussion. This allowed the knitted fabric reinforcement to be taken advantage of in these "flexible composites."

An impact test rig was created in order to analyze the performance of two different types of knitted reinforced polymer composite material, with emphasis on a commercially available product due to its availability. The test setup will be discussed in great detail and will be based on designs found in the literature. Post impact analysis will be performed based on techniques outlined in the literature with examination of the permanent deformation and energy absorbing capabilities of the materials tested.

Through an industrial partnership program, a large scale finite element model was created in order to examine the wind uplift performance of a commercial roofing application. This model will be created in a multi-level fashion from micro-scale to macro-scale in order to examine the effects each of the constituents has on

the overall performance of the composite membrane. Material property testing and curve fit capabilities will be employed in order to create the material models used in the finite element simulations. Comparisons between experimental tests and simulation results will show good agreement between the two, allowing for validation in potential usage of the model for predictive based purposes in order to provide recommendations for best changes to the material to explore further.

1 Introduction

In recent years, the use of polymer composite materials to replace heavier metal parts has been of increasing interest due to weight, reliability and cost concerns. These polymer composites are used in a variety of industries and applications including transportation (automobiles, aircraft, ships, and spacecraft), sporting goods, medical, and construction industries. In almost all of these industries susceptibility and resistance to impacts is of the utmost concern. This study will explore some of the applications of polymer composites as well the designs and procedures involved in the study of impact responses and other performance related analyses. Also included will be an in-depth examination of a particular application in the commercial construction industry thanks to an industrial partnership with GAF.

In general terms, a composite is a multiphase material comprised of two or more distinct materials that by the principle of combined action result in possession of a better combination of the physical properties of each of its constituents [1]. Furthermore, many composites consist of two phases: a matrix, which is continuous and surrounds the other phase often called the dispersed phase. Some of the more common forms of composites used in engineering include, but are not limited to, Metal Matrix Composites (MMCs), Ceramic Matrix Composites (CMCs) and Polymer Matrix Composites (PMCs). In the case of PMCs, the matrix is a polymer of some variety while the dispersed phase is often a fiber or particle reinforcement. Moving

forward, MMCs and CMCs will not be involved in the scope of this paper. Breaking polymer composites down further, a common classification scheme involves the examination of a polymer's response to rising temperature, which is categorized into thermoplastic and thermoset polymers. Thermoplastic polymers soften when exposed to rising temperatures and will harden when cooled. This process is totally reversible and can be repeated, allowing thermoplastics to be recycled. At a molecular level, the increased action and movement in the polymer chains causes a weakening of the secondary bonding forces allowing the polymer to be formed and molded. However, there is a limit to this action, which occurs at a temperature where the molten polymers molecular vibrations become energetic enough that primary covalent bonds break, resulting in irreversible degradation of the original material properties. Most forming techniques for thermoplastic polymers involve the use of both heat and pressure in order to achieve the desired shape. On the other hand, thermosetting polymers harden permanently when cured and remain in that state, and will not soften due to re-application of heat except for extreme temperatures. During the heat application process of the thermosetting polymers, covalent crosslinks are formed between adjacent molecular chains [1]. This prevents any movement of the polymer chains, resulting in generally harder and stronger polymers than their thermoplastic counterparts.

1.1 Organization of the Dissertation

This introductory chapter will include a literature survey overviewing polymer reinforced composites with a more in-depth examination of knitted reinforcement applications including explanations of knitting based terminology, processing issues and other unique characteristics. The following chapter will examine impact performance characterization information regarding techniques available, evaluation techniques and an examination of how the constituents of the composites affect the performance of the materials. Chapter 3 will provide background information for the formulation of the problems to be discussed including an overview of finite element definitions.

The next chapter will include the explanations of the setup of the impact testing rig, data acquisition system and the results obtained through the impact tests. Different materials will be analyzed with post impact analysis techniques including those outlined in Chapter 2. The final chapter will outline a specific knit reinforcement application through an industrial partnership program that includes the creation of a finite element model for analyzing the wind uplift performance of commercial roofing materials.

1.2 Literature Survey

As mentioned above, one such area where polymer composite materials are being explored is in the medical field [2–4]. Ramakrishna, *et al.* [2] explore the use of thin

and flexible composites for use as soft tissue replacements. Using a bio-tolerant elastomer, the group set out to examine the effects of using a pre-stretched knitted material. The concept of pre-stretching will be explored in greater detail in the following section. A review provided by Leong, *et al.* [4], reference the capability of using knitted composites for the use in the creation of prosthetics due to the ease of forming inherit in the structures of knitted materials. These forming capabilities will again be discussed in further detail in the following sections. In a somewhat related study, Wu, *et al.* [3] examined the feasibility of creating a self-healing polymeric structure for use in biological applications. This would eliminate the need for any repairs that might be necessary as the implants wear down over the years of usage. The self-healing nature however would not be limited to the medical field as more studies are finding the implications of damage to the matrix of a polymer composite can greatly impact its performance. Wu goes on to examine the recovery abilities of the self-healing materials whose recovery actions can be activated either autonomously or through some sort of external stimulus such as the application of heat or radiation. This healing power can be beneficial not only due to impact or cyclic loading induced damage, but also damage caused by the insertion of sensors, manufacturing processes and fiber de-bonding. Ratios of fracture stress, elongation at break and fracture energy are among the parameters used in order to evaluate the extent of healing that occurs in the composites.

A variety of healing techniques for thermoplastic materials were overviewed including molecular interdiffusion, which involves holding two pieces of the same polymer above their glass transition temperature, T_g, until the interface between the separate materials gradually disappears due to the interdiffusion of polymer chain segments. Another healing mechanism discussed was photo-induced healing which involved the use of a photochemical reaction. The issue with this technique is the limitations of the method that prevent light from reaching internal cracks, especially in thick substrates. Several other catalyst based reactions for thermoplastics were discussed in great detail, as well as a few techniques for thermoset repairs, such as nanoparticle deposits and *in situ* healing agent introductions, but these healing methods are further out of the scope of this paper.

Another area that composites are of growing interest is in the realm of civil transportation [5–9]. Replacing certain components of vehicles with lighter weight composite materials will allow for increased fuel efficiency as well as lower cost of maintenance for the life of vehicles, including bus structures and portions of high-speed railway coaches and locomotives. Ning [5,8] was involved in two such studies in which components of a mass transit bus were replaced with designs employing composite materials, while Zinno, *et al.* [6] examined a similar situation but for railway vehicles. In all three of these studies, the material choices and manufacturing techniques were explored in great detail. For both studies involving Ning [5,8], the emphasis was placed on the benefits of thermoplastic composites

versus other materials including aluminum, steel and thermoset composites due to its superior impact resistance, ease of shape and recycling among a variety of additional benefits. An additional benefit to take note of is the potential that thermoplastics possess to maintain their integrity post-impact due to the fact that they do not exhibit the catastrophic type of failures seen in other materials.

One of the more prevalent designs in the manufacturing of composite panels is the sandwich structure [6,9–12]. These structures are comprised of polymeric skins enveloping a foam core, which is used to increase the panel's moment of inertia, thereby increasing its bending stiffness. These structures are fairly complex and can present some difficulty in the design phase due to the difficulty in taking all failure modes and structural complexity into consideration. The two main sub-categories for the foam structures are often considered to be the solid core design, where a single rigid piece of foam as seen in [10] and a honeycomb structure seen below from [6].

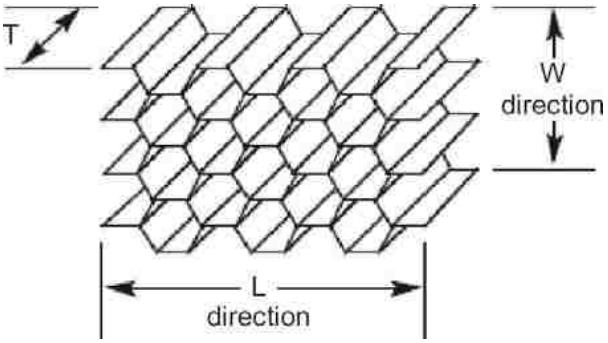

Figure 1-1 - Honeycomb Core Design [6]

In addition to the use of the foam core, additional reinforcement measures are often times employed. Torre and Kenny [9] offer an interesting take on this by using the same polymeric material to introduce a corrugated support system within the foam core. This reinforcement system is fairly unique in that the orientation of the sandwich structure (180° changes) will change its performance in the situation where impact resistance is concerned. The testing and results of involving this design will be discussed in greater detail in a later section. One important item to note from [9] is the discussion of the loading rate dependency that sandwich materials possess. While the structures may behave in a fairly ductile manner while in static loading, catastrophic failure can occur when impact loadings occur.

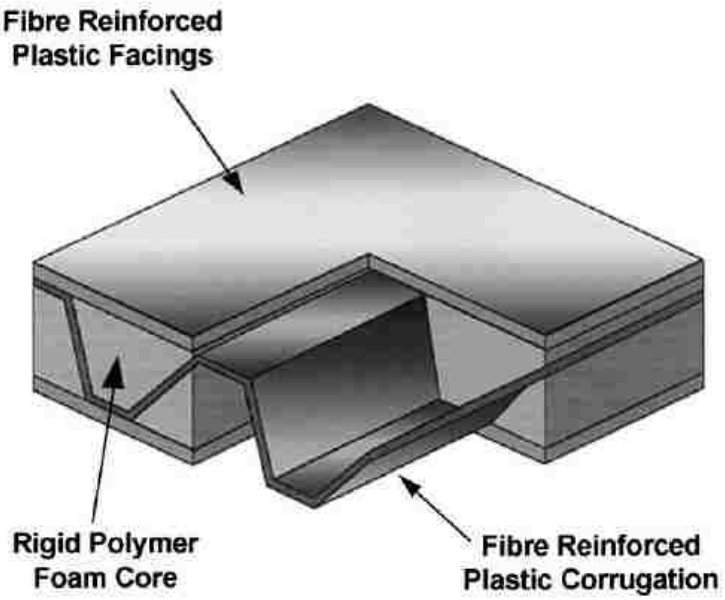

Figure 1-2 - Corrugate Foam Core [9]

A more common way to provide the desired reinforcement is to use woven fabrics [13–17] in conjunction with the polymeric materials in order to create a stronger and stiffer material than the polymer alone. Often times these fabrics are found in pre-preg, or pre-impregnated, form instead of mixing the two materials together *in situ*. Woven reinforcements can allow the composite laminas to behave in a more isotropic manner than the unidirectional laminas that are often created. The directional behavior can also be influenced by the layup employed in the creation of the composite panel. Layup designation is one of the more important aspects needed in describing the experimental setup use when testing a composite. The first example seen of this is seen in the abstract for [5]. Stacking sequences denote the orientation primarily, but in the case of irregular composite layups (where the thickness of each lamina is not the same) the notations can be changed in order to account for this. Since this type of composite will not be discussed much further, a brief example will be provided for edification purposes only. An example symmetric layup notation would be $[\pm 45°/0°/90°]_{sym}$ where each lamina's principle direction would be designated by the order written. Since the directional behavior of the composite can be either beneficial or not, the application drives the design and direction of the fibers to the greatest degree. Returning to the woven fabrics, the reinforcing fibers can range greatly in material type and performance. One of the more common fibers used is E-glass [14–17] due to the relative low cost of the material compared to other fibers. E-glass is created by drawing silicon dioxide into

fibers and is readily available for the use in composite manufacturing. Other fiber types include high strength aramid fibers [18–21], such as DuPont's Kevlar, hemp fiber [22], and carbon fiber [5,6,8].

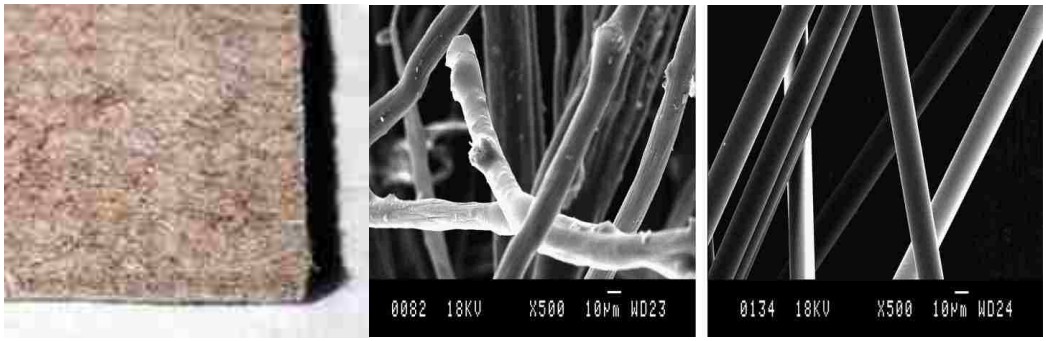

Figure 1-3 - (Left) Non-woven Hemp Mat, SEM Image of (Middle) Hemp Fiber, (Right) Glass Fiber [22]

Another way in which fabrics are used as composite reinforcement is in non-woven mats [22]. These mats contain fibers in a bulk configuration with little or no mechanisms holding the fibers together. Once these mats are infused with the polymer the matrix becomes the only binding agent. Non-woven mats will not exhibit failure in the same manner that a woven or otherwise reinforced composite would due to the lack of continuous fibers imbedded in the polymer matrix. A final design type employs more advanced textile manufacturing in order to create knitted patterns [2,4,23–29].

1.3 Knitted Composites

Knitted reinforcement designs take individual yarns and tie them together through a series of loops, resulting in a more flexible reinforcement that can be used when a compliant design is desired. As several studies cite, the opportunity for the use of knitted reinforcements is a great one that should be better explored [2,4,23,24,26]. With advances in the textile industry, the ability to create near-net-shape fabrics has emerged [4] with nearly limitless possibilities of creating simple structures such as helmets to more complex products such as pipes with integrated flanges and connectors.

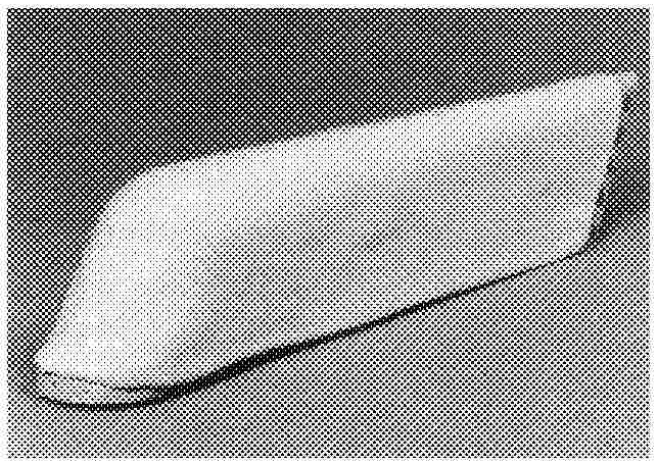

Figure 1-4 - Net-shape glass knitted preform for a rudder tip fairing of a passenger aircraft [4]

This is a vital advancement when concerned with the formability of the materials as well as what the knitted structure will look like once the material has been formed. It also helps minimize the amount of waste and production time, but can

still be quite time consuming due to the complexity in creating the knit designs. Another benefit pointed out by Leong, *et al.* is the cost portion of production. By combining inexpensive textile manufacturing techniques and products with polymers matrices, low cost, highly deformable composites can be made. A variety of applications can employ a knitted reinforcement structure. As mentioned previously, the medical field [2,4] is one such area where flexible composite materials are desirable. While [2] looks at the direct application of these composites, [4,23,25] all highlight the benefits of using knitted fabric in thermoforming applications. By creating large loops in areas that experience large deformation (forming corners, etc) the reinforcement tension can be tailored in such a way to retain a more uniform distribution.

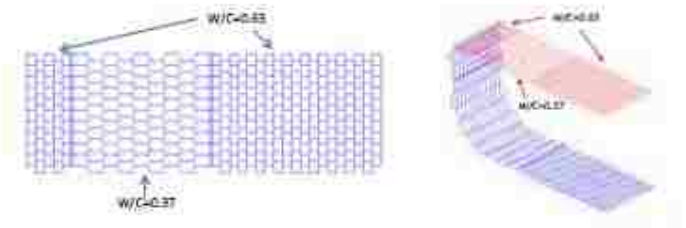

Figure 1-5 - Patterned Knit (left) and Deformed Configuration (right) [23]

In addition to the medical field, knitted composites can be used in industrial applications such as the commercial roofing application that will be discussed in greater detail later in this study. The relatively low cost of production is always a desirable characteristic in the business world, so the advancement of knitted composites for increased performance is of great interest.

1.3.1 Knitting Terminology

In order to examine knitting in further detail, the basics of the processes need to be discussed first. The first bit of important terminology is the names for the rows and columns of the fabric, which are referred to as courses and wales, respectively. These courses and wales are interlocked in order to form the final fabric product. The inverse values of wale count, *W*, and course count, *C*, can be used in order to define the geometric parameters of the repeating unit cells as seen in [23]. An in depth look at the scale values used to analyze knitted fabrics will be discussed below. Another important term used in fabrics is the density of the fibers, usually reported in either denier or Tex. These values are important to note since they can be used in order determine the total number of filaments that are used to construct each yarn or fiber.

Next, the actual techniques that are employed, in the most basic sense, can be categorized into weft- and warp-knitting. Weft-knitting is performed with one yarn moving perpendicular to the direction in which the fabric is produced, while warp-knitting is completed with multiple yarns being fed in parallel with the direction in which the fabric is being made [4]. With this knowledge, the number of loops in the wale direction will be created using a single needle whose gauge, along with yarn type, size and applied tension, are all vital in determining the density in which the loops are created using weft knitting. Conversely, the number of loops in the wale direction using warp knitting is dependent on the number of “warping beams” that

feed yarns into the knitting pattern, thereby allowing the interconnection of columns in order to create a completed product.

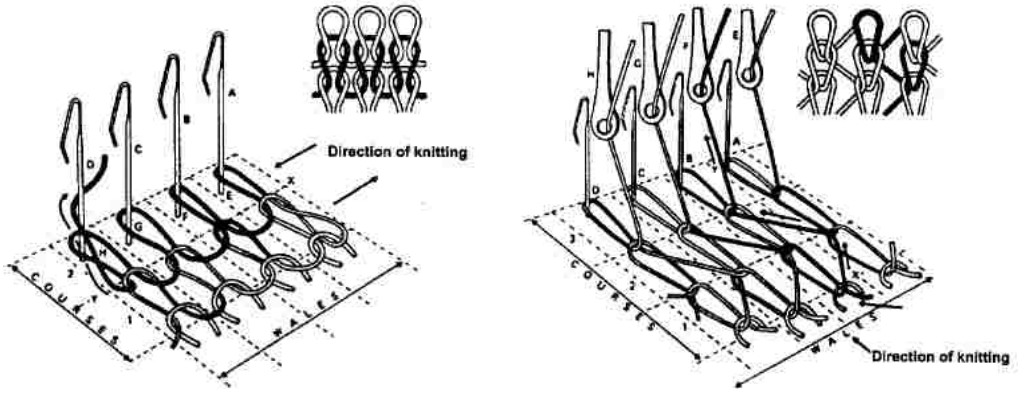

Figure 1-6 - Weft Knitting (left) and Warp Knitting (right) [4]

The main difference between the two styles is the stability of finished product. In general, weft-knit structures are less stable, thereby allowing them to stretch and distort more easily than warp-knit counterparts. This leads to increased formability in the composite creation process. Obviously depending on the desired behavior in the specific application, this could be viewed as a positive or negative. On the other hand, examining the production capabilities of both methods, warp-knitting is more desirable for large scale production based on the volume flow rate allowable due to multiple yarns being fed at once. For development purposes, where small amounts of fabric, as well as the ease of customization, are desirable, weft-knitting would be the process of choice. In combination with the warp- and weft-knitting techniques, the type of stitching will also affect the overall fabric behavior. Tuck and float

stitches are the two main types of looping that allow for the macroscopic changes to the properties of the fabric. Tuck stitches result in the wider, thicker, and slightly less extensible fabric [4] while the float stitch will result in the opposite description with an increased number of straight yarns in the overall structure. The literature also goes on to describe the vast amount of different high-speed machines that are available in order to perform the desired knitting actions.

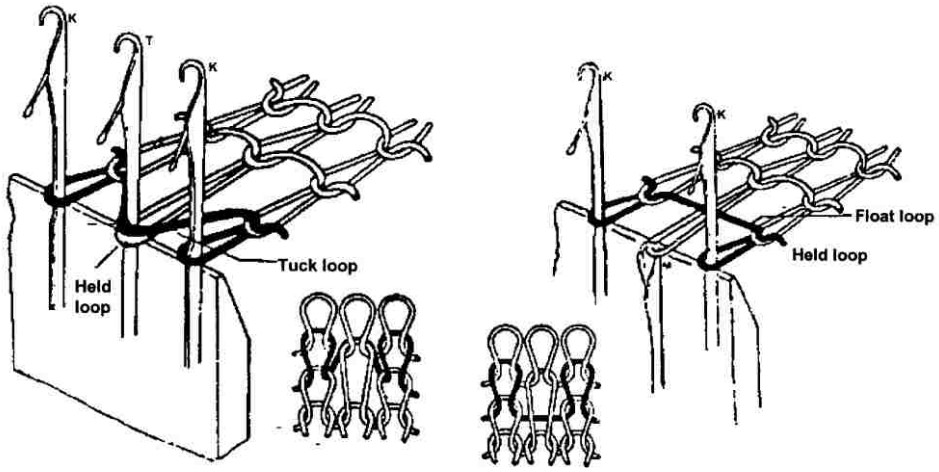

Figure 1-7 - Tuck (left) and Float (right) Stitching [4]

1.3.2 Processing Issues

One of the concerns with knitting materials is the degradation of performance that could occur during the processing techniques discussed above. This is a concern since the raw material properties are known, but the final properties could be changed due to the manufacturing method. Lau and Dias [30] examined this issue and found that the loop strength of glass yarns increased almost exponentially with knitting needle diameter. This phenomenon is due to the mechanical properties of

the materials often chosen for reinforcing in composites and the fact that bending these yarns around tight radii can cause significant damage to the internal fibers. This issue can hinder the available complexity of the possible structures. In order to avoid this situation, the first solution is the employment of spun yarns that consist of much shorter fibers that are twisted together. These yarns improve the knittability of the material while still preserving some of the properties of their continual filament counterparts [4]. Another benefit to the spun yarns is their improved wetting properties over yarns with continuous filaments [31]. This refers to the impregnation capabilities of the fibers with the resin system used in the composite structure. Another possible solution to allow for complex structures to be created is to make adjustments to the conventional machinery as suggested by [32] with the use of ceramic guides and extension springs.

Another cause of failure in the manufacturing process is due to the build-up of tension in the yarns. This accumulation of tension is due to the superior tensile properties and low-rupture strains inherit in the advanced fibers that are desirable for use in composite manufacturing. Of course more flexible yarns would counteract this tension induced failure in the manufacturing process, but they would not be nearly as beneficial in the final product's behavior. Since most textile manufacturers are concerned with general knitwear, the high-modulus yarn desirable for composites are very different and therefore can cause great difficulty in production. Lau & Dias [30] go on to examine aramid fibers and compare them to E-glass based

fibers as well as standard cotton and acrylic fibers that would be used in general knitwear creation. Since the initial tensile strength of high-modulus yarns could easily withstand the tension created by the knitting process, it was very interesting to find the fairly low breaking points exhibited by such fabrics at the Kevlar fibers tested. This behavior could be attributed to the bending of the filaments, thereby preventing them from lying straight, causing an uneven distribution of the loading. Additionally, loop efficiency, which was defined as the loop strength (found experimentally through uniaxial tensile loading with needles acting as the grip) divided by the tensile strength of the material. The results of this experiment found that the continuous glass fibers were greatly influenced by the needle diameter, which is to be expected due to the brittle nature of the filaments as well as the aforementioned degradation issues related to needle diameter.

Lau & Dias cite that friction and the angles of contact will increase the input tension of the yarn during the knitting process by the following manner through Euler's capstan equation:

$$\boldsymbol{T = T_i e^{\mu\vartheta}}$$

E. 1.1

Where T is the calculated tension in the yarn, T_i is the input tension, μ is the coefficient of friction between the yarn and the knitting elements, and θ is the sum of the angles between the yarn, needles and other knitting elements in contact with

the yarn. The frictional properties, along with the pliability and strength of a yarn are vital in determining the efficiency in which a fabric can be made.

In [30] it is noted that the optimum coefficient of friction of spun yarns is 0.13. Tests revealed that pre-lubricated cotton yarn had an average μ value of 0.12, while Kevlar had a very high value near 0.47 before lubrication. Textural 7970 sewing lubricant was applied, which dropped the coefficient of friction down to near 0.37 for the Kevlar. This value, however, was still a substantial amount higher than even un-lubricated glass fibers with μ value of 0.29, and even higher still than the lubricated results of a μ value of 0.18. But again, this value merely affects the calculated tension on the fiber, where in relative terms the E-glass fibers will still perform lower than the Kevlar due to the great amount of breakage that occurs. Another contributing factor to the effect friction has on the degradation of the material properties returns to the mention of the denier number mentioned earlier (number of filaments can be found using fiber diameter, density and denier value). With multiple filaments existing together inside a single fiber, if left unprocessed, the filaments could spread out, thereby increasing the surface area in contact with the needles and other knitting elements. Increased surface area would lead to a higher frictional force. A simple solution of twisting the fiber in order to keep the filaments closer together is suggested. Additional suggestions for minimizing the frictional impact is to, whenever possible, use hard ceramics for surfaces that the

yarn will contact. Along the same line, is to simply minimize the number of separate guide surfaces and changes in direction.

A final failure method occurs through abrasion which was quantified by Anderson *et al.* [33,34] by measuring the amount of dust that was emitted during the knitting process. Measurements were obtained by using two pins, 3mm (0.118in) in diameter, in a dust sampling chamber. Two different materials, polished high carbon steel and ceramic, were used for the pins in order to examine the effect the change of contacting surface had. The team concluded that the emission of dust was due to the overall brittleness of the fiber, as well as the efficiency of the surface coatings. These coatings again included a textile lubricant. Another interesting finding made by the team was that the polished steel pins resulted in higher frictional force build-up than more abrasive (caused by scratched) pins. This was attributed to the uninterrupted contact between the yarn and polished surfaces. A similar test was performed by Andersson *et al.* [34] where cyclic loading of yarn was performed where the abrasive nature of the pins also included intentional corrosion of the pins in order to examine damage caused.

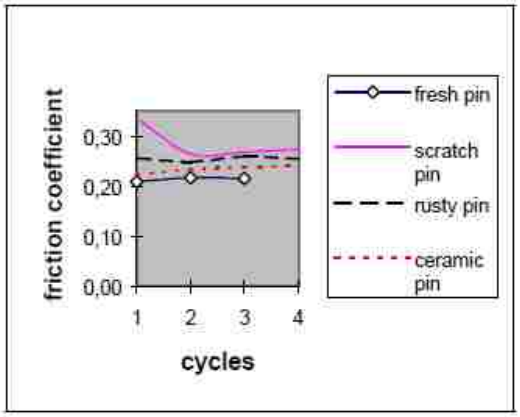

Figure 1-8 - Coefficient of Friction Comparison for Different Pins [34]

1.3.3 Unique Characteristics

One additional item that [4] discussed involved the insertion of a straight fiber through the loops of a knitted fabric. As seen in Figure 1-9, yarns are introduced through the loops of the knit that allows for the tensile strength and stiffness as well as the energy absorption capabilities of the material to be considerably higher than standard knitted composites. On the other hand, the introduction of these additional fibers causes the formability of the material to decrease as compared to more flexible patterns. This "hybrid" method of combining both knitting and weaving does allow for a marriage of the most beneficial aspects of each method. Additionally, by adding the straight inserts into the knit pattern, desired anisotropic tailoring can be achieved.

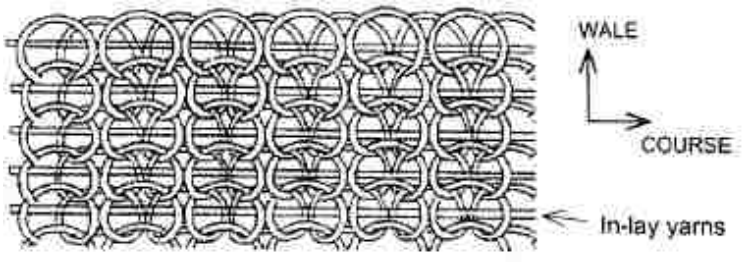

Figure 1-9 - Schematic of weft-insert, weft knit fabric [4]

In this same mindset, split-warpknits are essentially the same concept as the weft-insert fabrics, but instead of simply inserting un-crimped (straight) yarns, films of polymer such as polypropylene (PP) are inserted into the knit pattern. This allows for properties equivalent to those of commingled woven composites, but at a much lower production cost.

Ramakrishna *et al.* [2] examined a unique characteristic of employing knitted reinforcements in that they can be pre-stretched. This method is similar to the pre-tensioned reinforcing bars used in concrete. The team discovered that by pre-stretching the fabric before it is introduced into the matrix, the mechanical properties of the flexible composite could be tailored to a certain extent. The team found that both the stiffness and strength increased in the direction of the fabric pre-stretch and deteriorated in the direction normal, while the failure strain behaved in an inverse manner. In order to achieve the pre-stretching, the team designed and built a jig that allowed the percentage of stretch to vary independently in the course and wale directions.

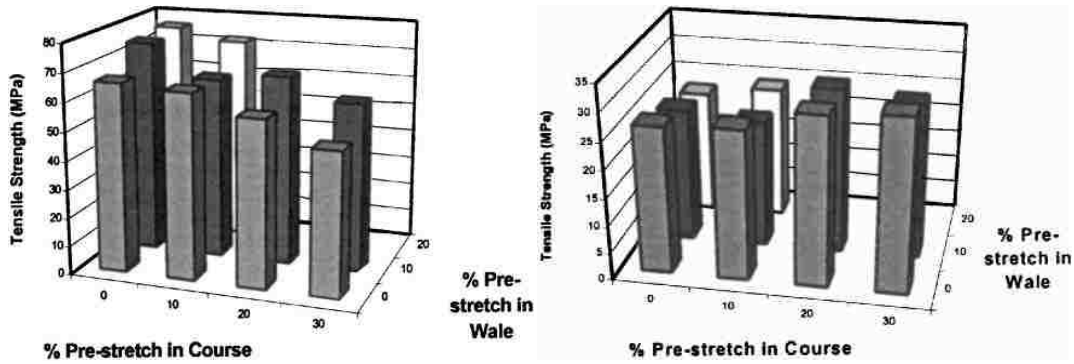

Figure 1-10 - Graphs of Tensile strength vs. (%) stretch of wale-(left) course(right) - tested specimens [2]

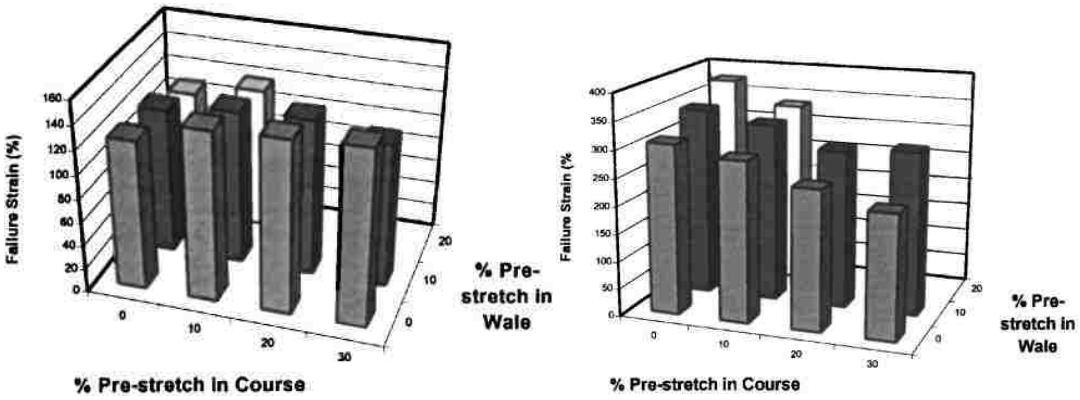

Figure 1-11 - Graphs of Failure Strain vs. (%) stretch of wale- (left) course (right)- tested specimens [2]

In Figure 1-10 and Figure 1-11, the wale- and course-tested notations refer to the direction in which specimens were cut from the manufactured sheets. The discrepancies in the tensile strengths of the specimens occurred from the start when it was found that the fabric had inherent anisotropy with superior stiffness and strength in the wale direction. This was attributed to the greater number of fibers oriented in the wale direction than the course direction. The team analyzed pre-stretch percentages up to 30% which, as seen in Figure 1-11, resulted in dramatic

decreases in the failure strain. As noted by the study, when combined with a polyurethane matrix, with a very high ultimate strain of 1078%, the knitted reinforced composites yielded ultimate strains in the range of 108-320%, depending on the specimen type. This is a significant improvement over failure strains of other composite which see failure strains in the 2-8% range.

1.3.4 Modeling of Knitted Fabric Reinforced Composites

As with any other engineering problem, it is often beneficial to be able to model the scenario in order to better examine all of the nuances. In this light, knitted fabric reinforced composite materials are no different. Woven and sandwich composite panels have been modeled in a variety of studies [9,11,15,35–37] where the increased geometric complexity of knitted fabric reinforced composites creates difficulties when modeling is concerned. As pointed out in [29], a full scale fiber based model would consume a vast amount of computational resources in order to accurately model. At the micro-scale, models from Miao, *et al.* can begin with individual fibers, which are combined into yarns in a digital model in order to examine fiber-to-fiber and yarn-to-yarn interactions. Besides the computational intensity involved in the modeling, physical properties are also difficult to obtain since many fibers are not tested in the manner needed to extract the desired behaviors. This is true when studying the compressive stiffness of a fiber, which would be dependent on the transverse modulus, which is rarely available due to most inquiries being concerned with axial modulus. The next difficulty that arises is

the non-linearity of the subject matter due to the large deformations that are seen in textile processes as well as the general loading of a knitted structure.

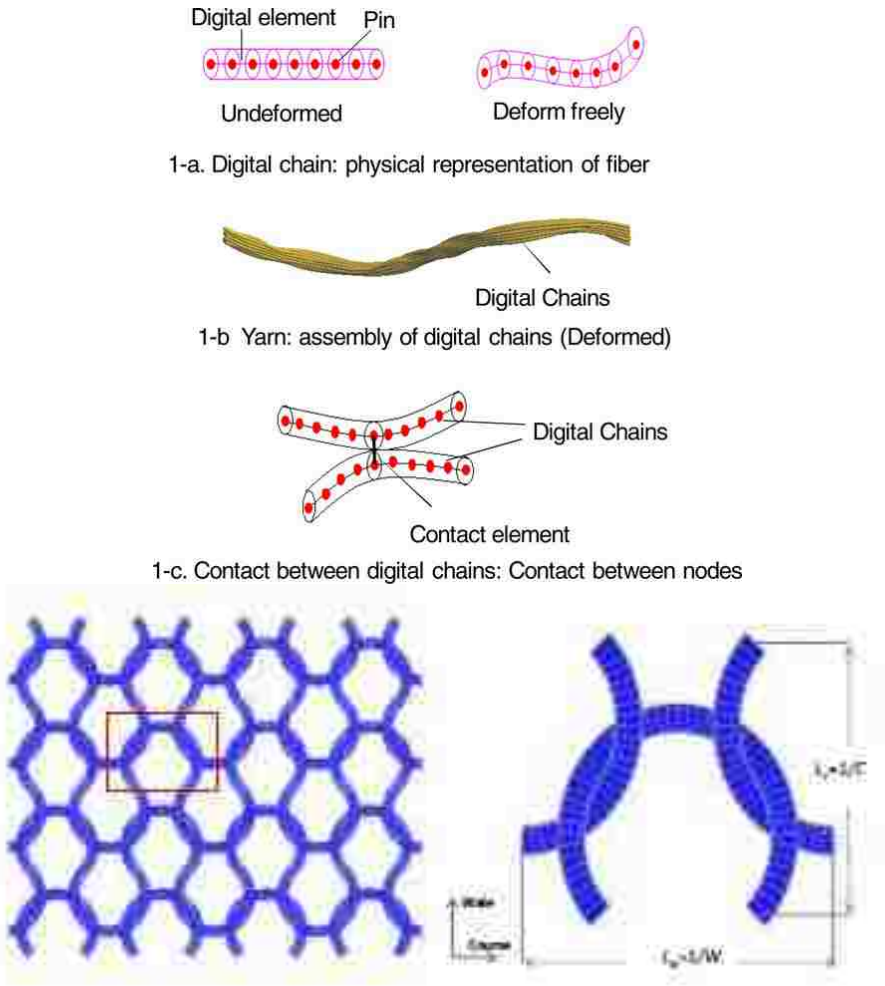

Figure 1-12 - Digital Representation of Fiber Interaction (Top) [29] Unit Cell Schematic (Bottom) [23]

In order to modify the original model so that the desired improvements can be made, simplifications such as node-element contact analysis instead of node-node contact analysis are employed. This allows for the use of much coarser mesh, thereby greatly reducing the total number of calculations that are needed. Another

study that began with a micro-scale model was performed by Bekisli [23] which began with a unit cell analysis due to the repeating nature of the knitted structure as seen in Figure 1-12. Initial models consisted of a 3D unit cell with great detail put into the actual diameter of the yarn using solid elements in ANSYS as filler with a beam element with linear elastic material properties through the interior of the filled zone. Filler elements were an important aspect of the micro/meso scale model due to the contact behavior between elements that occurs as yarns touch and deform around each other. Because of computational intensity and complexity, friction between the yarns was not generally taken into account, which resulted in over-prediction of the critical stretch values. Critical stretch is defined as the point at which the segments of a loop are as straight as possible and the stiffness of the fabric increases dramatically. Once the unit cell analysis and results were considered satisfactory, the mechanical properties were imported into a macro scale model that consists of a multitude of repeating loop structures. Since the rounded nature of knitted yarns is a fairly complex design to implement into a finite element program, a hexagonal honeycomb structure was employed due to its resemblance to the actual pattern.

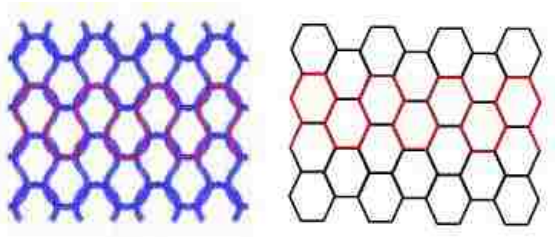

Figure 1-13 - Comparison of Knitted Structure to Hexagonal Honeycomb [23]

Other studies take a numerical modeling approach such as [27] where the elastic properties of a knitted fabric composite were studied in extensive detail using a combination of different previously established methodologies that are typically used for more conventionally reinforced composites. Three models (1D Krenchel model, 2D laminate approach, and 3D aggregate subcells) were each examined and adjusted accordingly in order be more applicable to the knitted fabric composites. Huang, *et al.* [28] also took a similar numerical modeling approach by breaking the knitted composites down into the subcells called representative volume elements (RVE). Each RVE was assumed to have the same fiber volume fraction as the full scale composite. Due to the large deformations observed in the knitted structures, the team's numerical model was only able to provide satisfactory predictions up to 50% of the ultimate strain of the composite.

2 Impact Performance Characterization

2.1 Testing Methods

In order to characterize the performance of a composite, a variety of tests need to be performed depending on the loading methods that will need to be withstood. One of the more vital testing procedures deals with recreating or at least mimicking impact events, which can be divided at the simplest level into low- and high-velocity impact conditions [38]. In [38], Cantwell and Morton defined the limit for considering an impact event "low-velocity" as below 10m/s. This gives a large range of velocity values for high-velocity, or ballistic, testing to take place. These impact events differ from their lower velocity counterparts as the strain rates in which they occur do not allow the stresses to be distributed to the outreaching fibers, but instead concentrate all deformation near the point of impact. Obviously, it is important to create a test where the loading scheme occurring will most likely reproduce a similar failure mode and mechanism to that in the real world application. As pointed out by [38] and [16], this is at times difficult to achieve since many previously established techniques have really been developed for testing metal structures, so their applicability to composite characterization is found to be inconsistent in many instances. Two such procedures for low-velocity testing are the pendulum based Charpy and Izod impact tests. The team found these testing methods to be suitable for impact performance ranking of continuous fiber

composites, but the repeatability was insufficient to depend solely on these experimental test setups.

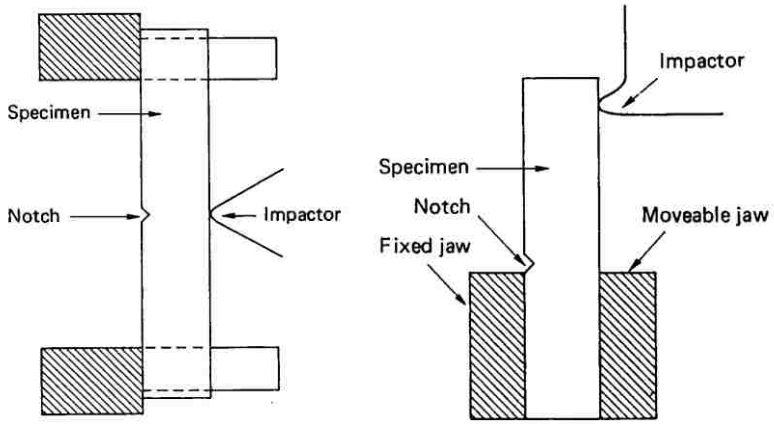

Figure 2-1 - Charpy Impact (Left) and Izod Impact (Right) [38]

Another pendulum based test was discussed by [36] where the differences between tensile- and flexural-impacts were examined. In this study, a CEAST Pendulum (named after Compagnia Europea Apparecchi Scientifici, Torino that invented the testing technique and seen in Figure 2-2), was used in order to strike the grip points of a specimen held in tension. This type of loading is much simpler than the flexural-impact counterparts due to the avoidance of such complex loadings at plate bending (one portion of the specimen in tension, the other in compression) and varying strain-rate loadings (transition through the layers of a composite).

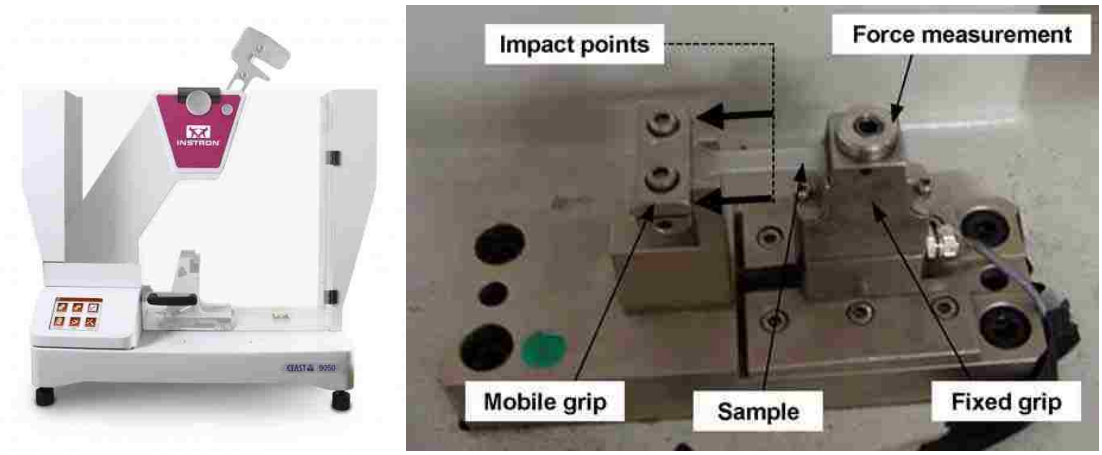

Figure 2-2 - Instron CEAST 9050 Impact Pendulum (Left) Loading and Grip Conditions (Right) [36]

Another advantage that the team points out is that the impactor in this case does not come into direct contact with the specimen, which allows for a more homogenous distribution of stress, strain and strain-rate as compared with impact events that induce local indentation. A similar loading occurs in the Hopkinson-bar technique discussed by [38] which can be considered more of an intermediate, or high velocity loading due to the flexibility in the testing conditions that can produce much higher strain rates than available in the low-velocity tests. The Hopkinson-bar technique places a test specimen bonded between an incident bar and transmission bar. Strain rates approaching $1000s^{-1}$ can be achieved by accelerating a striker, often times a using gas-driven projectiles, in order to impact the incident bar causing an elastic wave pulse.

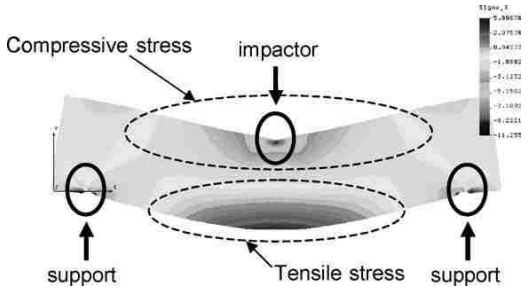

Figure 2-3 - FEA Simulation of Stress Distribution During Impact Event [36]

Another more common low-velocity impact test is the drop-weight impact test using an instrumented drop tower that is designed and manufactured for such a purpose such as an Instron Dynatup model or other equivalent models [10,13–15,22,38–41]. In these tests a weight is dropped from a pre-determined height, according the desired energy level of the impact, in order to strike a test specimen supported in the horizontal plane. As pointed out in [38] the impact usually does not result in complete destruction of the specimen, but rather rebounds, allowing for the calculation of the amount of energy returned to the system, if desired. The remaining energy is absorbed by the specimen through various failure modes. Within fiber-reinforced polymer composites, the most common failure mechanisms include delamination, intralaminar matrix cracking, debonding between fiber and matrix, fiber pull-out, and fiber fracture. This type of testing is particularly effective in testing knitted reinforcement polymer composites at low velocities as reinforcement layer can behave similar to a net, thereby allowing the impact load to be redistributed through the fibers to the boundaries. This behavior would not be

observed in more localized small scale tests like the Charpy as discussed above. The effects that physical properties of each of the constituents have on the overall impact performance will be discussed in more detail in a subsequent section.

For panels used in the civil transportation industry, the impact performance is of great importance due to the safety of passengers in a collision event. There are many studies available that examine this aspect of composite panel design [7,9,10,13–17,22,35,36,39,40,42] in a variety of different ways.

Figure 2-4 - Instron CEAST 9340 Drop Tower

As mentioned above, testing apparatuses such as the Instron Dynatup series are enclosed towers that are already outfitted with all the different sensors that one might need, including force transducers, velocity verification tools, and accelerometers, as well as rebound prevention add-ons that allow for a clear depiction of the impact event without a subsequent impacts clouding the post-mortem evaluations. All of the sensors and add-ons are fed into a central data

acquisition system that collects and displays all the data that the tests require. These are very user-friendly experiments with little worry regarding calibration, etc.

The downsides of these fully instrumented units are their large capital costs and the inability to easily customize the experiments. In order to save on costs and customize tests to provide specialized data, some research groups have designed their own “home-grown” impact towers and outfitted them with the desired sensors [9,16,17,35]. One of the more important aspects of the fabricated drop towers is the design of the guide system that directs the impactor towards the specimen to be tested. The first is a guide-rail system [16,17,35] with a crosshead that can allow for the addition of extra weight in order to change the amount of energy used for impact. These systems more closely mimic the enclosed Dynatup series models. A second guide system used for these drop towers is seen in [9] where a vertical tube directs a falling “dart” towards the test panel directly below the end of the tube. The falling weight is often instrumented with at least an accelerometer in order to extract the data from the impact event. This study also provided one of the more interesting examinations of impact tests, where the team was interested in quantifying the amount of energy that is transferred to the panel’s supports, not just the total amount of energy absorbed by the system. As more impacts occurred, the composite panels became more compliant, thereby allowing more of the energy to be transferred directly to the support structures. Another important aspect in the design of an impact testing rig is the shape and size of the impactor, often called the

"tup." Since, as mentioned earlier in the comparison between low- and high-velocity impacts, the behavior of materials is often strain-rate dependent, the geometry of the impactor is vital in the distribution of strain over the test specimen. This also ties into the determination of the sample size used. As with any other loading type, stress concentrations, which are heavily influenced by changes in geometry, can have a drastic influence on the final performance of the loaded object. A final factor to take into account during the design of an impact test machine is the clamping conditions used to hold the specimen in place. Many pre-fabricated testing machines used circular portals to clamp the specimens due to the aforementioned influence of the geometry on the stress concentrations. The circular shape allows for even distribution in smaller specimens, thereby reducing the amount of material used. As mentioned above in the discussion of Torre & Kenny's work, sometimes it is of interest to determine the amount of force transmitted to the support structures, in which case load cells can be employed in order to record the loading felt by the fixtures.

Another testing method is shock loading [14]. This type of impact loading is primarily used to mimic stress wave loading often due to explosions, especially in marine applications. In this testing scenario, a driver is used to create a short duration shock wave with a planar wave front in order to apply varying pressures to the test specimen. In [14], Herber, *et al* examined peak incident pressure loads

ranging from 3.08-7.53MPa which was achieved using pressurized Helium that was released due to the rupture of a Mylar diaphragm.

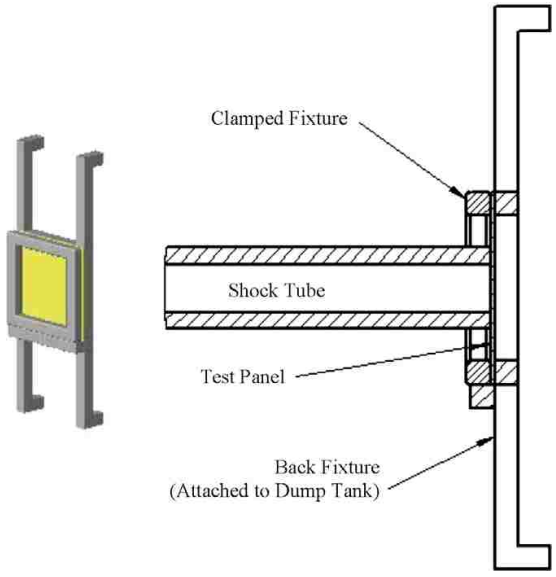

Figure 2-5 - Shock Loading Setup Schematic [14]

The previous examples have been considered low- or intermediate-velocity impact tests. These testing methods are fine for use when concerned with the civil transportation field as well as most portions of the medical field and structural composite applications, but another testing method that is also available is an important part of composite designs. Ballistic testing [18–21] examines the behavior of a material when it is impacted by a projectile at a much higher velocity than the tests mentioned thus far.

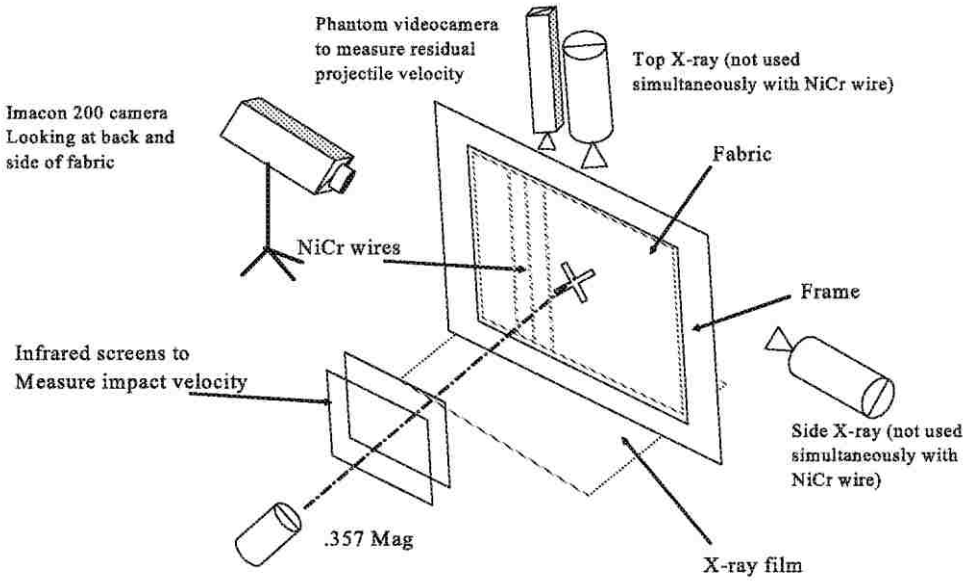

Figure 2-6 - Example of a Ballistic Testing Setup [18]

Often times these types of tests involve optical sensors to measure the projectiles velocity, as seen in Figure 2-6. Most full composite tests performed under ballistic conditions are intended for personal protection applications so velocity ranges are expected to correspond to typical small arm velocities between 300-500m/s [18,21]. Additional examinations [20] look at the performance of the fibers alone in lower ranges near 30-60m/s that are still considered to be in the high-velocity realm as discussed earlier. Most of these experiments will look at the probabilistic velocity response (PVR) of a material in order to quantify the probability that the projectile at a given speed will result in full penetration of the test specimen. An example of a PVR curve can be found in Figure 2-7

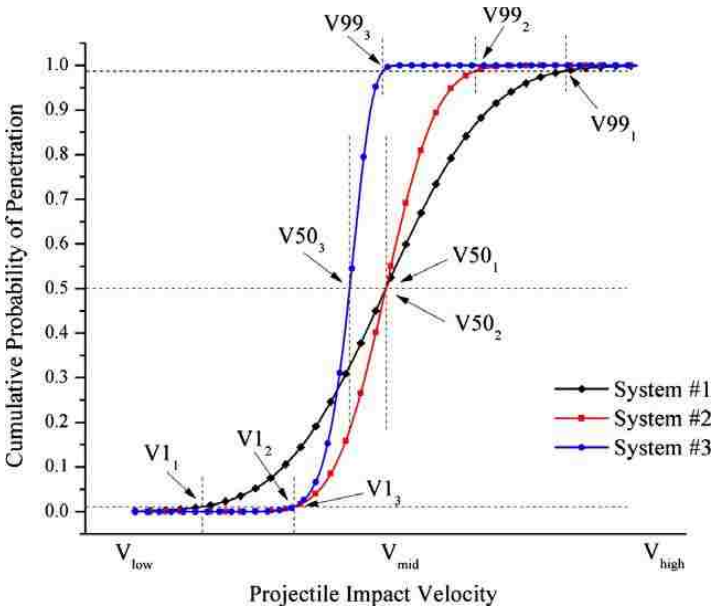

Figure 2-7 - Example of PVR Curve [20]

Cantwell and Morton [38] go on to point out that during a ballistic impact event the structure will respond in a local failure mode in such a way that the strain energy absorbing capabilities are less important than in a low-velocity impact event. Impact tests are vital in accurately qualifying a material for performance as standard static tests will not be able to identify the strain rate sensitivity that some materials display.

2.2 Evaluations

After the impact tests have been performed, the post-mortem evaluations are the next concern. The evaluation techniques used will again depend on the application. In some instances, the material properties will be tested to allow for degradation analysis. There are a variety of ways to evaluate the performance of a

material following the impact testing procedures outlined above. Some of these evaluation methods are fairly invasive or destructive, while others are merely comparing collected data to previously established predictions, such as those obtained by the modeling techniques outlined previously. These evaluations are of great importance since, as found in the literature, damage and failures are difficult to identify, thereby possibly allowing composite structures to remain in service following impact events.

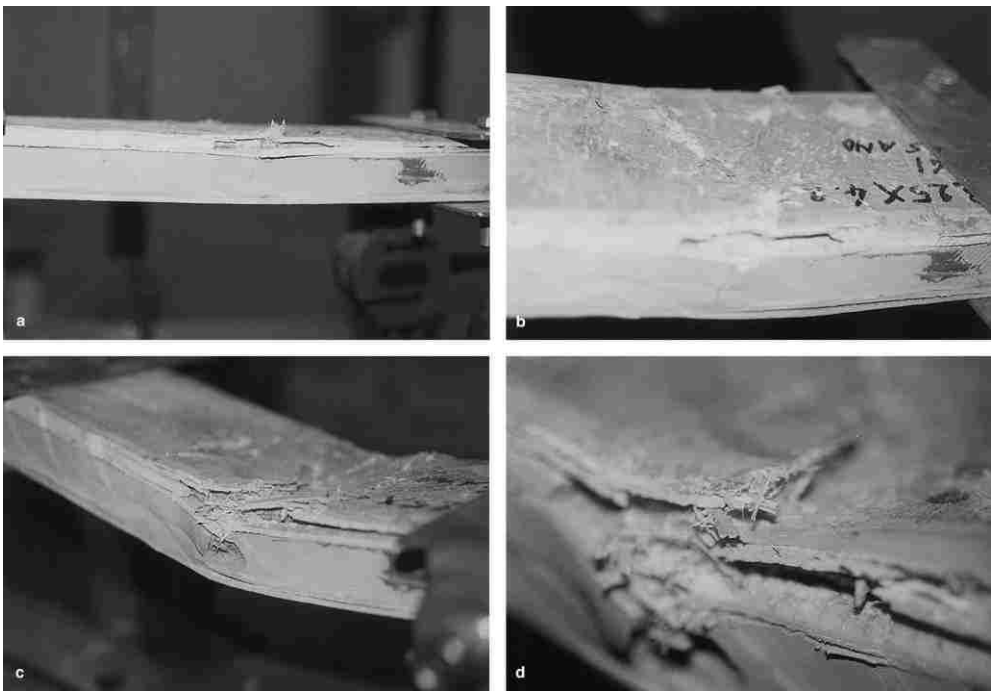

Figure 2-8 - Images of Composite Sandwich Panels After Impact [9]

2.2.1 Physical Testing

One way in which this is accomplished is through compression after impact (CAI) tests [10,13,14,43]. In this method the impacted specimens are subjected to

compressive tests that comply with the appropriate set of industry standards. The reasoning behind this testing is, as pointed out by [13], that the impact events can cause delamination in the composite, which will significantly reduce its residual compressive strength as well as its strain-to-failure.

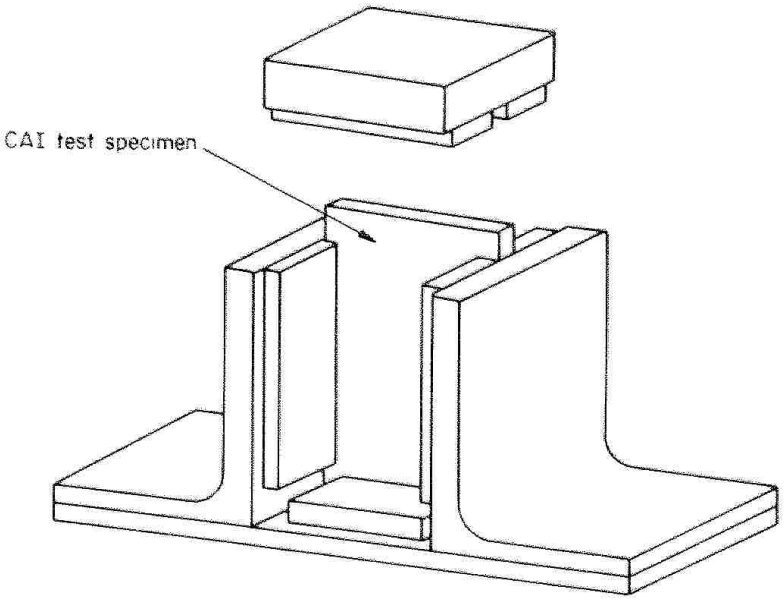

Figure 2-9 - CAI Test Fixture with Specimen [13]

An interesting aspect of this study, as compared to Hebert, *et al.*, is the use of an anti-buckling fixture for the compression test, as outlined by a Boeing created methodology. This test setup can be seen in Figure 2-9 where compressive strength can be isolated from critical buckling strength be the implementation of simple lateral supports. Adjustments to standard compression tests were also made by Schubel, *et al.* [10] citing stability issues caused by stress concentrations and the end effects of the column type structures being end-loaded. A similar testing method

would be to test the remaining tensile strength of the panels [41,44,45]. Two studies involving Tai [41,45] took the tensile examination a bit further by applying fatigue analysis to the post-impact tensile tests. The fatigue tests were performed using either tension-compression (T-C) tests or tension-tensions (T-T) test where both were found to exhibit similar S-N curve trends. S-N curves represent the fatigue properties of a material by plotting the stress (S) versus the number of cycles to failure (N), usually shown on a logarithmic scale [1].

A third physical method is the use of four-point bending (4PB) tests [9,15] which would measure the amount of flexural strength that is retained in the test panel. Reyes & Sharma employed this testing method in lieu of more conventional testing by means of CAI due to the complex rig and friction effects between the laminate and guides, which are difficult to take into account. The simplified testing would be used to provide a sufficient examination of the post-impact mechanical properties. A final method of physical evaluation would be to actually perform additional impact events to see how the material behaves [9]. This evaluation method would be especially important in quantifying the life-span of a certain composite panel which would be a vital factor in cost related decisions.

Another important item that this study provided was non-dimensional parameters in order to quantify the impact performance of the composite panels. Beginning with the strain ratio defined as:

$$\boldsymbol{RD = \frac{Def_{max}}{a}} \qquad \textbf{E. 2.1}$$

Where the maximum deformation (Def_{max}) is caused by the dart displacement, and a is the span of the plate. Moving forward, the Absorbing Energy and Moment Parameter is defined as the ratio between the energy loss and maximum moment due to the impact force as seen in:

$$\boldsymbol{AEMP = \frac{E_{max}}{M_{max}}} \qquad \textbf{E. 2.2}$$

Where:

$$\boldsymbol{M_{max} = \frac{P_{max}}{2}\frac{a}{2}} \qquad \textbf{E. 2.3}$$

Where P_{max} is the maximum load due to the impactor. Finally, the Performance Parameter is defined as:

$$\boldsymbol{PI = \frac{AEMP}{RD^2}} \qquad \textbf{E. 2.4}$$

While the *AEMP* parameter is used to measure the capability of a structure to absorb energy, the *PI* value gives a more complete examination of the crash performance. A high *PI* value will indicate that a panel is capable of absorbing a large

amount of energy, without transferring excessive deformations to the inner structures, which is vital for a crash resistant component in the realm of transportation related designs. As stated above, the Torre and Kenny [9] examined the effect multiple impacts have on the performance of the composite panel. By plotting the Performance Parameter as well as the flexural stiffness vs. the number of impacts, a similar trend is seen, while the Absorbing Energy and Moment Parameter displays an opposite trend. This is due to the support structures absorbing much of the energy and allowing for much larger deformations, leading to the aforementioned trend in the Performance Parameter, showing the best indication of the crash performance.

2.2.2 Non-Invasive Examination

Another method of evaluation is by close examination of the test specimens. The first, and simplest, example of this is visual inspection [14,40] which includes measuring the permanent deformation of the panels as well as the size and shape of the indentations. Along with these measurements, it is important to take note of any clear signs of matrix cracking, delamination or clearly visible fiber breakage. Since the first two items are often times very difficult to distinguish by the human eye, more advanced examination techniques can be applied.

Scanning Electron Microscopy (SEM) [15,22] and ultrasonic C-scans [10,13,16,39,41] allow the observer to capture these minute defects. SEM works by

scanning the surface of a material with an electron beam and the back-scattered electrons are then collected and displayed [1]. These images give a good representation of the surface of the interested material and can produce incredibly high-resolution images with significant amounts of magnification. Reyes & Sharma [15] used the SEM images in order to examine the relationship between increased incident energy and the amount dissipated throughout the composite by way of permanent deformation and failure, more specifically by way of fiber breakage and delamination. Ultrasonic C-Scans employ a transducer to scan perpendicular to the surface of the specimen, measuring the reflection of sound waves. A schematic of this scenario can be seen in Figure 2-10. B-Scans use the same methodology along the profile, or cross-section of the specimen as the plane of interest, while A-Scans measure the amount of ultrasonic energy reflected as a function of time, rather than distance [46]. C-Scans are very useful tools in that they can produce very detailed images.

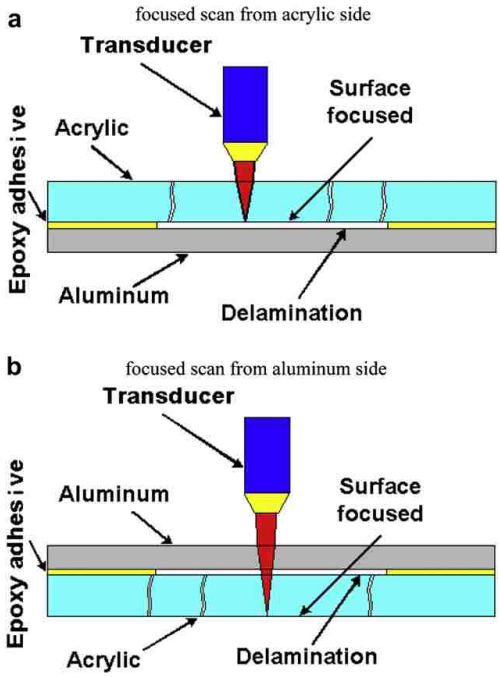

Figure 2-10 - Schematic of Ultrasonic C-Scan [39]

One small problem with the C-scan technique as cited by [39] is that air gaps, as seen in Figure 2-11, caused by delamination failure in bi-material composites can cause feedback errors that will block the C-scan from seeing through the gap. C-Scan limitations were also discussed by [13] where the images showed the sections that maximum delamination occurred within the panel, but does not necessarily encompass the true picture of the damage zone. Schubel, *et al.* [10] used the C-scan results in combination with B-scan results in order to confirm that the delamination did indeed occur. This combination of scanning methods was one of the most thorough seen in the literature.

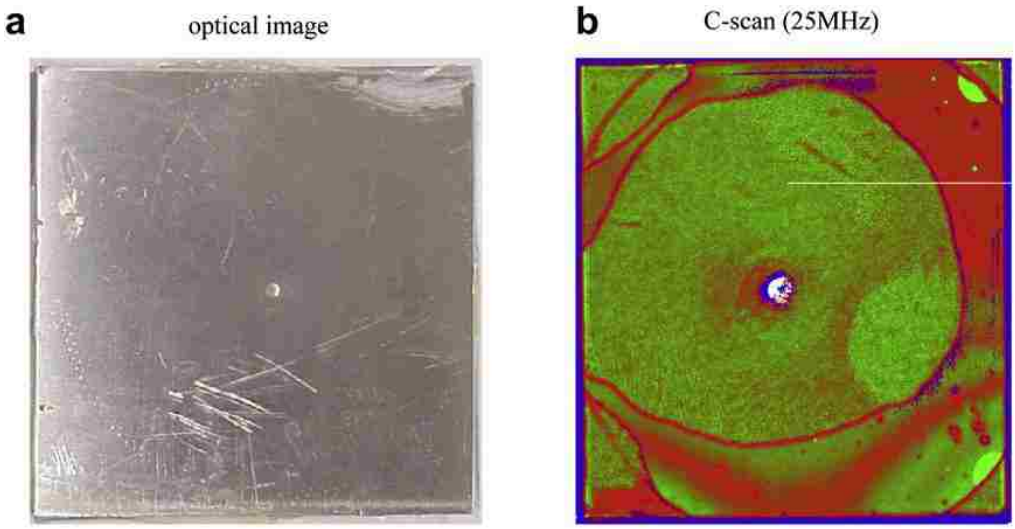

Figure 2-11 - Comparison between Optical and C-Scan Imaging [39]

By using these imaging techniques, the failure modes at very small scales can be analyzed. Additionally, the actual amount of damage could be quantified in certain cases by collecting data on how many fibers were broken due to the impact event. This could also provide data to determine the benefit that each fiber provides and how many fibers are necessary to still behave in the original desired manner.

2.2.3 Predictive Methods

A final evaluation measure is to compare the experimental results to any predictions that were made ahead of time. There are many ways in which to do this including energy balance models [9,15], stress tensor analysis [24], a spring-mass model [11,37] and finite element analysis (FEA) models [5,6,12,23,29,35,39].

Starting with the energy balance model, the equations begin fairly simple but can become more complex as they are carried through in order to predict the maximum deflection observed, or the maximum force that can be withstood. Since the impactor will be dropped from a known height, the potential and kinetic energies can easily be obtained through simple calculations. These values can then be used in the initial energy balance equation given by [39]

$$\boldsymbol{K_0 = K_t + U_{strain} + E_{balance}}$$

E. 2.5

Where K_0 is the initial impact energy, K_t is the remaining impact energy of the impactor, U is the strain energy and $E_{balance}$ is given by:

$$\boldsymbol{E_{balance} = E_{interfacial\ fracture} + E_{radial\ cracking} + E_{contact}}$$

E. 2.6

E. 2.5 and E. 2.6 came from an examination of a bi-material specimen. A more general approach can be seen in [15,47]:

$$\boldsymbol{E = E_c + E_{b/s} + E_m}$$

E. 2.7

Where *c, b/s* and *m* refer to contact, bending, shear and membrane effects of the strain energy. From this energy balance equation, the stiffness equations can be taken into account and yield the resulting energy balance equation:

$$\boldsymbol{\frac{1}{2}mv^2 = \frac{1}{2}K_{b/s}\delta^2 + \frac{1}{4}K_m\delta^4 + \frac{2}{5}\left[\sqrt[3]{\frac{\left(K_{b/s}\cdot\delta + K_m\delta^3\right)^5}{n^2}}\right]}$$

E. 2.8

Where *m* and *v* are the mass and velocity of the impactor, respectively, *K* represents the appropriate stiffness values, δ is the displacement and *n* is the contact stiffness parameter derived from the Hertzian contact law:

$$\boldsymbol{P = n\alpha^{3/2}}$$

E. 2.9

Where *P* is the applied force and α is the resulting indentation. E. 2.8 can then be used to predict the maximum deflection that will occur in the plate for a known impact energy value. Energy balance models can offer a fair approximation for the desired value, depending on the behavior of the test panels. More flexible panels would not provide such clean results, since the observed physics in large deformation problems are much more complex. In order to take this into account, Huysmans, *et al.* [24] developed a damage model for knitted fabric composites. The damage mechanisms that were examined included matrix/yarn debonding, yielding of the matrix, and the formation of macro-cracks. In this work, the team develops a model that takes into account the material properties, including Young's Modulus, the yield strength and the Poisson ratio of the test panel. These values are then incorporated into a tensor analysis that involves a von Mises stress criterion, the point of plastic strain, and the Eigen-strains. This model was only used however to predict the strength of the panels, and not the strain to failure. The team also pointed out that the model was difficult to apply to more complex knitted structures due to the method in which the material properties were calculated which was completed by examining the iso-strain conditions in the tensile direction and the iso-

stress conditions in the transverse direction. With increasingly complex knitted patterns, these directions will not line up nicely with the global coordinate system, but instead will occur in varying angles.

Another more simplistic method is the use of a spring-mass model. Reyes & Sharma [15] briefly mention this technique where the impactor and panel are modeled as rigid masses and their respective deformations are modeled as a spring between them. Richeton, *et al.* [37] took a more complex approach to the spring/mass model.

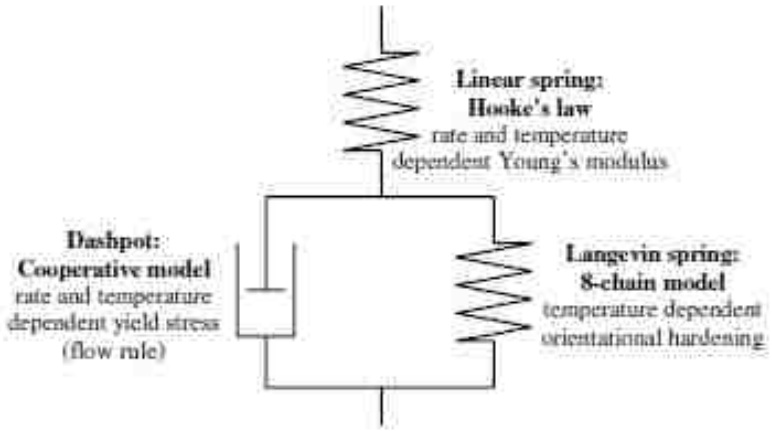

Figure 2-12 - Spring/Mass Model [37]

Figure 2-12 shows the model employed by the team that takes into account material property changes that are dependent on temperature as well as plastic flow that accounts for the strain softening of the polymer. This model examines the system at a molecular level that allows the changes that occur to be a driven by the polymer chains and their reaction with each other and the environment.

A final method that can be used for predictive purposes is finite element analysis (FEA). These models can range from fairly simplistic [9] to much more complex [12,39]. Several things need to be taken into account when performing FEA for an impact event. The first is the boundary conditions of the plate.

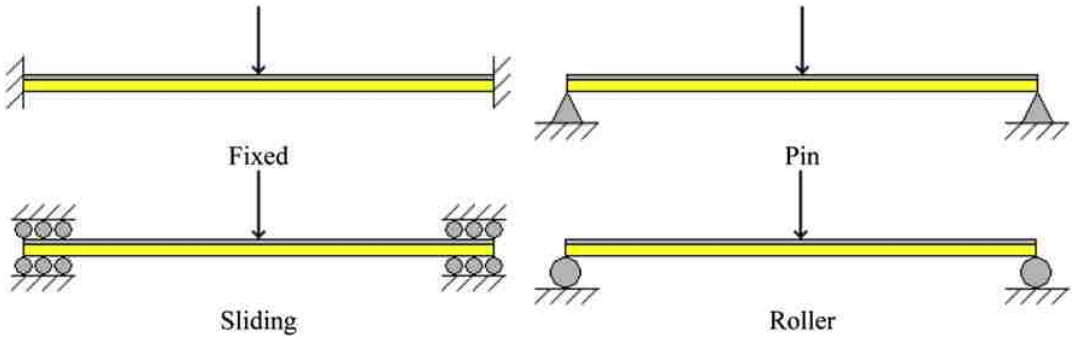

Figure 2-13 - Boundary Condition Models [39]

Liu and Liaw [39] run through a variety of simulations that use different boundary conditions until they settled on a mixed condition that allows the top surface of the plate to slide while the bottom surface remains fixed. This allowed for the desired flexibility at the mid-point of the top surface. The team also employed several failure criteria equations in order to accurately depict which failure modes would occur in the real world specimen. These criteria included delamination and crack initiation and propagation equations. In order to yield accurate results through these models, care must be taken to gather the appropriate material properties, which in some cases is rather difficult to obtain, as well as develop a model that accurately depicts the behavior of the materials as most composites will behave vastly different than the metallic structures that the finite element codes were created for.

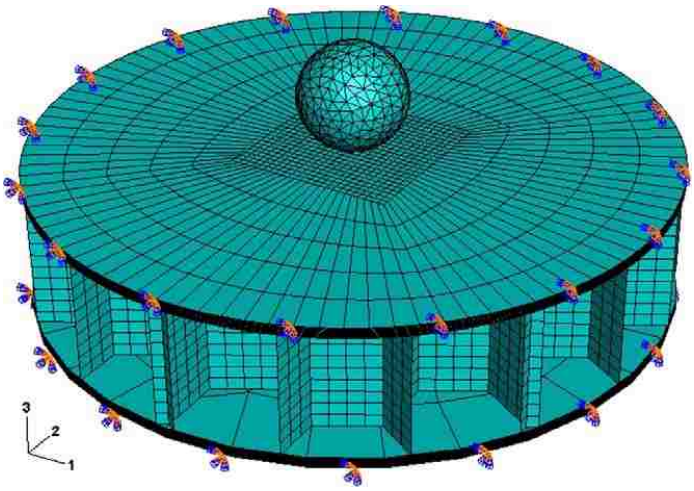

Figure 2-14 - View of 3-D Finite Element Model [12]

The next item to be addressed for the analysis is the method of contact modeling used to mimic the interaction between the panel and the impactor. A more hands-off approach would be to allow the finite element software of choice to use the integrated contact calculations in combination with two rigid bodies as seen in [12,35]. Allowing the software to perform the calculation helps to keep all of the analysis internal, including the failure analysis portion of the post-processing. Choi [11] on the other hand examined a couple of different modeling techniques for the impact event. First, a simple lumped mass could be used to represent the impactor in order to approximate the contact force history. The study found that this was an acceptable approach for quick predictions, but beyond that it was not reasonable for in-depth analysis. Choi then moved forward to use a spring element method where

one end of a spring element is attached to the composite and a lumped mass representing the impactor is located at the other end of the element.

2.3 Effects of Composite Constituents

Thus far the various impact testing methods, modeling techniques and evaluation methods have been outlined. The important part of these tests is to determine which aspects have the greatest effect on the impact performance of a material. In fiber-reinforced polymer composites, there can be considered three main constituents: the fibers, the matrix, and the interface region responsible for the bonding between the matrix and fiber. By examining the various failure mechanisms mentioned previously and applying the blame to one or more the constituents, attempts to rectify and improve the situations can be made. Cantwell & Morton [38] provide a detailed look at this topic by breaking each constituent down and examining the effect that each has.

2.3.1 Effect of Fiber

In fiber reinforced composites, the fiber is a crucial component due to the amount of loading they are responsible for. There are a variety of changes in the fiber that can be made in order to improve the impact resistance of composite including the fiber orientation, the length (i.e. continuous vs. chopped strand), physical properties (i.e. strength or stiffness), and the volume percentage. One of the most significant changes in the fiber is the material choice. Currently, while

other novel material choices are available, the common choices of material can be most simply broken down into three main choices: glass-fiber, carbon-fiber, and aramid type fibers (i.e. Kevlar®). Of course each of these fiber types possess varying strength and stiffness as well as processing capabilities as discussed earlier. An early study by Beaumont, *et al.* [48] examined the differences between 3 such fibers. The study found that the carbon based fibers exhibited more catastrophic failures, while the E-glass and aramid fibers dissipated energy much better to allow for more progressive failures. This allowed the authors to establish a "ductility index" defined as the ratio of propagation energy to initiation energy, leading to a quantifiable conclusion that the aramid fibers exhibited superior energy absorption capabilities in the study. A similar conclusion was drawn by [49] in that the E-glass reinforced composites would exhibit much better performance in static testing, while the aramid reinforced composites would perform better with the dynamic loading. This study also noted the importance of the fabric structure by examining the impact performance of unidirectional E-glass fiber reinforcement versus the same material in a woven structure. It was concluded that the unidirectional pattern was a better choice for static loading, while the woven structure should be preferred for impact or dynamic loading.

Sayer, *et al.* [40] also examined these aspects to a certain degree by combining both glass and carbon fibers used in combination into what is deemed a hybrid composite. This study was also interested in the orientation and stacking sequence

to a certain point with impact studies performed depending on which material was struck first.

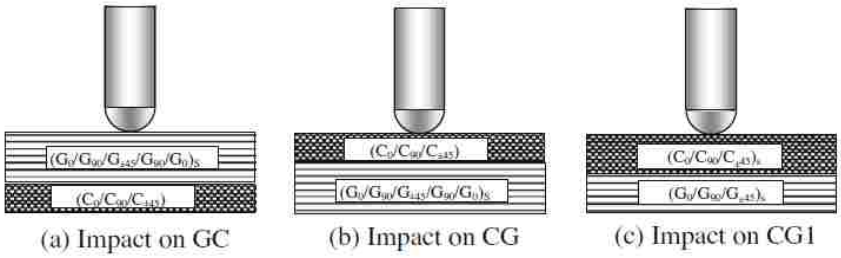

Figure 2-15 - Schematic of Impacted Surface of Hybrid Composites [40]

Hybrid composites were also studied by [44] by once again combining carbon fiber and glass together to study the impact performance of the hybrid versus the stand alone versions of each type. The study found that the addition of glass mats to the carbon fiber reinforced composites resulted in improvement of impact behavior in regards to the energy absorbed as well as residual physical properties. Through these studies of material choices the common result has been poor performance of carbon fiber as a reinforcing material in the case of dynamic loading, with aramid based fabrics providing the best performances and E-glass in between.

Another aspect of reinforcement selection to keep in mind is the geometry in reference to both the length, as well as the diameter, of the fiber. Two studies by Thomason [50,51] examine the influence fiber diameter, as well as fiber content, have on the mechanical performance of a glass-reinforced composite. It was found that the testing parameters caused variations in the dependency of the performance

on the fiber length and diameter. For example, whether a notched or un-notched impact test was performed, the trends observed relating fiber diameter and content to impact performance would be reversed. This observation indicates the difference the fiber has on the incident energy dissipation, revealing that change in diameter will greatly influence the onset of damage.

2.3.2 Effect of Matrix

The matrix in a fiber reinforced composite serves several purposes including providing a medium in which to bind the fibers together as well as to evenly distribute an externally applied load amongst these fibers [1]. This allows, as mentioned earlier, for the fibers to feel the brunt of the loading. Another purpose of the matrix is to protect the fibers from damage due to abrasion or chemical reactions; otherwise the fiber performance would be greatly compromised. In consideration of the changes or choices that can be made in respect to the polymer matrices used in these composites, the number of variables is lower than the number available for reinforcing fibers. The level of ductility and hardness is one of the main issues that can be addressed. One such study that examined this material difference was performed by Sutherland & Soares [52] with the comparison of orthophthalic polyester resin and an epoxy resin in combination with E-glass woven reinforcement. Although, the impact performance was fairly similar between the two materials, the damage modes that were exhibited were found to be the main the difference. These damage mode differences are important in regards to the

post-impact evaluations since delamination will greatly reduce the stability of the composite material. Another study by Morais & D'Almeida [53] examined the impact performance based on the thickness of the laminates which showed a direct relationship to the amount of incident impact energy.

2.3.3 Effect of Interface

The interface region of a composite is defined by the adhesion properties between the matrix and reinforcing fibers. Several studies [22,43,54,55] have examined the bonding properties that occur in this region and how potential surface treatments affect these properties. Kim & Mai [55] discuss the control of the interface in order to tailor the fracture mechanisms and energy absorption capabilities of polymer composites. The study found that a stronger interface will result in a more brittle fracture mode with relatively low energy absorption capabilities, while a weaker interface will cause a multiple shear mode with higher energy absorption. This concept was also investigated by Hirai, *et al* [43] in which surface treatment of fibers using a silane coupling agent was performed and the mechanical properties of the various treatment levels and agents were examined. The main difference between the two coupling agents occurred at the chemical level where one treatment could react with a double bond found in the matrix polymer chains, while the other agent could not. It was found that the treatments had a significant effect on the physical properties of the composite, including its strength and moduli. These properties were considered to be root cause of any differences in

impact performance, including residual strength. A similar study by Jensen & McKnight [54] also examined the use of varying concentrations of silane coupling agents and reached similar conclusions that the chemical reactions between the agent and polymer matrix have the largest effect on the energy absorption capabilities as well as residual strength following an impact. Additional experiments performed by Bekisli [56] and others have shown that poor adhesion facilitated by ensuring chemical incompatibility between fiber coatings and the matrix can be desirable in order to maximize the deformation before the critical stretch occurs in knitted materials.

3 Background Formulation

This chapter will provide background formulation for future problems so that attention with the subsequent chapters can be devoted to details regarding the actual setup of the solutions, results, and discussions rather than the details associated with the background calculations.

3.1 Finite Element Options

As much of the finite element work was performed using commercially available software in ANSYS 13.0, the full formulation of how the finite element method works will not be explored in this section. Several resources are available [57–60] and should be referred to in order to fulfill the background necessary to understand finite element theory. On the other hand, the unique options available that will be applicable to the future simulation models will be discussed here in order to highlight the properties associated with the solution techniques.

For the modeling portion of this paper, large deformations are expected which turns the problem into a highly non-linear one, both in terms of material behavior and strains. In order to account for this, solution control must be implemented in ANSYS so that the proper solver methods are activated. Solution control needs to be used during most non-linear analyses as well as when contact elements are present [57]. First, by specifying that large-deflections will be present, the solution will include these effects, where the default solution methods ignore these effects. This

specification is implemented by employing the built in NLGEOM command in ANSYS 13.0. For effectively solving the non-linear problems, the Newton-Raphson solution method was specified. An in-depth explanation and derivation of the Newton-Raphson method can be found in [61] where for a non-linear system given as:

$$\mathbf{F}(\mathbf{X}) = \mathbf{0} \qquad \textbf{E. 3.1}$$

It is shown that the extension of the Newton-Raphson method is:

$$\mathbf{X}^{(k+1)} = \mathbf{X}^{(k)} - \left[\mathbf{F}'\left(\mathbf{X}^{(k)}\right)\right]^{-1}\mathbf{F}\left(\mathbf{X}^{(k)}\right) \qquad \textbf{E. 3.2}$$

Where $\mathbf{F}'\left(\mathbf{X}^{(k)}\right)$ is the Jacobian Matrix comprised of the partial derivatives of $\mathbf{F}$ evaluated at $\mathbf{X}^{(k)}$.

Although it is commonly the default solution method due to its speed of convergence and reliability, there are many variations included in ANSYS in order to modify the method. These variations are based on how often, and which form of the stiffness matrix is updated. In certain methods, the tangent stiffness matrix is only updated at each substep, but is not applicable to large-deformation analyses. Other versions of the method only base the calculations on the initial stiffness matrix and continue to use this matrix for each iteration of the solution which, again, is not applicable for large-deformation problems examined in this study. The chosen method for the accurate simulations examined in this study is the full Newton-Raphson Method, where the stiffness matrix is updated at every equilibrium

iteration. In more clear terms, the simplest form of the discretization process shows a set of equations represented by:

$$[K]\{u\} = \{F^a\}$$

E. 3.3

Where *K* is the coefficient matrix representing the stiffness of the material, *u* is the vector of unknown degree of freedom values and F^a is the vector of applied loads. Since the coefficient matrix is a function of the unknown degree of freedom values or derivatives based on these values, the equation is non-linear and can be written as the equations below to show the Newton-Raphson setup:

$$[K_i^T]\{\Delta u_i\} = \{F^a\} - \{F_i^{nr}\}$$

E. 3.4

$$\{u_{i+1}\} = \{u_i\} + \{\Delta u_i\}$$

E. 3.5

Where K^T is the tangent matrix, the subscript *i* represents the current equilibrium iteration, and F^{nr} is a vector of loads corresponding the internal loads found in the element. It was found that the Line Search option greatly improved the standard Newton-Raphson approach by scaling the solution vector by introducing a scalar term that changes the amount of Δu_i is used since using the full term can lead to instabilities in the solution caused by taking too large an increment. This is accomplished by introducing the line search parameter, *s,* into E. 3.5 yielding:

$$\{u_{i+1}\} = \{u_i\} + s\{\Delta u_i\}$$

E. 3.6

The line search term falls in the range of $0.05 < s < 1.0$ and is automatically determined by minimizing the energy of the system. The scaled solution is then used to update the current degree of freedom vectors so that the next iteration can be performed.

3.2 Numerical Analysis

The analyses of the problems discussed below often require a numerical method in order to find viable solutions. A brief discussion involving these techniques will be discussed in order to highlight the background calculations involved in the subsequent chapters. In addition to the Newton-Raphson method discussed in the section above, numerical integration methods will be used to process the experimental data obtained below. The method employed will be the Trapezoid Rule where the area under a curve can be computed by creating basic trapezoid shapes from point to point.

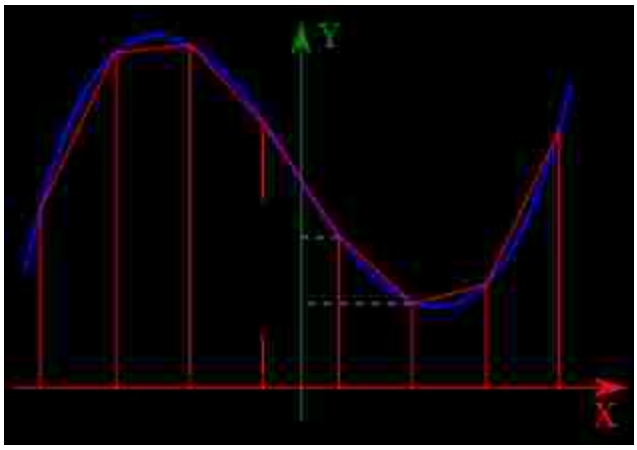

Figure 3-1- Trapezoid Rule Inspired by [61]

A basic trapezoid rule a single subinterval is given as:

$$\int_{x_i}^{x_{i+1}} f(x)dx \approx \frac{1}{2}(x_{i+1} - x_i)[f(x_i) + f(x_{i+1})]$$

E. 3.7

So that the total area under the curve is given by the composite trapezoid rule seen as:

$$\int_{a}^{b} f(x)dx \approx \frac{1}{2}\sum_{i=0}^{n-1}(x_{i+1} - x_i)[f(x_i) + f(x_{i+1})]$$

E. 3.8

Where all terms refer to the values demonstrated in Figure 3-1. This method was beneficial in solving for the area under curves presented in the next section, where these integrations will yield important values. Although the values will be obtained through numerical approximations, the data points collected appear along linear paths, as opposed to curved paths that may result in larger errors.

4 Impact Testing of Knit Reinforced Composites

Previous studies [23] have examined the deformation properties associated with knit reinforced polymer composites by way of analyzing the critical stretch value which occurs when the loop structure found in knitted patterns reaches the upper limit and the fibers become parallel and "lock" into carrying all of the applied load. As discussed in an Chapter 2, many studies are available that have examined the impact behavior of traditional woven reinforced polymer composites, while similar studies using knitted reinforcement are very rarely found in the literature.

4.1 Objective and Technical Approach

The objective of the research conducted in this study is to characterize the impact behavior of knit reinforced polymer composite materials, specifically; to examine the feasibility of employing such materials for use in applications that will undergo collision events due to the decreased cost associated with the knitted composites versus the more commonly employed woven versions.

An in-depth energy balance equation based on known materials properties and expected results of the impact, including a rebound event, was created for comparison to the impact test results. A multitude of impact tests using an instrumented drop weight impact tower were performed in order to characterize the impact performance of the loose-knit reinforced polymer composites.

4.2 Custom Built Impact Testing Apparatus and Setup

The impact testing apparatus is comprised of a clear PVC tube attached to a current drop tower. The tube design will be implemented instead of the pre-fabricated plate style drop tower, as overviewed in 2.1, as it is believed that the plate design will initially provide too much force at the impact.

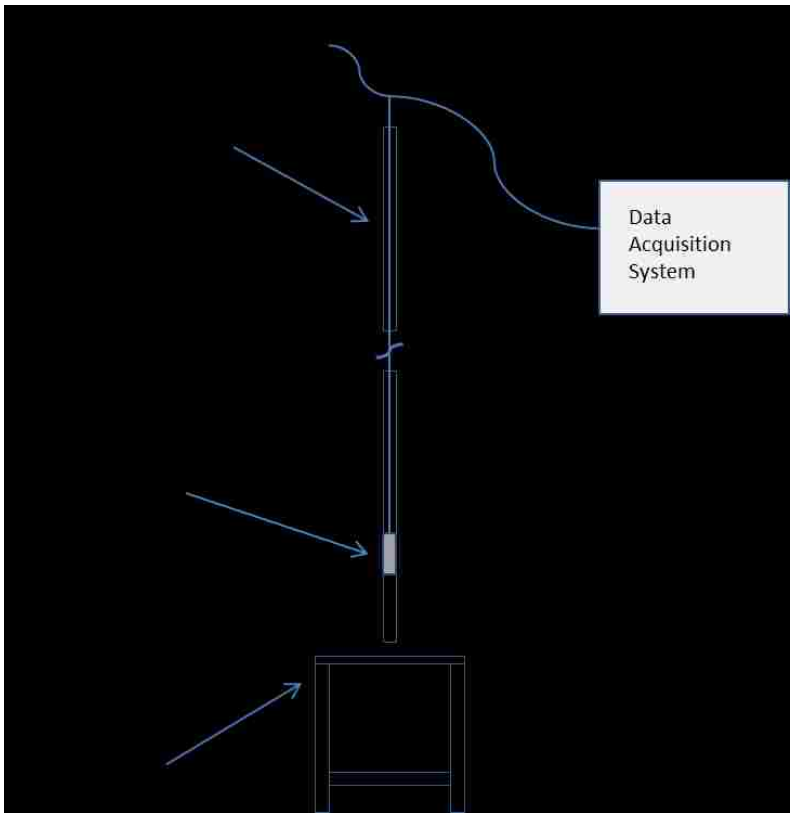

Figure 4-1 - Impact Testing Setup Schematic

Figure 4-2 – Image of Drop Tube and Stand

Figure 4-1 and Figure 4-2 shows the testing setup for the impact events. It includes an adjustable impact stand that allows for a 20.3cm x20.3cm (8”x8”) or 20.cm x 25.4cm (8”x10”) window used for the test panels. This can allow for the observation of how the geometry of the test panel affects its performance. The current dimensions were chosen based on the limitations of the available compression molding machine used to fabricate the composite test specimens, as well as geometrical criteria for the impact event. To minimize the effects that the edges of the clamping structure would have, the impact events were designed to occur at least 7.62cm (3”) from the specimen’s edge. This should allow the maximum amount of energy to be transferred through the reinforcing yarns/fibers, thereby dispersing the energy in the desired fashion. The test setup also includes the aforementioned clear PVC tube that will allow tracking of the drop weight during the event as well as prior to the drop when the initial height is of upmost importance. Finally, the drop weight was affixed with a threaded Dytran 3034B4 analog accelerometer that was connected through a Dytran 4102C current source to a Data Translation DT9816 data acquisition module. This module was connected to an available computer in order to collect the data produced by the accelerometer voltage readings taken at a sample rate of 1000Hz.

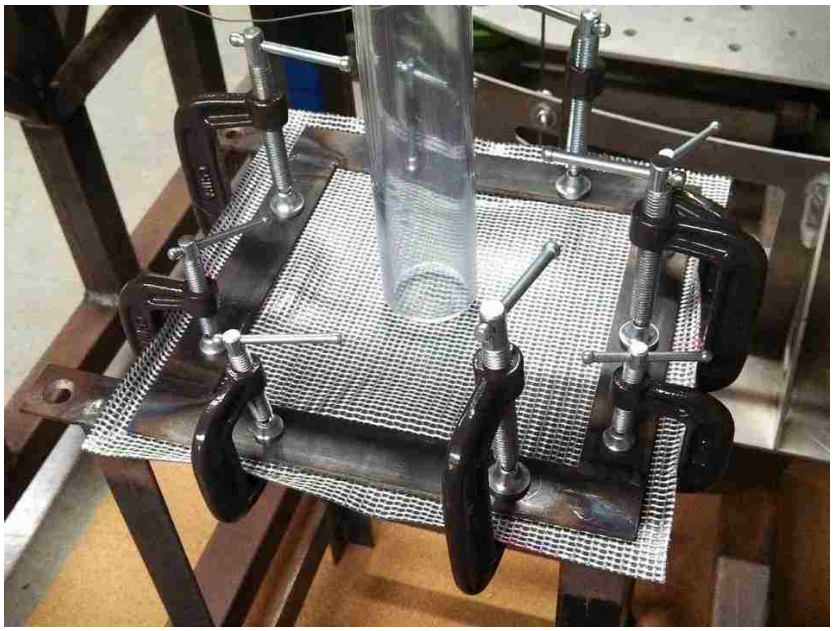

Figure 4-3 - Clamped Panel under Drop Tube

The most common impact geometry, as well as the one specified in ASTM standards, is a hemispherical impactor. A 2.54cm (1”) diameter and 7.62cm (3”) long drop weight with a hemispherical tip was machined in order to avoid issues that may arise with the use of an interchangeable tup geometry as seen in other testing rigs.

Figure 4-4 - 1" Diameter Machined Impactor

This impact geometry will also allow for the reinforcement fibers to behave in low-velocity impact test, whereas a conical shaped impactor may strike a “window” between fibers, thereby resulting in the polymer acting as the sole energy

dissipation avenue. The diameter of the impactor was chosen based on the desire to contact between six to ten fibers in each direction. Due to the loop spacing a 2.54cm (1”) diameter would accomplish this goal. This principle was examined by [20] as the study found conical projectiles to most easily penetrate through a fabric due to the tendency to push aside the principal yarns. This study was more concerned with the analysis of the fabric itself and found that cylindrical projectiles with a flat striking surface and a spherical projectile of a similar radius resulted in nearly identical impact responses. This is not expected to be the case with the addition of the polymer matrix as the sharp geometrical edges on a cylindrical flat punch could cause severe stress concentrations resulting in increased chances for failure when compared with a smooth spherical impactor.

4.2.1 Data Acquisition

In order to collect data from the impact events an accelerometer was threaded into the drop weight and the data was transmitted to a computer through the methods discussed above. By examining the plots produced by this data, combined with simple equations of kinematics, the desired values can be obtained.

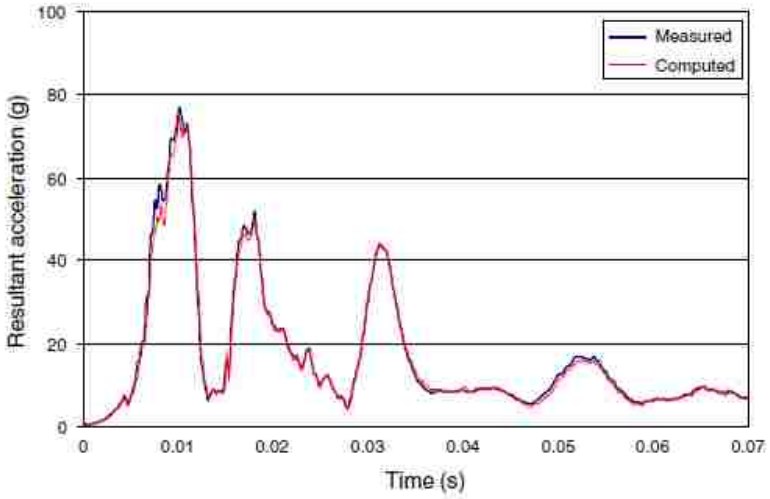

Figure 4-5 - Typical Acceleration vs. Time Example Plot [62]

Figure 4-5 shows the acceleration vs. time plot of an object mounted with multiple accelerometers during a drop test performed in order to examine head injuries. The slope of the plot should be constant near zero for the free fall for a very short period, followed by a point where the impactor first makes contact with the panel, resulting beginning of the sudden rise as seen in Figure 4-5. The slope should continue in some form, whether it is a linear or non-linear relationship until it reaches an inflection point, which will coincide with the maximum acceleration felt. Once the plot approaches the x-axis again, the acceleration will drop to zero, thereby corresponding to the maximum deflection. If the assumptions of a rebound event are indeed correct, the drop weight should experience acceleration in the negative direction (upward) along the same path until it touches or comes near the horizontal axis, and the area under this curve will represent the initial upward velocity as the projectiles loses contact with the surface. This velocity is of interest

as it is vital to understanding the energy dissipation. This will be used in order to determine the amount of energy transferred back into the system, so that the total amount of energy absorbed can be calculated.

4.3 Material Choices

For the polymeric matrix material, there are several avenues that can be explored. The first is the use of a thermoplastic elastomer (TPE) that will be compression molded into lamina sheets. These can then be combined with the fabric reinforcement to make composite panels. One specific type of TPE will be Pebax® 2533 SA 01 produced by Arkema that is tailored for food uses. These TPE lamina sheets will then be combined with simply course weft knit fabric reinforcement layers comprised of knitted E-glass fiber created on a Silver Reed SK840 knitting machine.

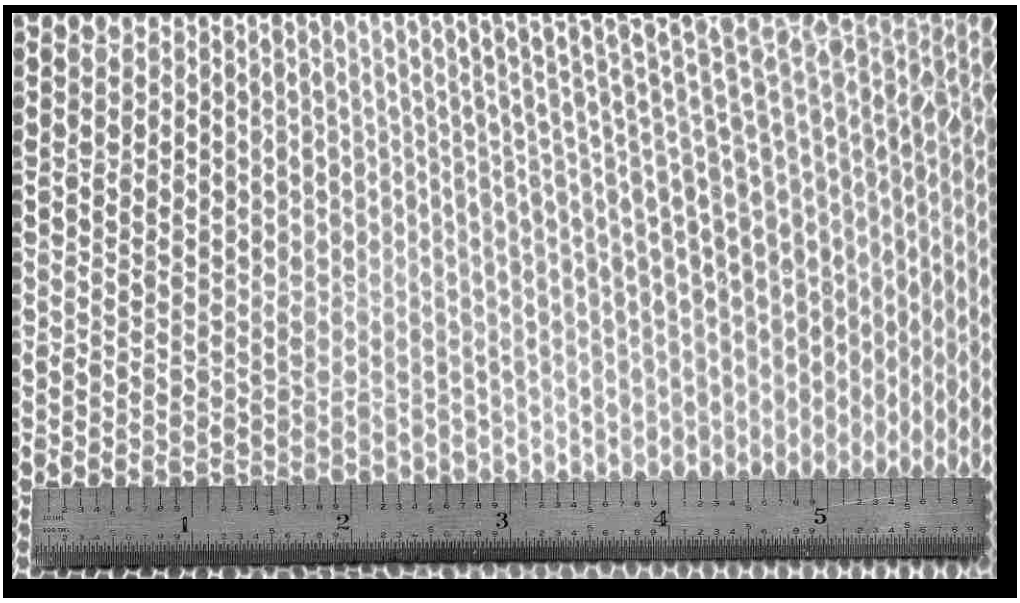

Figure 4-6 - Image of Weft Knit Reinforced TPE

Figure 4-7 - Silver Reed SK840 Knitting Machine

Additionally, the roofing company GAF provided sample sheets of a Thermoplastic PolyOlefin (TPO) that is used in commercial roofing applications. The production method for the GAF roofing composite employs a co-extrusion technique in order to adhere two different layers of TPO together with a knitted reinforcing fabric in between them. An example of half of this configuration, i.e., TPO layer missing, can be seen in Figure 4-8.

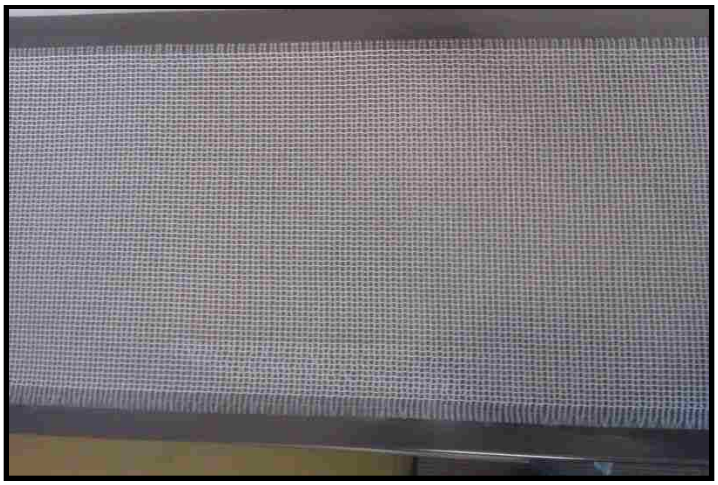

Figure 4-8 - Fiber Adhered to TPO

4.4 Evaluation Methods

Following the impact event, several evaluation measures were taken as outlined in 2.2. The first, and possibly most important, was to measure the permanent deformation. The depth of the indentation as well as the radial affected zone was important to note. This allowed for further verification of the models created as well as the calculations performed using the accelerometer data. Another method of evaluation included testing the specimen again to examine the performance degradation that occurred due to the first impact event. This data will be vital in determining the fatigue related properties of the test material. Finally, all of the test data will be compared to the predicted values that were obtained from the aforementioned energy balance equation as well as the finite element analysis results. The energy balance equation will use many of the same principles that are set forth in [15] by using the best known material properties of the test panels, the

maximum deflection should be able to be predicted in the same basic manner as Reyes and Sharma did.

4.5 Results

Several impact tests were performed through the outlined methodology above and the data was processed in order to extract the necessary values for use in the calculation of the amount of energy absorbed by the fiber reinforced polymer panels. Tests were carried out under impact velocities between 4.5-6.2m/s (10.1-13.9mph) based on drop heights of 1.08m (42.5”) and 1.89m (74.25”) from the surface of the test specimen. Voltage vs. time plots as seen in Figure 4-9 were acquired through Data Translation’s QuickDAQ 2013 software, which could subsequently export the data into Microsoft Excel. At this point the data can be converted from the raw input voltage into the desired acceleration readings by taking into account the sensitivity of the accelerometer according to the manufacturer’s specifications.

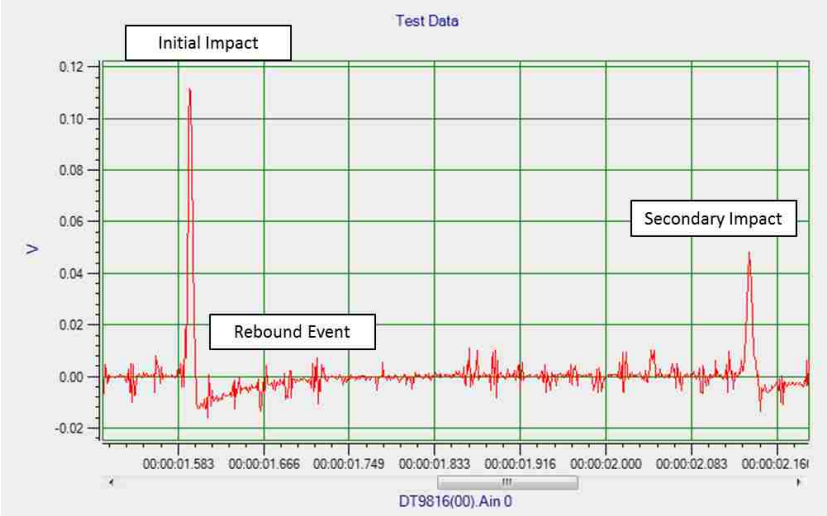

Figure 4-9 - Voltage vs. Time Plot

Once the raw data was processed, it could be broken down into three main sections of the test: initial impact, rebound event, and the secondary impact. From here integration of the acceleration vs. time plot could be used in order to calculate the initial velocity, and therefore initial impact energy, of the impactor.

$$\Delta V = V_{t_2} - V_{t_1} = \int_{t_1}^{t_2} a(t)dt$$

E. 4.1

As this value was important to obtain, a numerical integration approach based on the trapezoid rule discussed in 3.2 was employed. These results were consistent with initial assumptions based on simple kinematic calculations where the potential energy of the impactor based on the drop height was converted to kinetic energy at the end of the tube, resulting in an impact energy of near 7.1 J (8.85 lbf-in) for the 1.89m drop height.

$$\Delta x = x_{t_2} - x_{t_1} = \int_{t_1}^{t_2} v(t)dt$$

E. 4.2

Curve fit tools match a 5th degree polynomial to the acceleration vs. time data in order to provide values to use for analysis in finding the maximum deflection found through E. 4.2. Figure 4-10 shows the distribution of the maximum deflection found in each of the impact tests performed. The red line shows the average value for comparison purposes, while "high drop" refers to a drop height of 1.886m (74.25") and "low drop" refers to a drop height of 1.079m (42.5").

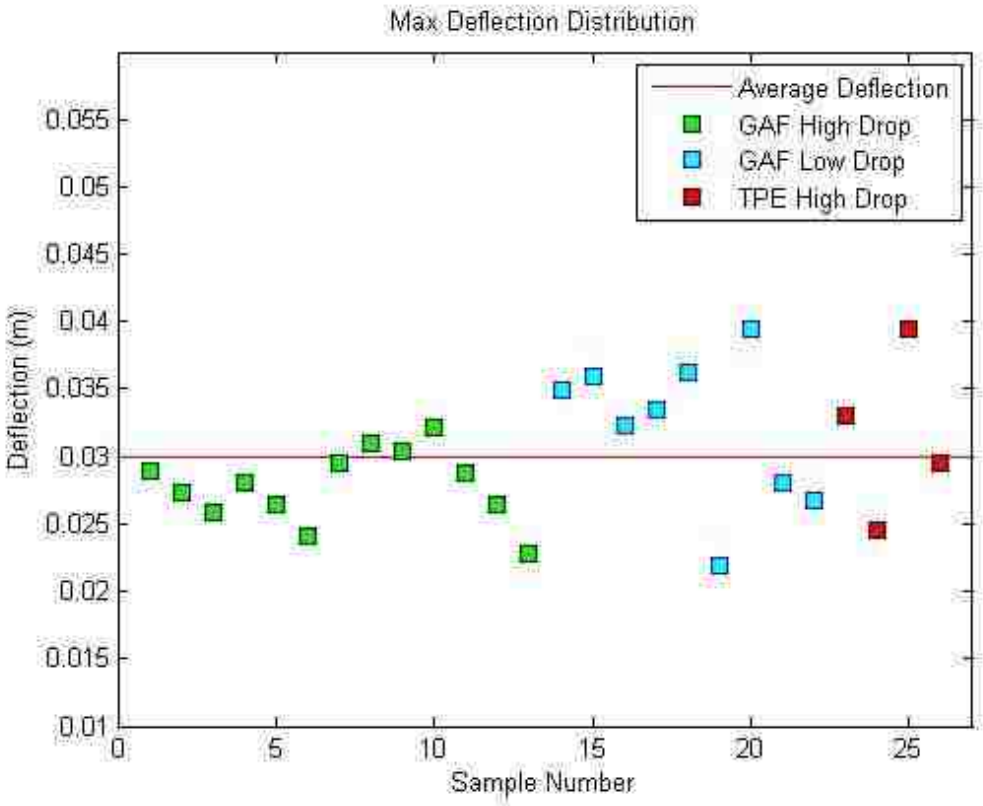

Figure 4-10 - Maximum Deflection Distribution

With the maximum deflection accounted for, the energy balance equation could be completed in order to calculate the amount of energy absorbed by the test panel. Referring back to E. 2.5, we see that the impact energy will be transferred into the energy remaining in the impactor, through both potential and kinetic energies, strain energy of the impacted surface and the balance which accounts for the damage incurred by the impacted surface. The strain energy can further be broken down into recoverable and un-recoverable forms where the un-recoverable form is associated with the plastic, or permanent, deformation of the impacted structure. Therefore, accounting for the rebound event, E. 2.5 becomes:

$$\Delta KE_{Impact\,1} + \Delta PE_{Impact\,1} = U_{Total\ Strain} = \Delta KE_{Return} + \Delta PE_{Return} + E_{damage} \quad \textbf{E. 4.3}$$

Where:

$$KE_{Impact\,1} = \frac{1}{2} m_{impactor} V_i^2 \qquad KE_{Return} = \frac{1}{2} m_{impactor} V_r^2 \quad \textbf{E. 4.4}$$

$$\Delta PE = m_{impactor} g \delta_{max} \quad \textbf{E. 4.5}$$

Where $m_{impactor}$ is the mass of the impactor system, including the drop weight, accelerometer and eye hook used to lift the impactor into place, V_i is the initial velocity right before impact, V_r is the rebound velocity calculated where the impactor is no longer in contact with the specimen, g is the Earth's gravitational constant, and δ_{max} is the maximum deflection.

Table 1 - Values used for Energy Calculations

Term	Value
$m_{impactor}$	0.3855 kg
V_i	* Values calculated for each test
V_r	* Values calculated for each test
g	9.81 m/s^2

By solving E. 4.3 for the term E_{damage}, the total amount of energy absorbed by the panel can be found as this term will include both the damage induced on the reinforcement fiber and polymer, as well as the plastic deformation left in the polymer. Figure 4-11 shows the distribution of damage energy calculated for each impacted sample. Many of the values found to higher than the average line correspond to large apparent plastic deformation or failure, while the points found to be lower than the average line generally correspond to barely noticeable fiber damage as well as much smaller permanent deflection which will be discussed in further detail in the next section.

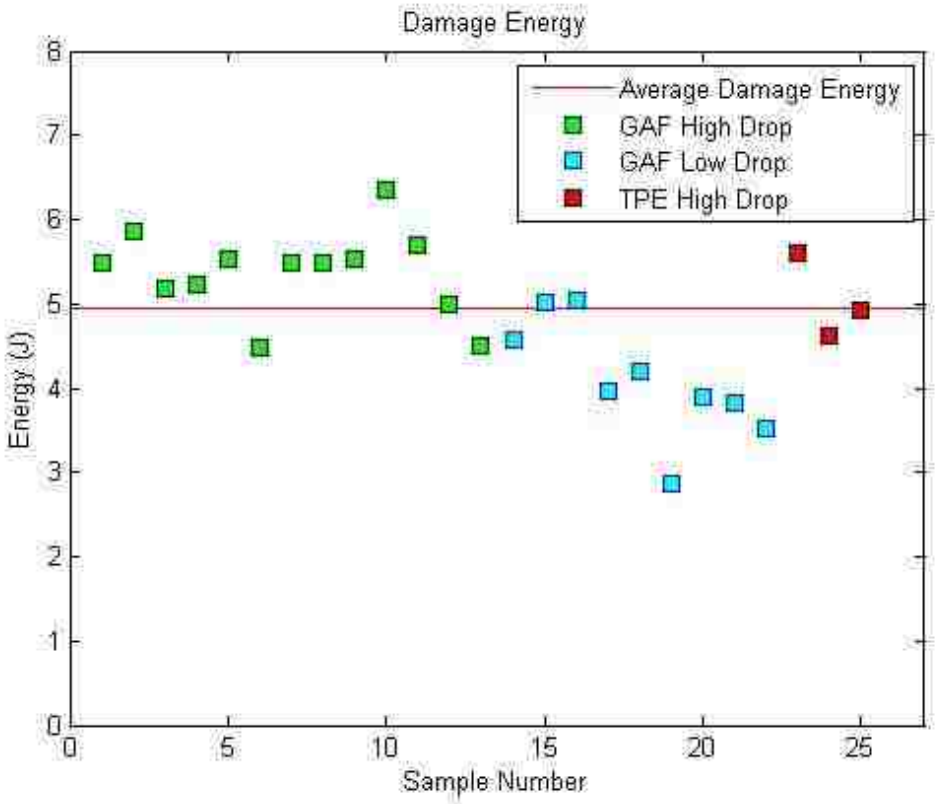

Figure 4-11 - Damage Energy Distribution

Taking an example from Atas & Sayman's [17] examination methods, Figure 4-12 shows the impact energy vs. the absorbed energy through damage mechanisms. The red diagonal line shows the points at which all of the energy is absorbed and retained by the panel. In this case, no energy would be returned to the system and depending on the situation, this could be beneficial or not, since this instance would likely result in catastrophic failure of the composite panel.

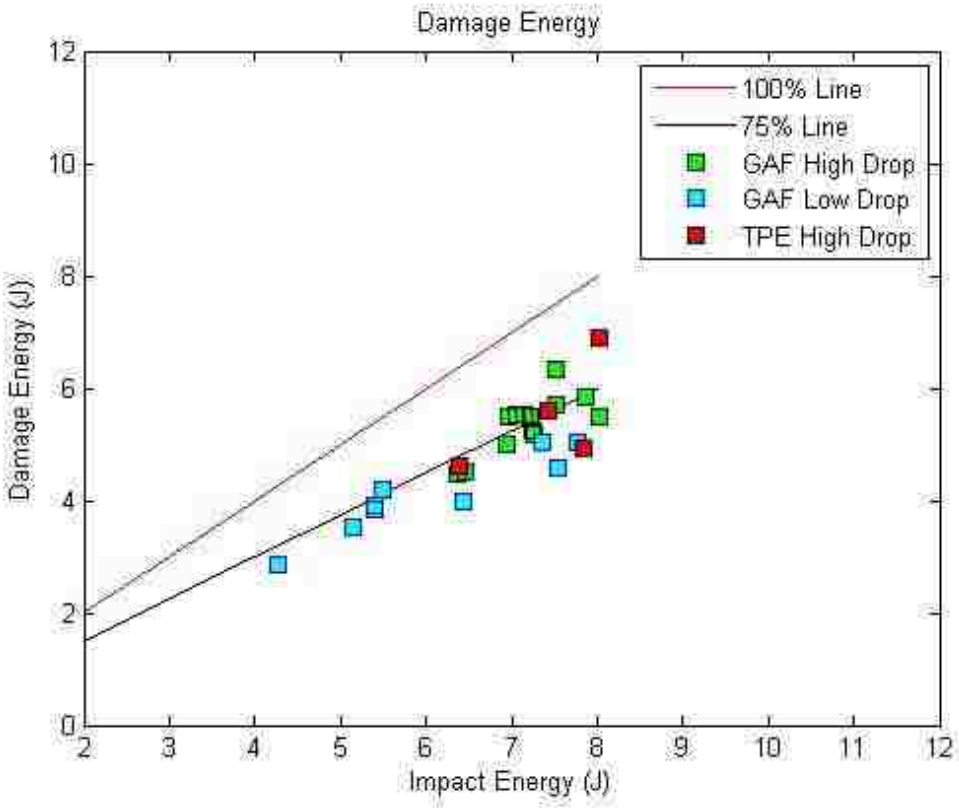

Figure 4-12 - Impact Energy vs. Absorbed Energy

Figure 4-12 shows that the panels absorbed a portion of the energy, while the rest of the impact energy was returned to the system. In many cases this would be undesirable as the thought behind the flexible composites would be for use in slowing objects down to a stop and removing the energy from the system through damage mechanisms. These tests show that around 25% of the impact energy is returned to the system in which case the motion would occur in the opposite direction of the initial impact.

Due to limited availability of material and processing capabilities, only a few samples of Pebax TPE with E-glass knitted fiber were created or tested as seen in the

figures above. Inconsistency with knitting resulted in fewer usable samples. Results were still fairly consistent with the GAF material as much of the energy was returned to the impactor with around 2J being absorbed through damage mechanisms.

4.6 Post Impact Analysis

The first method used to analyze a specimen following the impact test was examining for easily visible localized failure of either the polymer or reinforcing fibers. This could be accomplished immediately following the removal of the specimen from the clamped test stand. In many cases, there were not any clearly visible signs of failure, but other specimens exhibited polymer failure in line with the reinforcement fibers as seen in Figure 4-13.

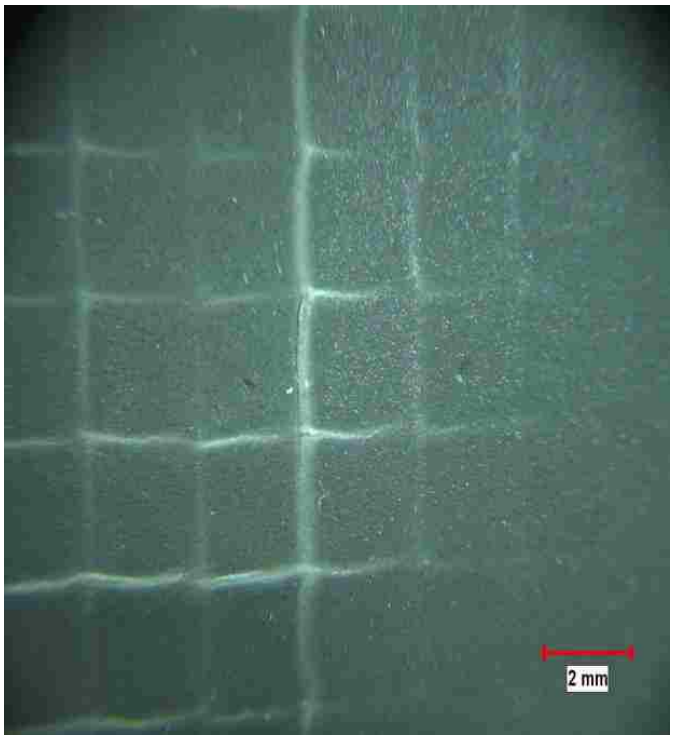

Figure 4-13 - Image of Polymer Yielding and Failure of One-Sided GAF Material

Reinforcement fiber/yarn failure was also a common energy absorption method as seen in Figure 4-14. This figure shows localized failure in the impact zone through delamination from the polymer surface, as well as fiber breakage.

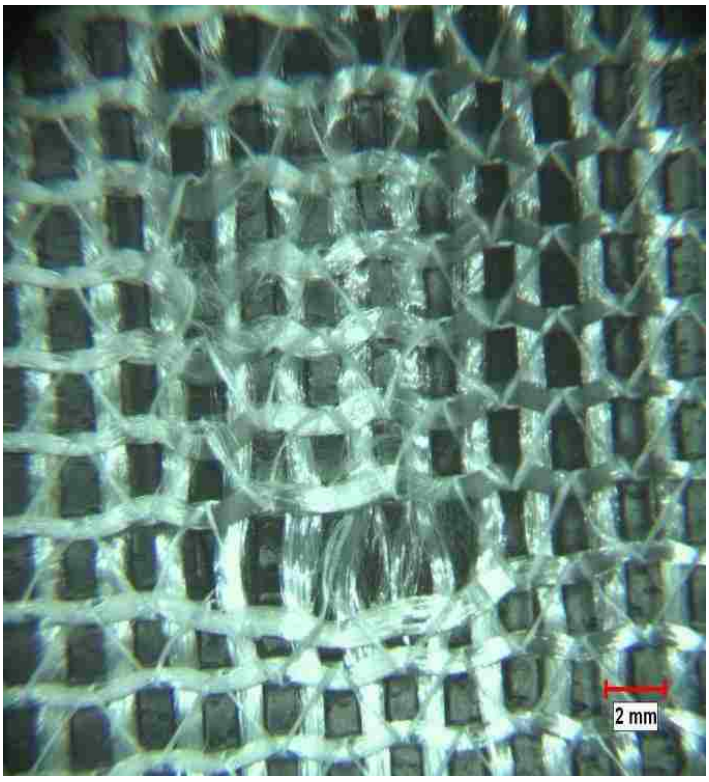

Figure 4-14 - Image of Fiber Failure and Delamination of GAF Material

As outlined in Section 4.4, the permanent deformation of the panels was measured in order to quantify the plastic strain experienced during the impact event. As seen in Figure 4-15, examining the backside of the panels creates an easier to measure protrusion than measuring the depth of the permanent indentation that would be found by analyzing the impacted side of the panel. Radial measurements corresponding to the affected impact zone were measured where the polymer was

no longer continued in its current plane. In addition to this, the height of the impact bulge was measured. Together these measurements allowed for the calculation of the permanent strain experienced by the specimen.

Figure 4-15 - Permanent Deflection of GAF Material

By assuming the deflection to behave along a radius of curvature, the strain can be computed based on the radius of the affected zone and arc length of the permanent deformation found through the use of trigonometric calculations:

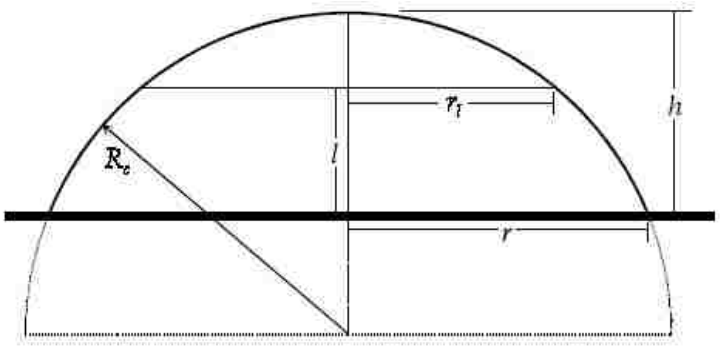

Figure 4-16- Schematic of Radius of Curvature Calculations

$$R_c = \frac{r^2 + h^2}{2h}$$

E. 4.6

$$s = r \sin^{-1} \frac{r}{R_c}$$

E. 4.7

Where *s* is the arc length, *r*, *h,* and *Rc* represent the radius of the affected area, height of the protrusion, and calculated radius of curvature, respectively, as demonstrated in Figure 4-16. The permanent strain was then found through:

$$\varepsilon = \frac{s - r}{r}$$

E. 4.8

Measurements were taken along the machine- and cross machine-directions of the GAF provided specimens in correspondence with the manufacturing method in which the samples were produced. This directional notation is discussed in greater detail in the next chapter.

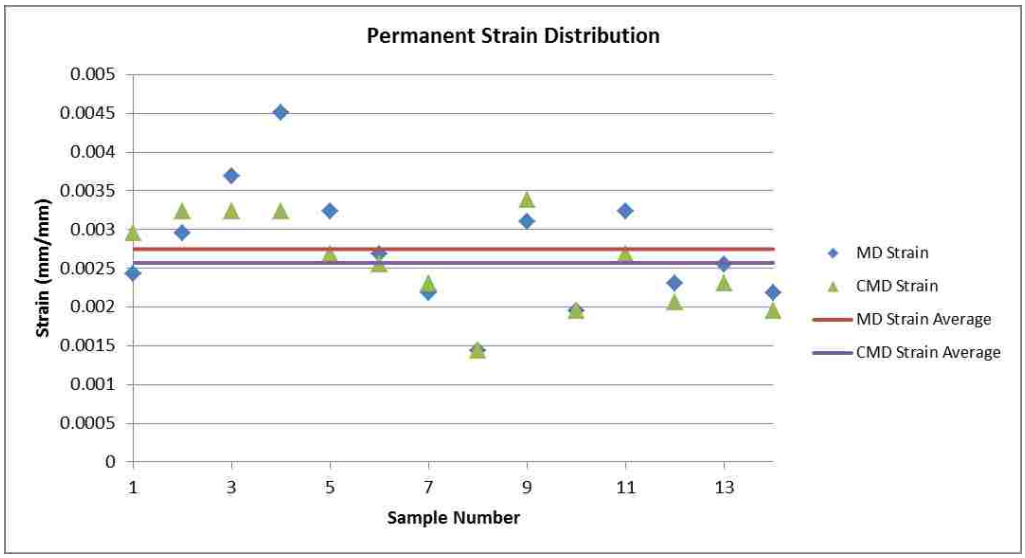

Figure 4-17 - Permanent Strain Distribution for Single Impact for GAF Material

Again, only a small number of tests were performed using the knitted E-glass reinforced TPE panels. Post impact analysis of the samples did not exhibit any visible signs of failure or damage and permanent strain was found to be a great deal less than that found in the GAF material at less than 0.001mm/mm in any direction.

These measurements were difficult to obtain due to the barely detectable changes in the material. The same geometric evaluation methods employed for the GAF material were again used for the E-glass reinforced TPE samples.

As discussed earlier, another method of evaluating the impact performance of a material is subjecting the specimen to multiple impacts. This was performed on selected test panels with 3, 5, 7 full drops from the constant drop height of 1.89m (74.25”). After all of the impact events had been performed, the panels were again analyzed for permanent deformation and failure.

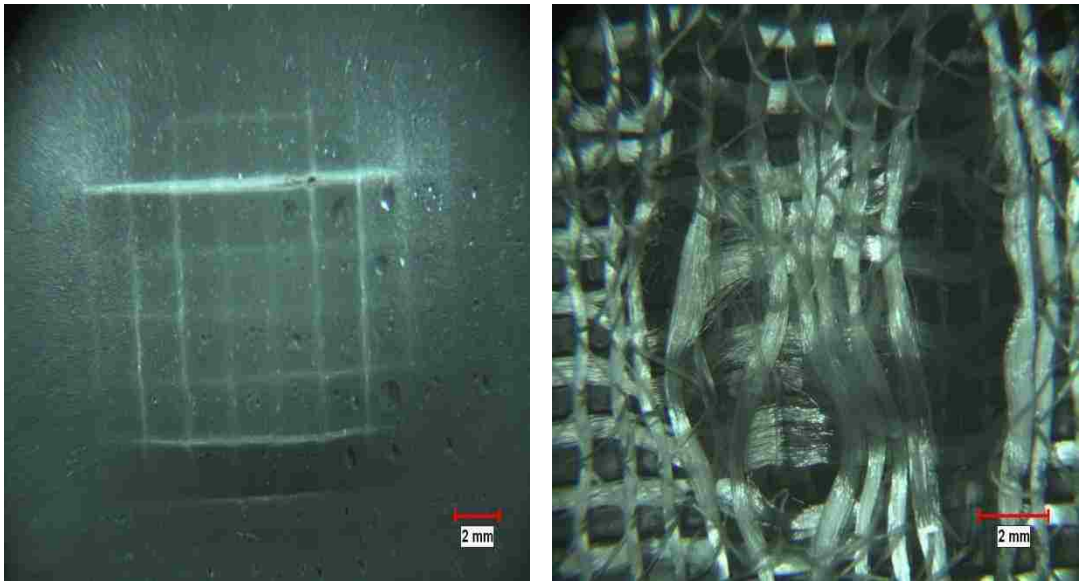

Figure 4-18 - Images from Panel Subjected to 7 Impacts

Figure 4-18 shows the much higher levels of failure and deformation than those seen in Figure 4-13 and Figure 4-14 caused by single impact. This can also be seen in Figure 4-19 where permanent strain measurements were much higher than those found in the single impact specimens. One exception in this data was found in a 2-

impact set where a much higher than expected permanent strain was measured. This can be attributed to the weaker boundary clamping that was in place during this test. The test was not repeated as it is important to note how the boundary affects the impact behavior of the specimens.

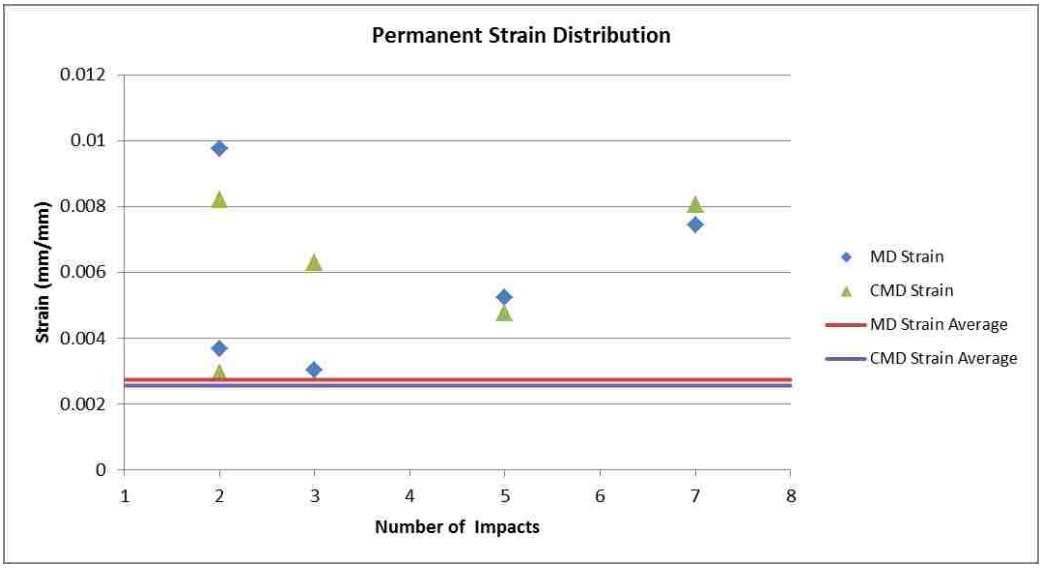

Figure 4-19 - Permanent Strain Distribution for Multi Impact Samples

4.6.1 Comparison Issues

The polymers used in these tests were both characterized by a hyperelastic material model, which will be discussed in greater detail in the next chapter. This material model selection provided unforeseen issues with the planned comparison methods, which are all based on linear elastic analysis with fairly simplistic methodologies in which to obtain the stiffness matrices required to solve the energy balance equation, as well as ease of computation for finite element analysis simulations. An additional element to keep in consideration is that in order to take

advantage of the increased flexibility inherit in the knitted reinforcement layer, an elastomeric material will need to be used. These flexible composites will result in deformations much larger than the thickness of the material, thereby no longer considered a linear deformation scenario.

Another interesting aspect of the impact event included the previously discussed rebound event. As seen in Figure 4-9, the test specimens provide an acceleration upward immediately following the maximum deflection, which is not a common element found in the literature. This results in the established energy balance prediction methods discussed in 2.2.3 to be inapplicable in the current situation. Without further instrumentation in the impact testing rig, many of the necessary data points are difficult to find, such as the recoverable strain energy. This could be accomplished by analyzing a force vs. displacement curve where it would be expected that a closed curve would be observed based on the calculated difference between max deflection and the much lower permanent deformation. Issues such as additional sensors and instrumentation would greatly increase the cost of the study performed and were subsequently not available.

4.7 Discussion and Conclusion

As seen in the results and post impact analysis, the elastomeric polymer materials combined with knitted fiber reinforcement returned nearly 25% of the incident energy back into the system. In order to verify the scalability of these experiments, much larger scale tests should be performed in order to assess at which point, if any,

the amount of energy fully absorbed by the test panels reaches a level that can be satisfactory. It can assumed that this point would correspond to a level at which nearly all of the incident impact energy is removed from the system, thereby slowing the impactor down with minimal energy returned to the impactor. This would be a beneficial application in transportation barriers where sudden and violent decelerations can result in serious injuries. In further examination of the elastic properties, it was found that the elastic return capability of Arkema's Pebax® material was quite high as observed on their websites material properties section. This behavior can be seen in Figure 4-21 and Figure 4-21 through different testing methods.

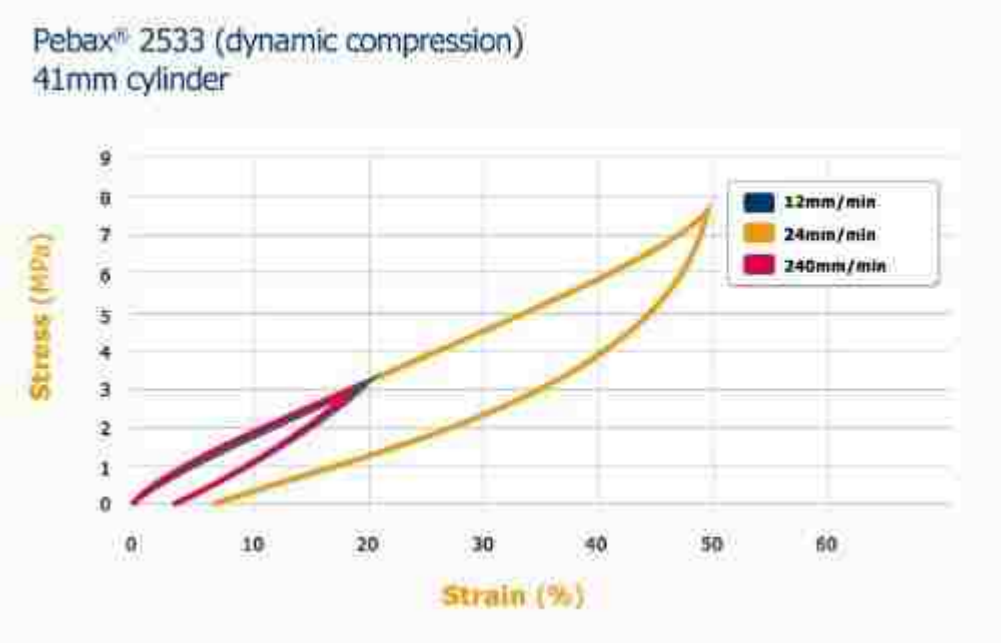

Figure 4-20 - Dynamic Compression Cycle [63]

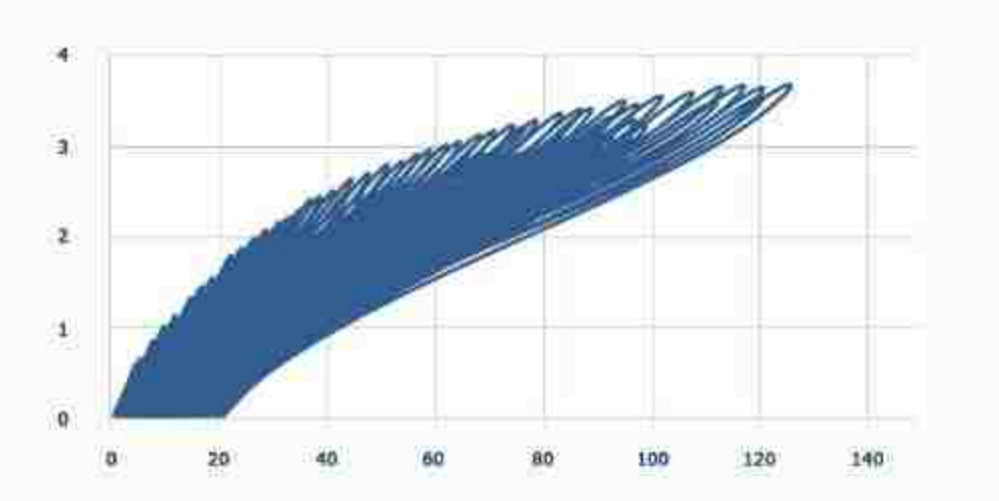

Figure 4-21 - Tensile Cycling Stress Given in MPa [63]

It can be concluded from these examinations that in order to absorb enough energy to result in large permanent strain values, very large initial strain values need to be introduced into the system. This will also allow for increased damage mechanisms into the fibers/yarns, thereby absorbing even more energy. In this sense, much higher energy levels at larger scales must be used to fully verify the energy absorbing capabilities of these knitted reinforced polymer materials. It is important to note that these tests be carried out with the same manner as the current experiments, i.e. low-velocity impact where multiple fibers/yarns are located within the contact area. By dramatically increasing the mass of the impactor, the desired increases in impact energy can be achieved.

5 Model Application - GAF Project

One application of non-woven polymer composites that was studied in-depth was that of a specific polymer composite building material. Several studies [63–65] examined the performance and testing of single ply membrane roofing materials which have gradually replaced more traditional built up roofing systems. These single ply systems do not offer any redundancy so their performance in terms of insulation and water-proof capabilities can be compromised by simple failures such as damage due to impact from tools used during installation. Due to the high flexibility of the systems, dynamic loading magnification could occur when fluctuating wind speeds create uplift loading on the roofing surfaces.

Figure 5-1 - Image of Roof Damage Caused by Hurricane
(Image from John F. Kennedy Space Center Damage Evaluations)

Because even the smallest failure can have drastic consequences, it is important to keep in mind that the overall performance of the roofing systems does not

depend solely on the physical properties of the materials used, but rather the installation methods, total system design and other factors that all play very important roles.

Prevatt, *et al.* [64] briefly discuss the two different installation techniques that are commonly used for the single ply membrane roofing systems. The first, which is not examined in the study, is a fully adhered system where the membrane is glued to the substrate insulation. No additional fastening mechanisms are used other than the adhesive. The second method is a mechanically attached system that employs fastener plates that are affixed to the structural roofing deck via screws. This schematic can be seen below in Figure 5-2. As mentioned above, the uplift or billowing loading that occurs from wind blowing over the surface of the roofing material and thereby creating a pressure differential similar to an airplane's wing is one of the largest concerns. The study goes on to point out a glaring difference in the manner in which the roofing systems are tested in North America versus Europe. While the European nations have employed dynamic testing protocols, static testing has remained the norm in North America even though a dynamic uplift standard was developed by the National Research Council in Canada in 2004. Another issue with testing discrepancies is the test specimen size which was also addressed by the same Canadian Standards Association study through the introduction of size correction factors. Even with all the aforementioned protocols in place, it still may be difficult to predict all failure scenarios.

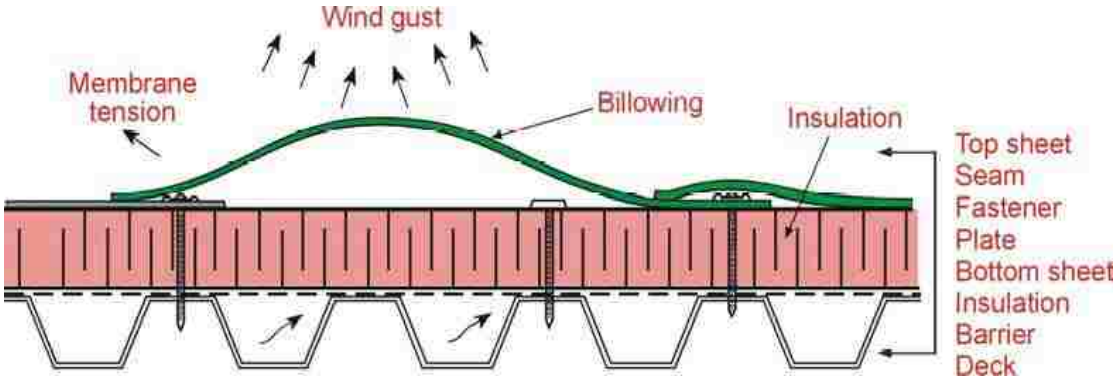

Figure 5-2 - Schematic of Roofing Material Showing Billowing Effect

Taylor and Yang [63] mention a very important business strategy that has applied to many single-ply roofing systems: Companies typically concentrate their efforts on cost reduction and manufacturing efficiency instead of making significant improvements of their more mature products. Despite this statement, GAF, a roofing solutions company, needed their commercial roofing product analyzed in order to find room for improvements. More specifically, the company's EverGuard® TPO (thermoplastic olefin) was the product of interest. The material consisted of two layers of TPO co-extruded onto a non-woven sheet of PET (polyethylene terephthalate) fibers. This material comes in 3.05m (10ft) wide rolls in varying thicknesses (45, 60 & 80mil) that are laid on top of insulation and fastened to the roof deck of the structure with screws and large washer type plates. When the layers overlap, a heat sealing roller is used to create a heat weld between the composite membranes. The wind uplift scenario discussed above results in a variety of failures,

including de-bonding at the heat seal seem, fastener pullouts, and tearing of the TPO sheets near the fasteners. The ultimate goal of the project was then established as creating a finite element model in ANSYS that would accurately depict the given scenario.

In order to evaluate and quantify the wind-uplift performance in the real world, experiments are performed in accordance with ANSI FM 4474, which states that a 3.7m x 7.3m (12ft x 24ft) platform be covered by a roofing system, including heat welded seams and mechanical fasteners. All four edges are then clamped to the platform and the volume between the membranes and the test platform is inflated incrementally every 0.72kPa (15psf) until a failure occurs. The current standard for the commercial roofing material is 5.745kPa (120psf). These parameters will be used in order to recreate the experimental results.

5.1 Micro-Scale Model

As discussed earlier in Section 1.3.4, a common approach to modeling a knitted composite is through unit cell analysis. With this in mind, an effort to create a finite element model was undertaken in order to accurately model the FM wind-uplift test. The results and methodology for the creation of this model can also be found in [66] which is waiting to be published at the time of this work.

5.1.1 Cell Geometry

The scrim, which is produced by Highland Industries, Inc., is comprised of PET fibers that are held together in a non-woven sheet. The fibers can be separated into 3 different types: horizontal fibers (in-line with the direction of machine production), vertical fibers (perpendicular to machine direction), and the "tie" fibers. The horizontal and vertical fibers lay in such a way that they create a grid, while the tie fibers are much smaller than the other two types and create joints where the other two fibers intersect.

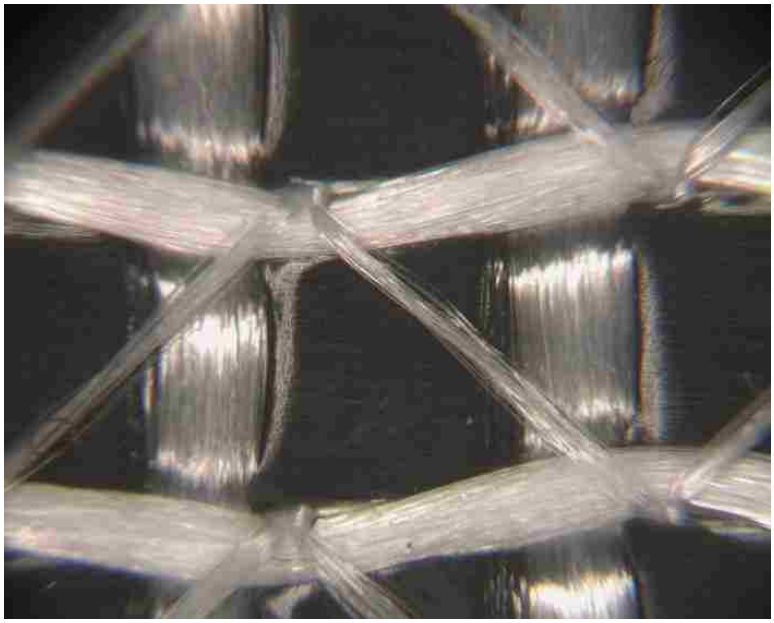

Figure 5-3 - Microscope Image of GAF Scrim

A first attempt to examine this geometry failed because the product used was the raw scrim, meaning it had not been adhered to any polymer yet. The material was very unstable and as such the images that were obtained were highly dependent on how the sample laid on the microscope platform. Any change in tension led to large

variations in the measurements. Because these discrepancies would not be helpful in creating the finite element model, a one sided polymer/scrim sheet was produced by the GAF Research Lab. This sample simply did not have the second sheet of polymer extruded onto it, so the geometry was exposed, yet was held firmly in place. Images were taken from several locations around the sheet in order to get an accurate depiction of changes within the sheet.

Measurements were taken of the apparent thickness of the fibers, the spacing between the fibers, and the angles that were made with the slight bending trend in the horizontal fibers as well as the angles created by the thinner tie fibers. The standard deviations on these values turned out to be fairly high for some of the measurements. After this was realized, the images and measurements were repeated for full production quality materials. These proved to be more consistent throughout the sheets as well as slightly different dimensions than those found in the samples produced by the research lab. The comparisons and results can be found below in Table 2.

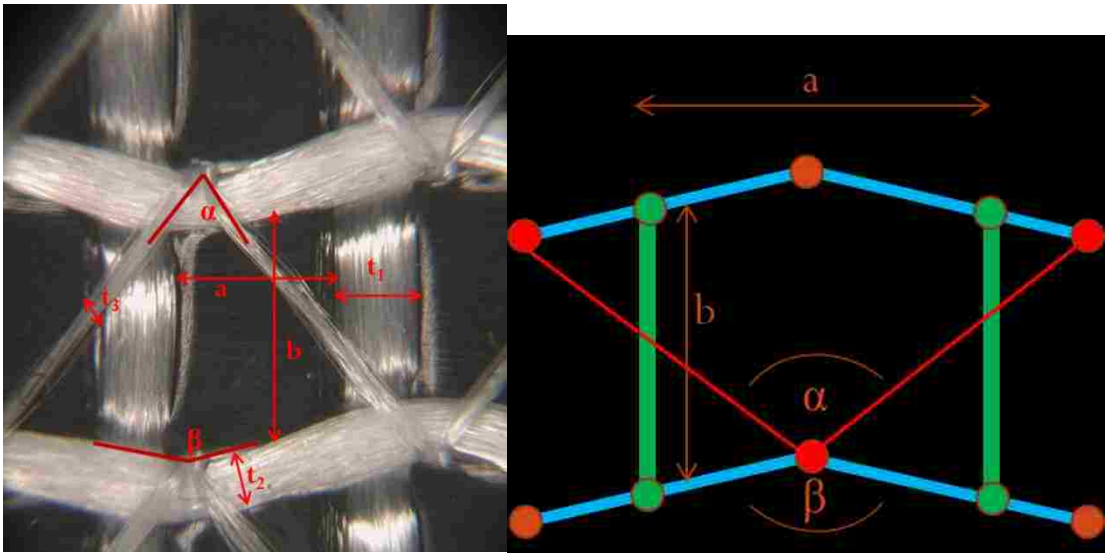

Figure 5-4 - Measurements Taken on Images (Left), Basic Cell Geometry (Right)

Table 2 - Comparison of Measurements

	Lab Created		**Manufactured**	
	Average	Std. Dev.	Average	Std. Dev.
a	2.042mm	9.68%	1.172mm	11.98%
b	2.105mm	5.10%	2.022mm	3.23%
t1	1.065mm	17.75%	1.169mm	9.80%
t2	0.662mm	12.04%	0.672mm	7.75%
t3	0.281mm	14.48%	0.237mm	9.98%
α	94.4°	2.23%	82.5°	2.29%
β	152.3°	1.34%	153.5°	2.30%

Since the manufactured material will be used in the commercial applications, the corresponding measurements were used to create the initial cell geometry and spacing. Within ANSYS, it is very simple to create a single cell and replicate it into a matrix of cells that will correspond to and entire sheet. Once this geometry was created satisfactorily, the next step was to gather the material properties for both the fibers as well as the polymer.

5.1.2 Material Properties

Tensile tests were performed on an Instron Universal testing machine with Measurements Technology Inc. MTI-10K integrated into it. For the first round of testing, samples of the bottom and top TPO sheets were cut into 18.5mm x 80mm (0.728in x 3.15in) pieces at varying orientations, according to the designations seen below in Figure 5-5.

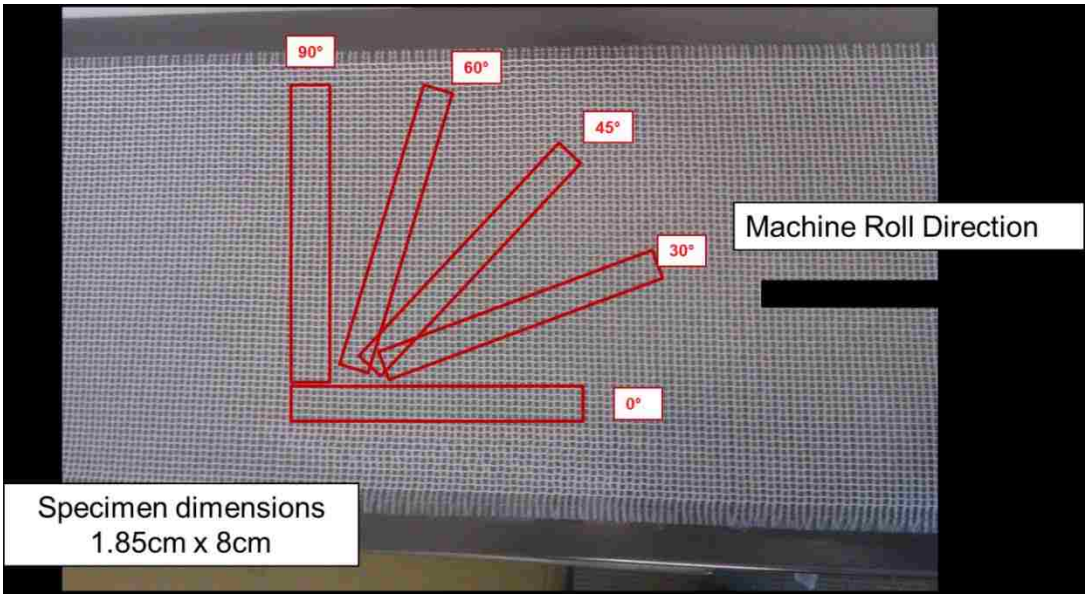

Figure 5-5 - Tensile Specimen Orientations

The majority of the tests were run at 10mm/min (0.394in/min) crosshead speed, but a study for the effect that strain rate had on the material was also performed, which will be discussed below. Several polymer samples were tested and the results can be seen in Figure 5-6 and Figure 5-7. The black TPO is designated as the bottom side of the EverGuard® material while the white TPO is used for the top layer. The layers differ as additives are included in the creation of the black TPO which produces slightly different results.

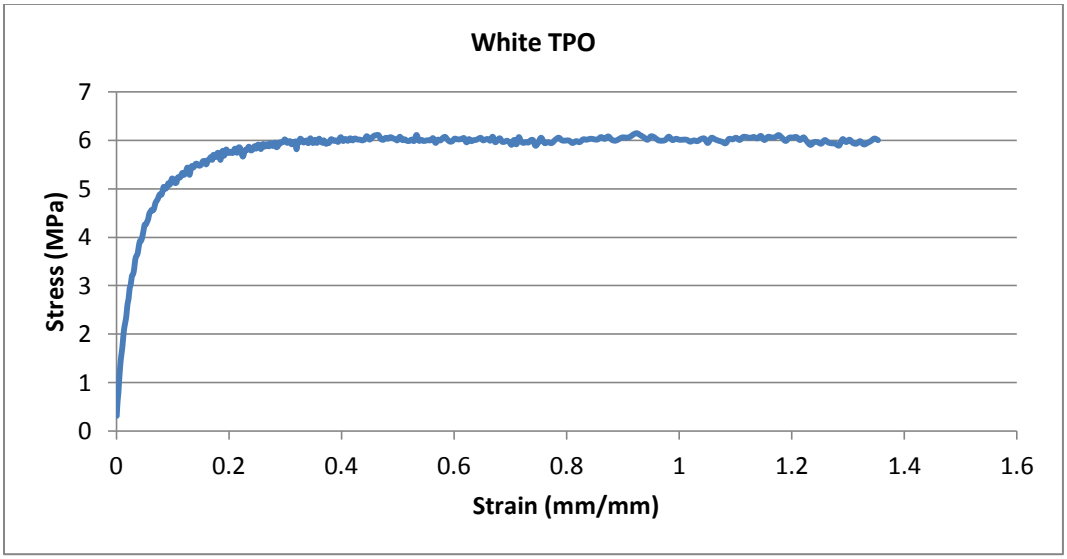

Figure 5-6 - Stress vs. Strain Curves for White TPO for 18.5mm x 80mm Samples

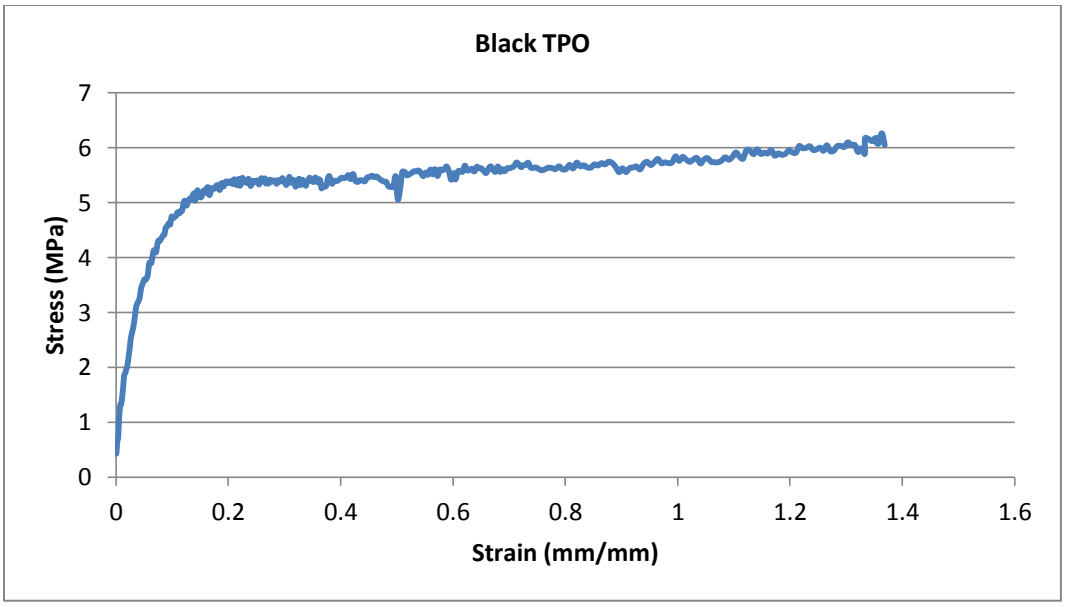

Figure 5-7 - Stress vs. Strain Curves for Black TPO for 18.5mm x 80mm Samples

Figure 5-6 and Figure 5-7 show the results of the tensile tests for the white TPO and black TPO, respectively, which were found to behave nearly isotropically, which is consistent with results found in [63]. On the other hand, the values from these tests differed from the expected results so larger samples were cut along the same orientation patterns, but with the same aspect ratio. The main factors attributed to this discrepancy included the small samples' vulnerability to environmental noise as well as the lower overall stability. The larger sample sizes produced much more consistent results and were more in-line with the manufactured expectations.

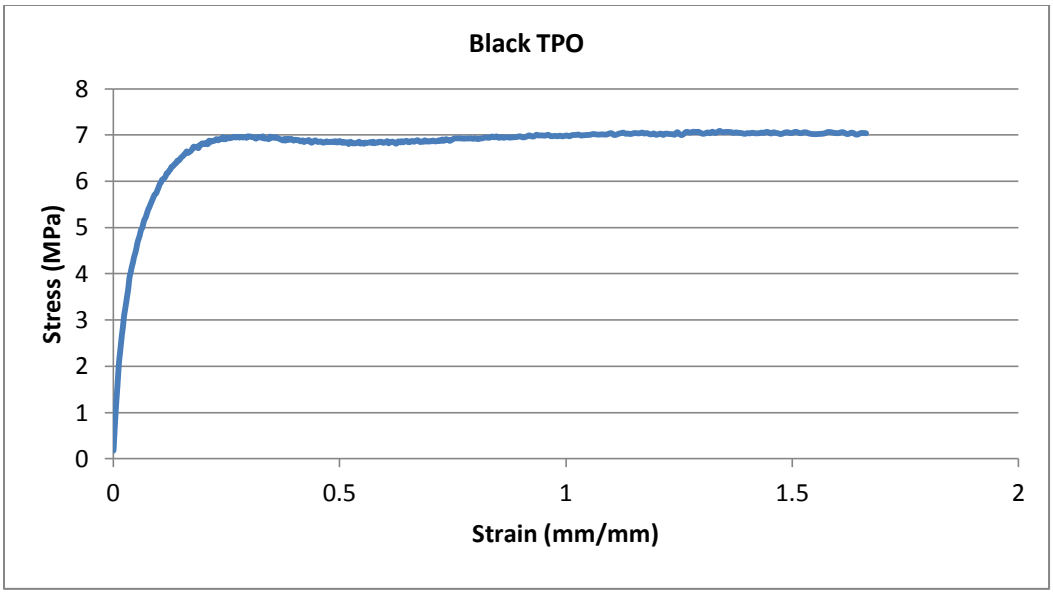

Figure 5-8 - Stress vs. Strain Curves for Black TPO for 25mm x 108mm Samples

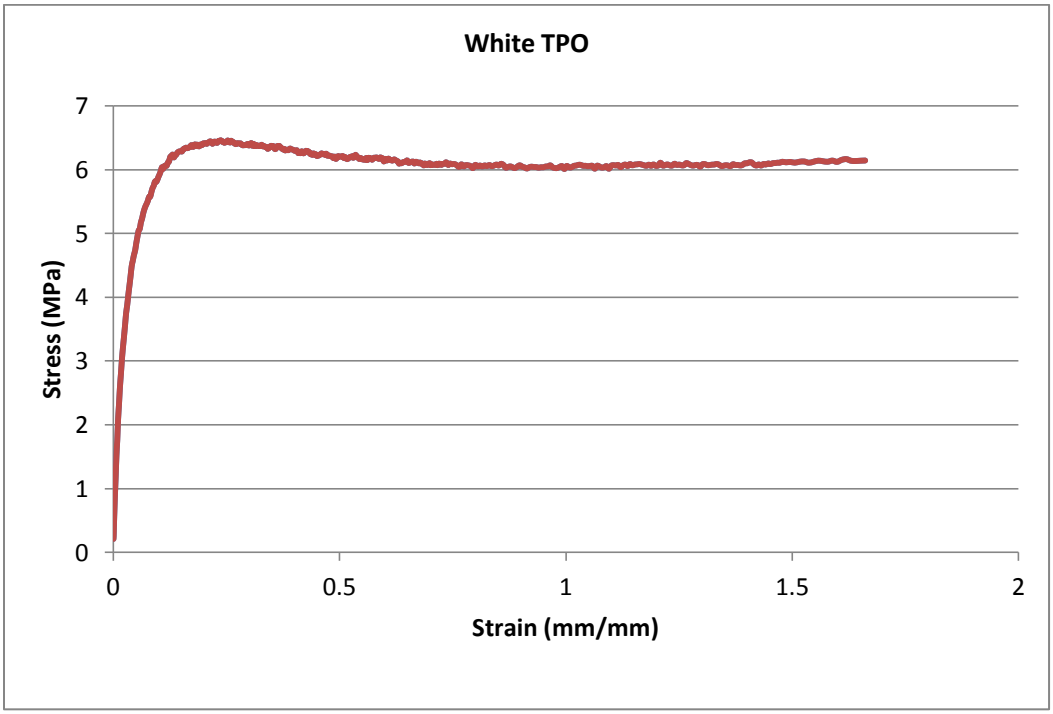

Figure 5-9 - Stress vs. Strain Curves for White TPO for 25mm x 108mm Samples

With these test results, ANSYS's curve fit tools were employed in order to define the material within the model. Examination of the stress vs. strain curves reveals that the material behaves in a non-linear, elastic manner. This type of behavior fits into the realm of a hyper-elastic material since the polymer also displays isotropic behavior, as mentioned earlier. In general, hyper-elastic material models do not incorporate strain rate effects. To examine this assumption, the tensile tests were repeated for varying strain rates between 2mm/min and 50mm/min. The results for these tests matched very closely with the initial set of results that were performed at 10mm/min. Knowing that we were dealing with very large deformations, the best solutions for the material model for these flexible polymers is either Ogden or Mooney-Rivlin models [67–69]. The Mooney-Rivlin model is based on the strain-energy function as is expanded into an infinite series:

$$\boldsymbol{W = \sum_{m,n=0}^{\infty} C_{mn}(\bar{I}_1 - 3)^m(\bar{I}_2 - 3)^n \qquad (C_{00} = 0)}$$

E. 5.1

Where *W*, is strain energy, C_{mn}'s are the constants, and $\bar{I}_1$ and $\bar{I}_2$ are the 1st and 2nd invariants of the unimodular component of the left Cauchy-Green deformation tensor given as:

$$\boldsymbol{\bar{I}_1 = J^{-2/3} I_1; \qquad I_1 = \lambda_1^2 + \lambda_2^2 + \lambda_3^2\,; \qquad J = \det(F)}$$

E. 5.2

$$\boldsymbol{\bar{I}_2 = J^{-4/3} I_1; \qquad I_2 = \lambda_1^2\lambda_2^2 + \lambda_2^2\lambda_3^2 + \lambda_3^2\lambda_1^2}$$

E. 5.3

Where λ_i are the principle stretches, seen below in Figure 5-10, and F is the deformation gradient.

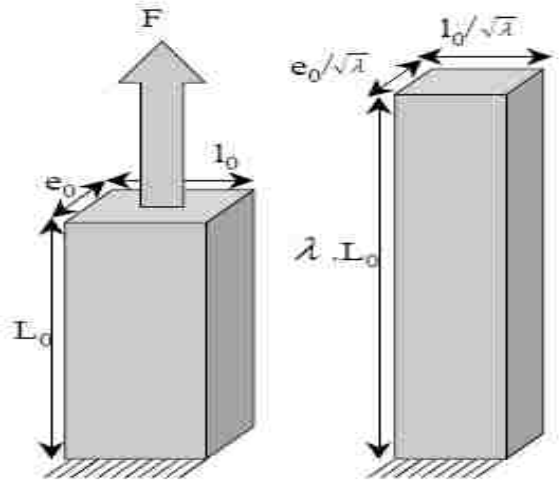

Figure 5-10 - Principle Stretches

This function is built into ANSYS for ease of computation and only requires a text file containing the stress vs. strain values obtained experimentally. Solving for the constants represented by C_{mn} is a simple step that will also produce plots showing the curve fit match. ANSYS has built in solvers for *m* & *n,* values up to 3, which yields a total of 9 parameters. The results of these solutions can be seen below in Figure 5-11.

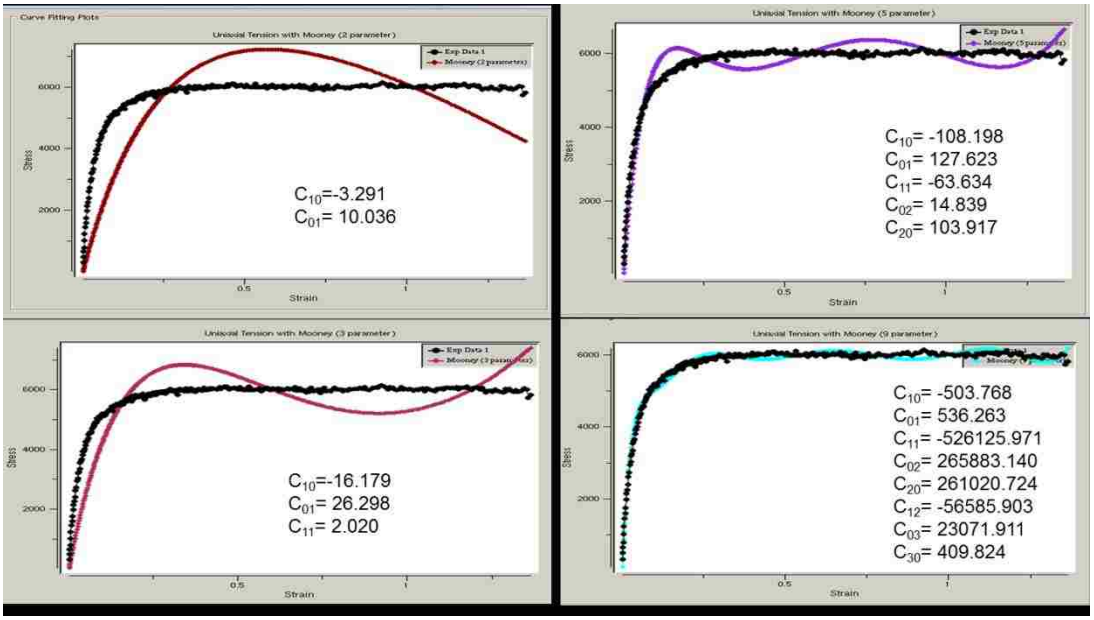

Figure 5-11 - Examples of White TPO Mooney-Rivlin Curve Fitting

Clockwise from Top Left: 2 parameter, 5 parameter, 9 parameter, 3 parameter

It can be seen above that the 9 parameter Mooney-Rivlin curve fit produces a fairly close match. Unfortunately, the more parameters that are used in defining the material behavior, the more computationally intensive the program becomes. The other option available, as mentioned above, is the Ogden model. Again, this model is based on the strain energy of the material but this time with fewer constants. The Ogden model for an incompressible material is given by:

$$W = \sum_{p=1}^{N} \frac{\mu_p}{\alpha_p}\left(\lambda_1^{\alpha_p} + \lambda_1^{\alpha_p} + \lambda_1^{\alpha_p} - 3\right)$$

E. 5.4

Where again λ_i corresponds to the principal stretches mentioned above, and α_p and μ_p are the material constants that will be found through curve fitting. An example of this curve fitting can be seen below in Figure 5-12.

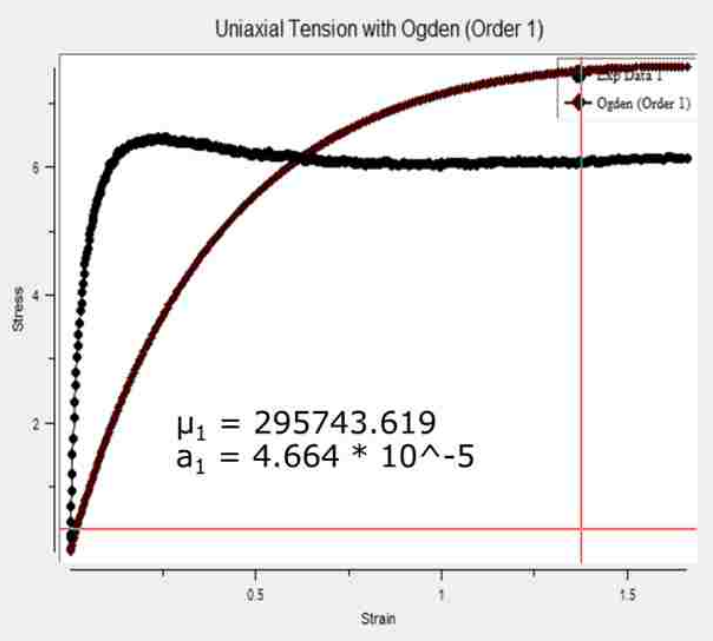

Figure 5-12 - Example of White TPO Ogden Curve Fitting

From Figure 5-12 it is easy to see that the Ogden model will be able to predict very large deformations with fewer parameters, which leads to greater stability in the model solution.

In order to better understand the entire composite system, the focus was turned back to the Instron testing machine to examine the uniaxial behavior of full composite samples. Test samples were cut in the same manner as seen in previously in Figure 5-5. The tests produced very interesting results as the composite behaved

very differently along the directions of the main fiber orientations, while it behaved more similarly to the polymer by itself when the off-axis samples were tested.

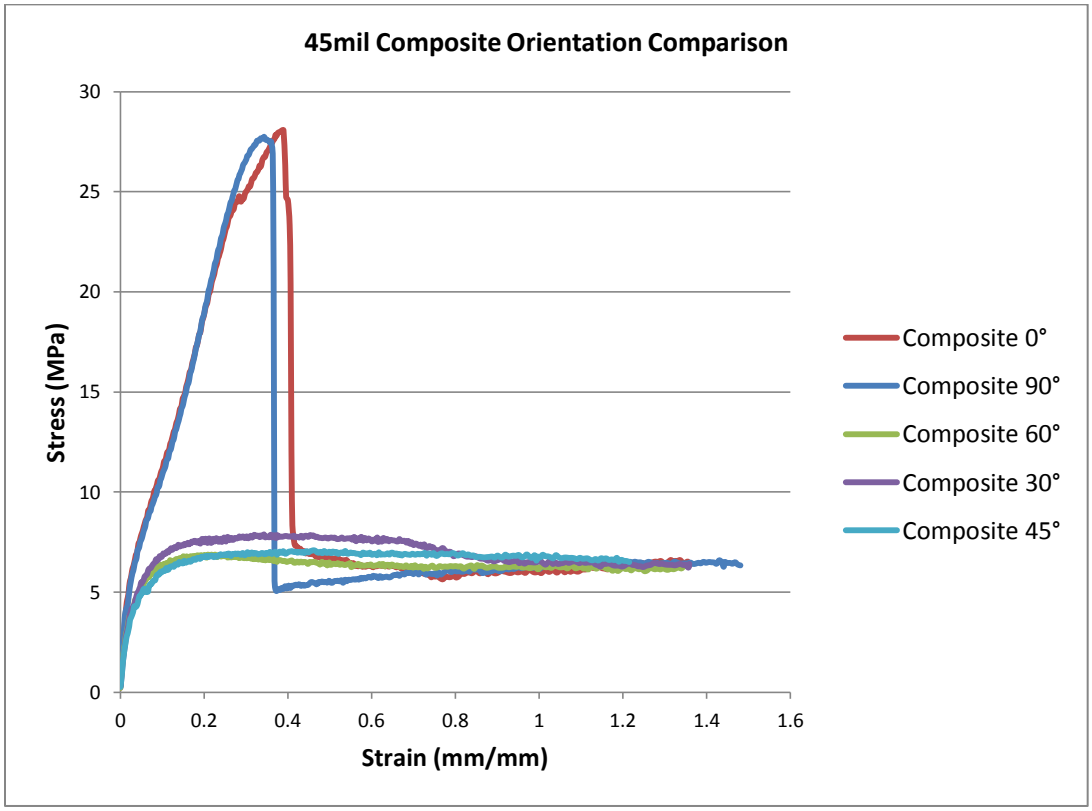

Figure 5-13 – 45mil Composite Orientation Comparison Stress vs. Strain Curve

As seen in Figure 5-13, the fibers failed in the ~35% strain range, where the curve suddenly dropped to the level of the off-axis composites. By confirming with previous experimental results seen by GAF, and attempting to find the best curve fit, a final deflection limit of 30% was decided upon. By trimming the stress strain curves of the polymer to around 30% strain, the elongated portion of the curve, which proved to be the most difficult to accurately match, could be eliminated. This

allowed the number of necessary parameters to diminish to a more manageable level for the simulation, and lead to the elimination of the Ogden model as a feasible solution. A 5 parameter Mooney-Rivlin model produced a close match for the stress-strain curve while also providing increased stability in the solution of the model. A simple replication of the uniaxial tensile test produced the curve seen below in Figure 5-14. With good agreement for the polymer, the attention could be turned towards the fibers as well as the full composite.

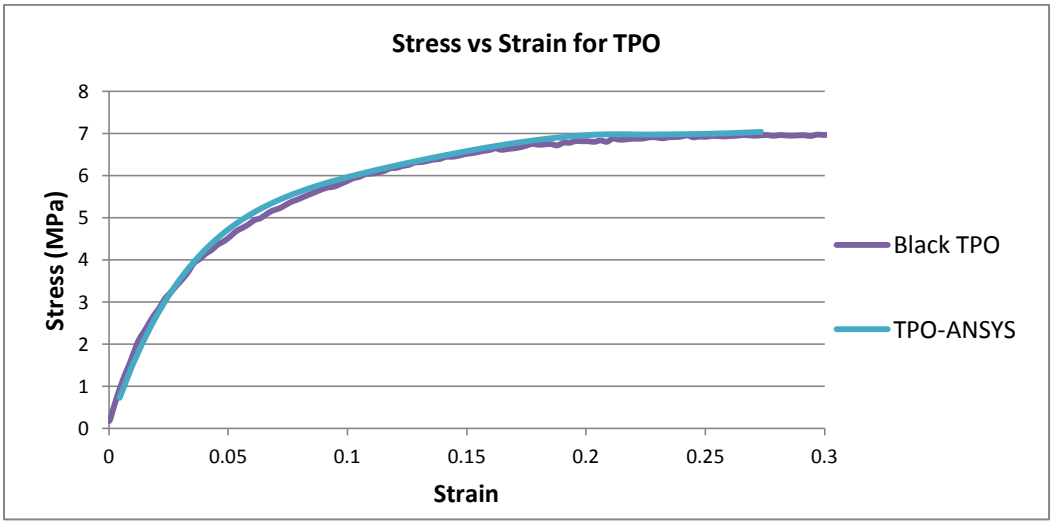

Figure 5-14 - Comparison of Black TPO to ANSYS Simulation

The size of the samples limited the number of continuous fibers imbedded in the composite to around 5 or 6, since the specified fiber ends per inch was 9±1. This number is important as the combination of materials continues. A force vs. displacement curve from Highland Industries Inc. was provided for reference since the testing of individual fibers or even groups of fibers proved near impossible due to the inconsistency of the gripping techniques available and the instability of the

raw material. From the data provided, the force vs. displacement curves of the fiber in addition to those of the polymers was actually much higher than that of the full composite. This was only discovered after several attempts of correcting an issue within the ANSYS model, which will be discussed in greater detail below.

The full composites are created by co-extruding the polymers onto the PPT scrim in order to create the sandwich sheets that are the final products. Because of this method, it is very easy to produce one-sided material where only one sheet of polymer is adhered to the PPT scrim, leaving the fibers exposed to view. As mentioned earlier, this is how the geometry was examined and measured for the cell structures. The other benefit of the one-sided structures was to examine their tensile behavior, which can be seen below in Figure 5-15 and Figure 5-16.

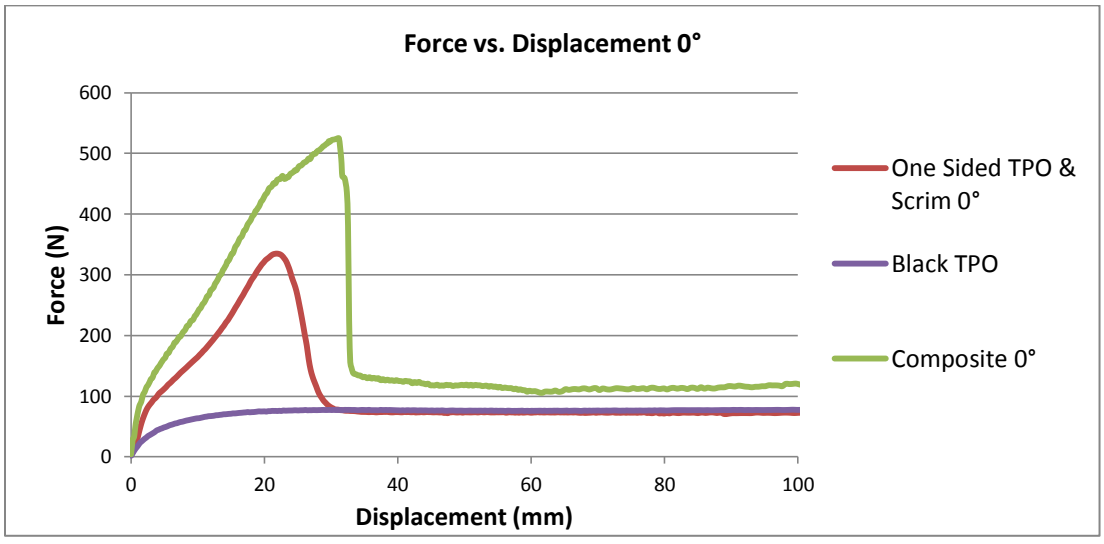

Figure 5-15 - Force vs. Displacement for 0° Orientation

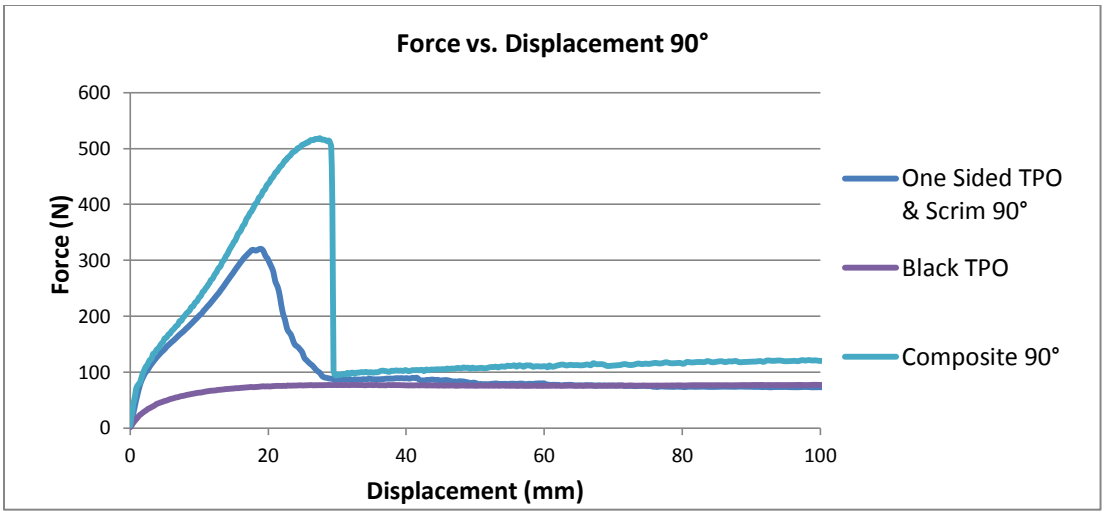

Figure 5-16 - Force vs. Displacement for 90° orientation

These one-sided structures follow along with the earlier observations seen in the full composites that when the fibers begin to fail the overall strength of the material falls back to that of the TPO by itself. With this observation, the polymer behavior can be removed from the one-sided behavior, in order to obtain the "effective" fiber force vs. displacement curve. The exact reason why the effective and provided curves differ is unknown, but one theory is the constraints provided by the adherence between the polymer and the fiber. As will be mentioned again below, the data extracted through this manner did work once the additional sheet of polymer was added into the model. In order to obtain more robust data for the fibers, a simulation using the two sheets of the TPO with the fiber values set to negligible levels was examined. This behavior was then subtracted from the behavior of the full composite in order to extract the final force vs. displacement

curve which can be seen below in Figure 5-17. This final piece of data completes the basics necessary to move forward with modeling.

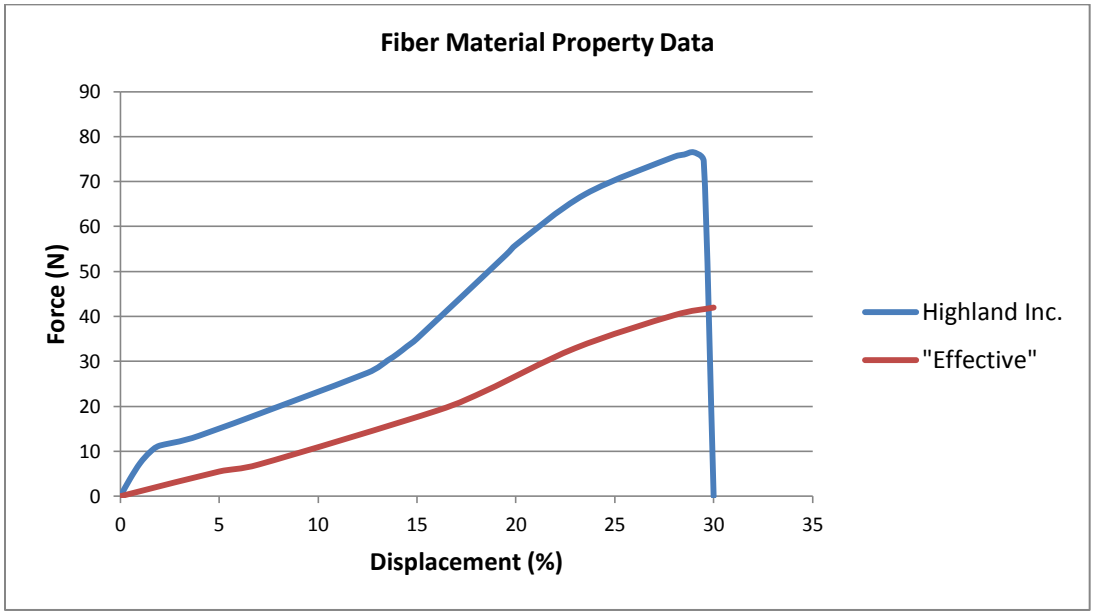

Figure 5-17 - Force vs. Displacement Comparison

5.2 Finite Element Modeling

Once the cell geometry was established and the material properties were obtained, the full model could start to come to fruition. The polymer elements would be modeled using SHELL181 elements in order to allow the thickness to be varied by merely changing the real constant that defined the thickness of the elements. These elements would also take on the 5 parameter Mooney-Rivlin material model that was discussed previously. The cell geometry and subsequent definition of the fiber material properties was the next challenge. The spacing and

apparent fiber thicknesses obtained above were both analyzed in order to create a chevron type element as seen previously. Upon further examination, the tie threads, represented by the very thin diagonal elements seen in Figure 5-4, did not seem to carry any additional load and appeared to only serve as support to hold the main yarns in place during the manufacturing process. Due to these observations, these fibers were left out of the initial model for simplicity purposes and the only load bearing fibers were kept in the Machine Direction (MD) and the Cross Machine Direction (CMD). These designations are defined based on the direction in which the rolls of single-ply membranes are manufactured, where Machine Direction is parallel with the direction in which the rolls are produced and Cross Machine Direction is defined as perpendicular to this production direction. Once a single cell was created, it could be replicated in order to create a matrix of cells that would be representative of the overall fiber structure the scrim. This pattern can be seen below in Figure 5-18.

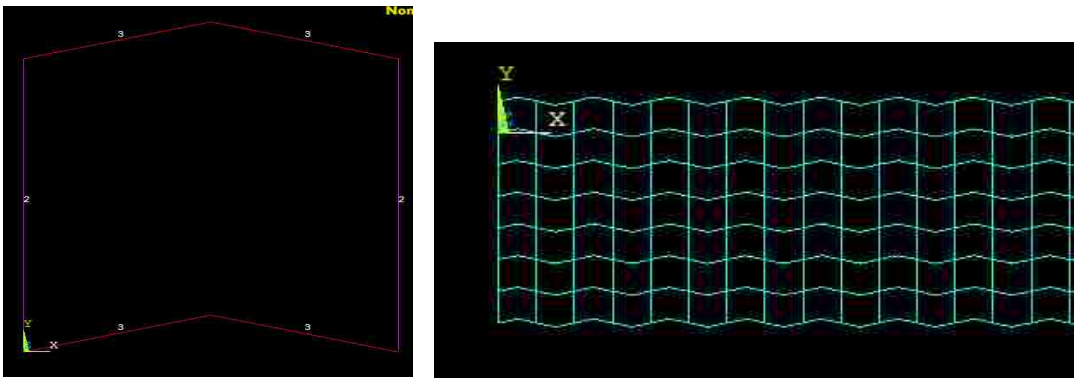

Figure 5-18 - Single Cell Geometry (Left) Pattern Created from Repetition (Right)

Because these fibers cannot carry any load in compression, a non-linear spring element (COMBIN39) was used for modeling purposes. These elements would take on the properties of the fiber's effective force vs. displacement curve data that was acquired by the method mentioned above. The reason that this specific type of element was used was in order to accurately depict the behavior of the fiber was that by employing the correct key options, the fibers would only be able to carry load in tension, and not in compression. This is important since the yarns used to create the scrim behave in the same manner. After the fibers were created, the polymer elements were then created using the same key points and nodes that the fibers used. This helped to create a situation corresponding to perfect adhesion and bonding so that the fibers and polymer sheets moved together. This proved to be the most expedient method of creating the model, but could later be changed in order to examine the effects of less than perfect bonding. Due to instability of employing quadrilateral shaped elements in the tension analysis, triangular units were used to fill the void left by the fibers.

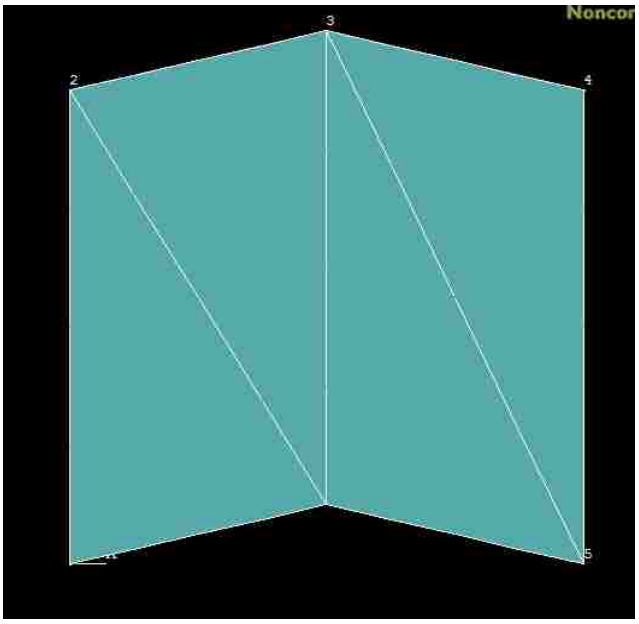

Figure 5-19 - Cell Geometry with Polymer Elements Added

For the uniaxial tensile test analyses the boundary conditions were set such that one side was clamped while the opposite end was moved through displacement driven analysis. By extracting the reaction forces at the nodes that were clamped, the force vs. displacement and stress vs. strain curves could be created in order to compare them to the experimental results.

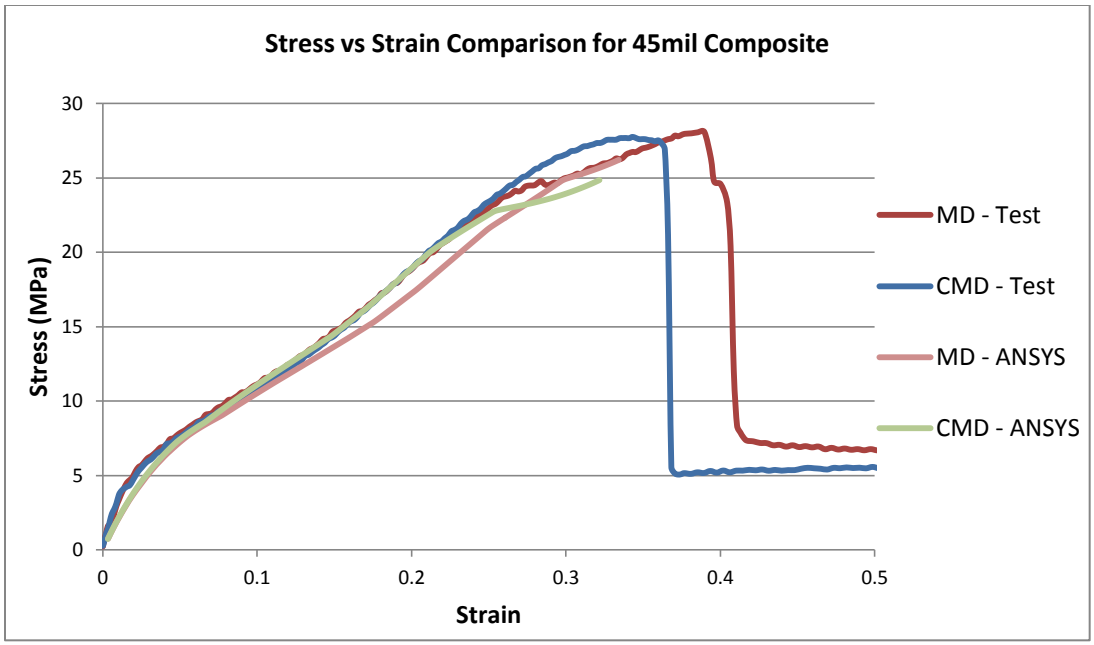

Figure 5-20 - Stress vs. Strain Comparison for 45mil MD and CMD Cut Tensile Specimens and Finite Element Results

Once satisfactory results were achieved in the simple uniaxial tensile test, the attention was turned to larger scale models in order to check for the consistency and capabilities of the model. At this point, it was found that the size of the model was limited to around 152mm x 254mm (6in x 10in) due to the large number of elements included in such simulations. This discovery was not unexpected as previous studies have pointed out the computational effort required to model individual loops in a knit pattern [23,29].

5.3 Macro-Scale Model

A new model would be created in order to preserve the good agreement found in the micro-scale model, but would allow for larger scale models to be created in

order to mimic the FM wind uplift tests which required a 26.8m^2 (288ft^2) area of the roofing system. To accomplish this, a SHELL181 element with section properties was created. Each element was given section properties that corresponded to the individual constituents of the composite. In the micro-scale model, the fiber architecture allowed for the anisotropic behavior of the composite to come through in the finite element simulations, but in the macro-scale model, the individual fibers will no longer be present, rather a layer that possesses the stress/strain relationship exhibited by an area of fabric. This relationship was based on the specifications provided by the scrim manufacturer, including the number of yarns/mm (yarns/in) and the force-displacement curve data provided for each yarn. Based on these values, a simple stress/strain plot was created and an additional curve fit model was employed in order to obtain a good match. However, with this model, the anisotropic behavior was not accounted for. In order to take this into consideration an additional layer with orthotropic properties in the Cross Machine Direction only was added to the element.

Figure 5-21 - Schematic of Section SHELL181 Element

An attempt was made to combine the micro- and macro-scale models in order to achieve a balance between detail in specific areas and the ability to create models

with dimensions more indicative of the scaling associated with roofing systems. This was not a successful endeavor as an unknown discontinuity between the two models resulted in extremely high reaction forces as compared to either model alone, as well as the experimental results. This version of the model was scrapped in favor of the macro-scale sectioned shell elements only.

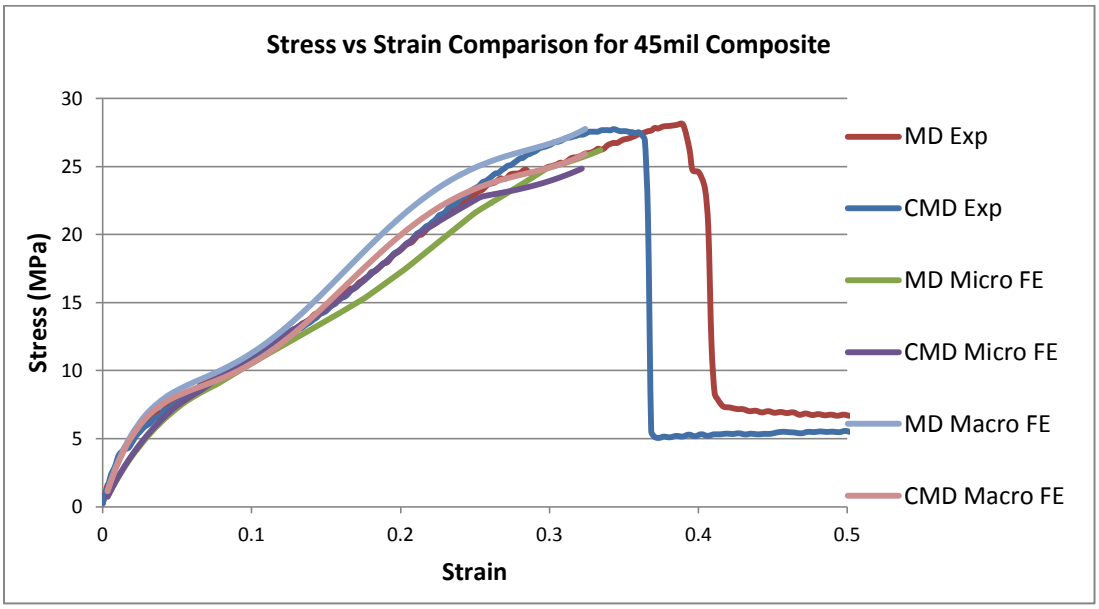

Figure 5-22 - Stress vs. Strain Comparison for 45mil MD and CMD Cut Tensile Specimens and Micro- and Macro-scale Simulations

As seen in Figure 5-22, the macro-scale model provided a good match to the micro-scale model, as well as to the experimental results. These results were deemed sufficient enough to move forward with the increasingly complex model that would be required to accurately model all of the aspects of the roofing system, including the heat welded seam, steel plate fasteners, and varying boundary conditions that would all highly impact the simulation results and stability.

5.4 Roofing System Model

With the material properties clearly defined, the attention could then be turned towards the remaining items that needed to be included in the full roofing system model. As previous results have shown, the TPO membrane does not fail during loading in the areas near the middle of the sheet, therefore the mechanically fastened areas and seams are the weak points of system, which require special attention during the modeling process. As seen below in Figure 5-23, the three main forces that are acting are the peeling force, which acts between subsequent sheets, the tearing force that occurs near the interface of the mechanical fasteners and the membranes, and the internal tensile force present in each sheet.

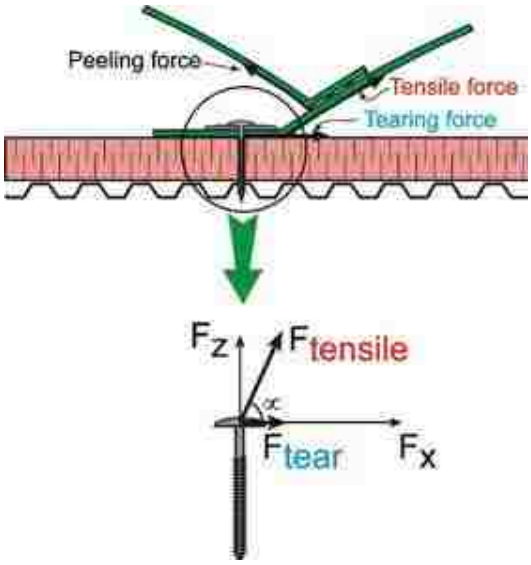

Figure 5-23 - Pull-Out Scenario Schematic

In the real life application, seams are created using a heated roller that melts the polymers enough to fuse them together. This will be the first portion of the roofing system added to the model. Since the direction of the "pealing force" as labeled in Figure 5-23, is unknown, there will be two different values used in defining this interaction: normal strength & shear strength. A previous study [63] and additional experimental tests have examined the strength values of these welds under different loading conditions. Two loading conditions, T-peel and shear seam, were examined and the results were used to define the properties used in the weld area.

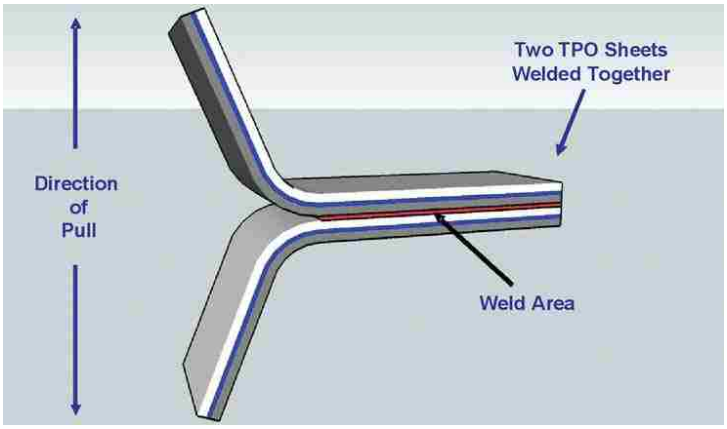

Figure 5-24 - Schematic of T-Peel Test [63]

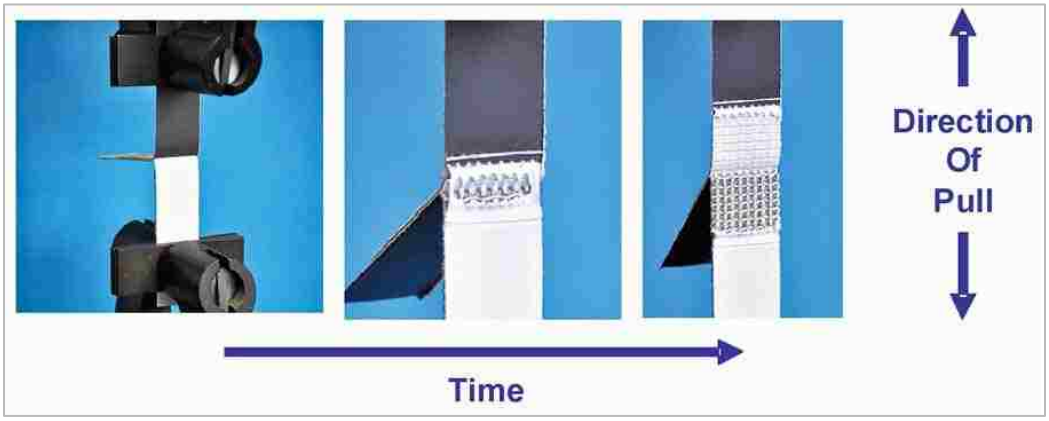

Figure 5-25 – T-Peel Test Progression [63]

The T-peel experimental setup that determines the normal strength of the welds can be seen in Figure 5-24 and Figure 5-25. As seen in Figure 5-25, the peal test results in a delamination of the composite, leaving the underlying fiber reinforcement exposed. This behavior resulted in a cyclic behavior of the load vs. peel extension plot (see Figure 5-26) as each subsequent boundary between the TPO and fiber was reached. The breakage points are used to determine the appropriate normal strength values of the weld.

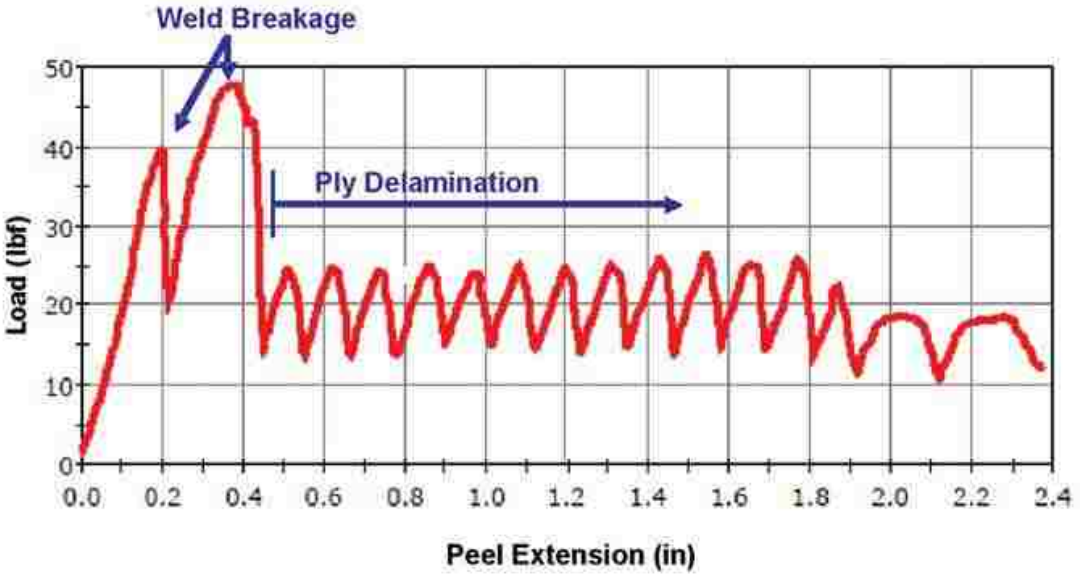

Figure 5-26 - Load vs. Peel Extension for Normal Peel Test [63]

Additional tests were performed in the shear direction as seen below in Figure 5-27. The study found that the shear direction failed near the ultimate strength of the polymer, thereby indicating that the shear strength of the weld was in fact higher than the strength of the polymer. To account for this scenario, the shear

strength will be set to a very high number, therefore relying on the material data of the polymer to determine the failure regions.

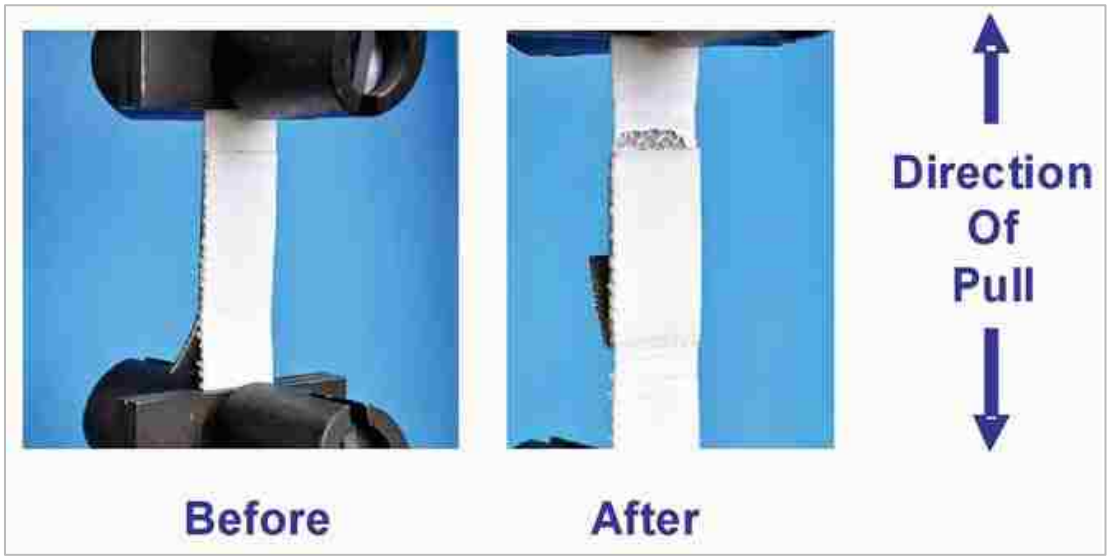

Figure 5-27 - Shear Loading of Seam [63]

In order to create this weld, two composite sheets overlapped in accordance with the installation specifications determined by the manufacturer. Within the overlapped area, CONTACT173 and TARGET170 elements were used in combination with Cohesive Zone Material (CZM) property values based on the seam strength data for the flexible-flexible contact analysis. This modeling condition could be used to examine any delamination that may occur. As mentioned previously, the area welded in the real world application does not actually fail, but rather the material just outside the CZM fails due to delamination between the top and bottom TPO sheets and the fiber scrim as well as failure of the TPO sheet itself as seen in Figure 5-27.

In order to check the suitability of this method, a simple double bubble inflation model was created with clamped edge boundary conditions. By examining the CZM zone for increased stress concentrations, as well as comparing the maximum out of plane deflection values to those observed in the real wind-uplift test, it was concluded that the weld area was sufficient enough to move forward with increasing the complexity of the model.

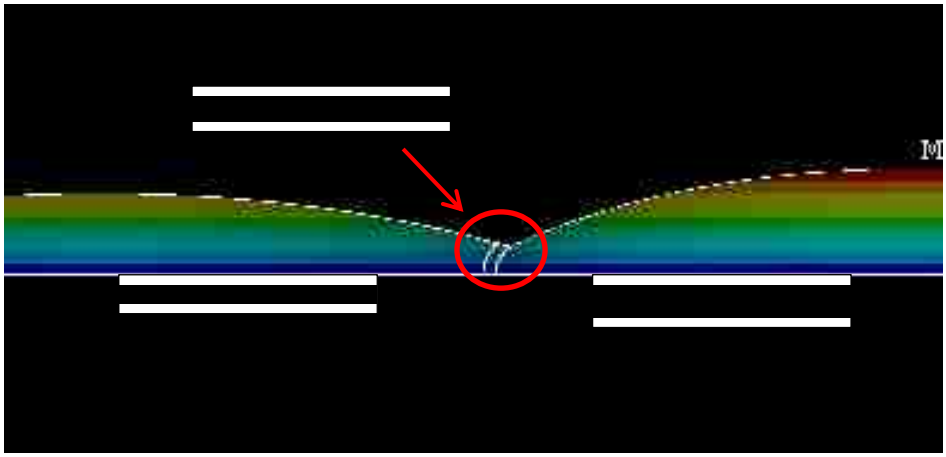

Figure 5-28 - FEA Simulation Delection Results Plot

To accompany the test data for the heat seam strength, data for the failure near the fasteners was also provided through mechanical testing. Figure 5-23 shows a simplistic representation of the tear scenario that occurs due to the wind-uplift loading in the roofing material, while Figure 5-29 shows the corresponding physical testing setup. Data provided by this experimental setup was used for failure analysis in the subsequent section.

Figure 5-29- Fastener Pull-Out Test

Contact between the plates that are secured to the roofing deck by fasteners is a difficult interaction to model. With several scenarios to consider, the details involved in contact analysis in ANSYS are complicated and vast. Since the main elements that will be in contact are shell elements created in essentially 2-D geometry, it is very important to distinguish between the top and bottom by

defining the normal vectors of each element in the appropriate direction. These directions determine which elements are considered the “target” elements and which are the “contact” elements. In most cases the more rigid object will be defined as the target while the more flexible material will deform around the target elements. Therefore in this contact scenario, we can see below in Figure 5-30 that the plates are circular barbed steel plates that are affixed to the steel deck below the composite and insulation blocks by the fasteners that go through all of the material, so the plates will be defined as the target, above the composite.

Figure 5-30 - Fasteners and Plates

Once these directions are established, many more possibilities must be explored. One of these options is to include friction between the materials. In the specific case of the composite pulling out from under the plates, the barbed teeth that protrude into the polymer can be initially modeled by an increased the level of friction. This interaction is a more complex one which results in the use of an unsymmetrical

solver in order to take into account the behavior of this sliding friction. The next option that can be adjusted is a defined initial penetration of the target elements into the contact elements. Since the initial position of the plate and composite are essentially parallel, no initial penetration will be defined. This could be adjusted however to take into account any over-tightening that could occur during installation. There are many more complex options available, but those discussed thus far will be sufficient to model the tearing force. Different spacing schemes of either 152.4mm (6in) or 304.8mm (12in) are used in accordance with readily available anchor points in the deck structure. This difference in the quantity and frequency of fasteners has a large impact on the wind-uplift performance due to the increased stress on the larger spaced fastener systems. Data provided for Drill-Tec™ steel fastener plates was used for shell elements in the model. Again, CONTACT173 and TARGET170 elements were used in order to perform the rigid-flexible contact analysis.

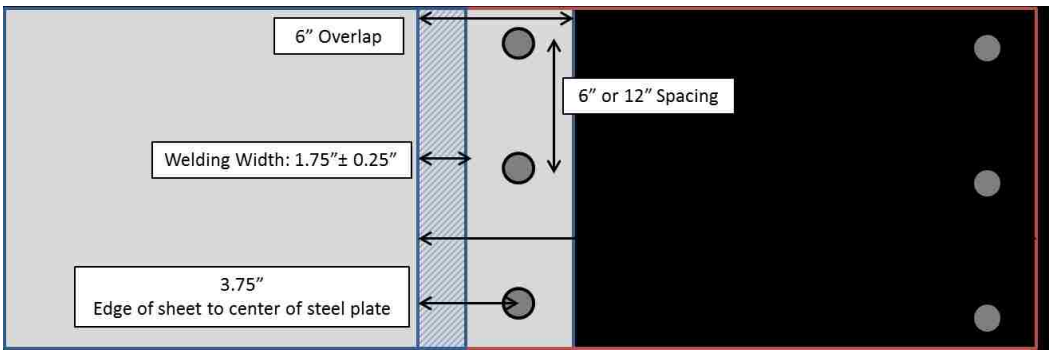

Figure 5-31 - Schematic of Roofing System Installation

In an effort to minimize the number of elements, while still achieving a high level of detail in regards to mesh refinement, a strip element was proposed that would examine a portion of the roofing system occupying an area defined by two 3.048m (10ft) long sheets and represent repeating symmetry for a vey large surface. The dimensions in the perpendicular directions would then be defined by the desired spacing, thereby spanning from center point of one fastener to the next. This geometry would then require symmetry boundary conditions on the two long edges and clamped conditions for the steel plates and remaining free edge.

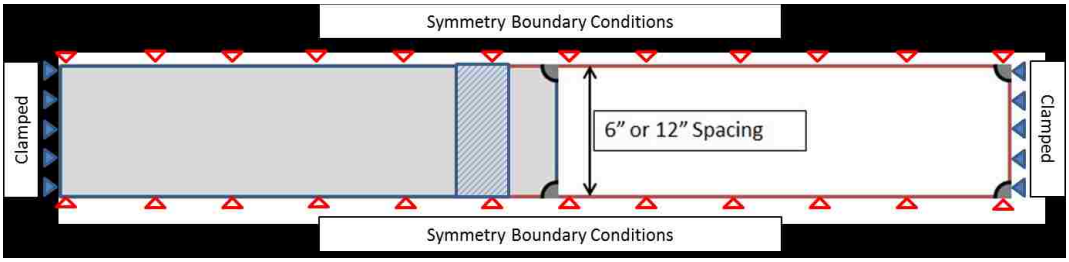

Figure 5-32 - Schematic for Finite Element Strip Model

The strip model was then surface loaded by incremental loading up through the previous pressure requirement of 4.31kPa (90psf) until the current required threshold of 5.75kPa (120psf) was reached. It was found that this geometry did not provide a good match between the simulation and FM wind-uplift tests due to the boundary conditions involved in the experimental tests, i.e., in small test samples the edge effects are relatively large.

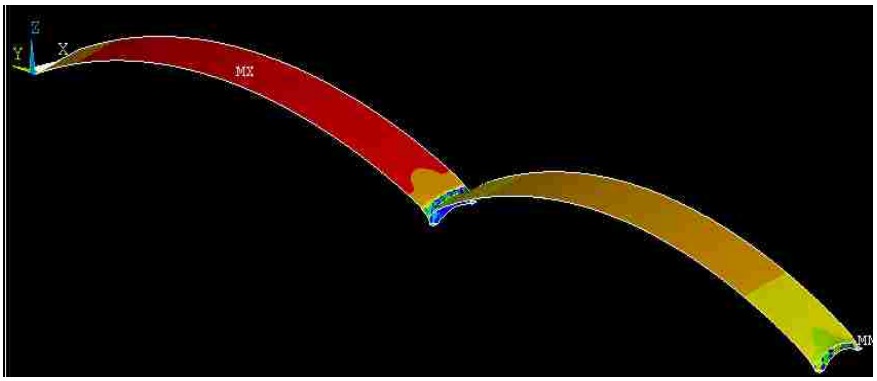

Figure 5-33 - Stress Distribution of Pressure Loaded Strip Model

According to the FM wind-uplift specifications, the edges of 3.66m (12ft) long membranes need to be clamped to the test platform. It is believed the lack of agreement could be attributed to insufficient distance between the area of interest and the actual edge. However, it is important to note that it is believed that this strip model could be more indicative of a full roof system installation as the length would be much larger than the width of the sheets, therefore allowing the symmetry boundary conditions to accurately capture the true behavior of a large surface. The topic of size discrepancies between testing and installation was discussed by Prevatt, *et al.* [64] in regards to necessary correction factors in order to compare the actions at different scales.

5.5 Results

Results for additional material property validation, as well as full scale uplift simulation, were collected in order to assess the robustness of the finite element

model. Findings included sufficient matching between real world and model results, as well as promise for the predictive power of the model.

5.5.1 Thickness Variation

As discussed previously in 5.1.2, a 5-parameter Mooney-Rivlin curve fit option was employed with the final equation given as:

$$W = C_{10}(\bar{I}_1 - 3) + C_{01}(\bar{I}_2 - 3) + C_{20}(\bar{I}_1 - 3)^2 + C_{11}(\bar{I}_1 - 3)(\bar{I}_2 - 3) + C_{02}(\bar{I}_2 - 3)^2 + \frac{1}{d}(J - 1)^2$$

E. 5.5

Which was obtained through expansion of E. 5.1. Since the strain energy is defined on a per unit volume basis [69], the constants will remain valid through thickness changes in the hyperelastic material. In order to validate this postulate, additional uniaxial tensile tests were performed with thicker roofing material corresponding to the company's 60mil and 80mil product lines. As seen in Figure 5-34 and Figure 5-35, good matching was found when comparing both the micro- and macro-scale models to the experimental results as seen in below for the 60- and 80mil products. Discrepancies between these results could be attributed to the lack of experimental tests performed due to the higher initial interest lying with the 45mil product line.

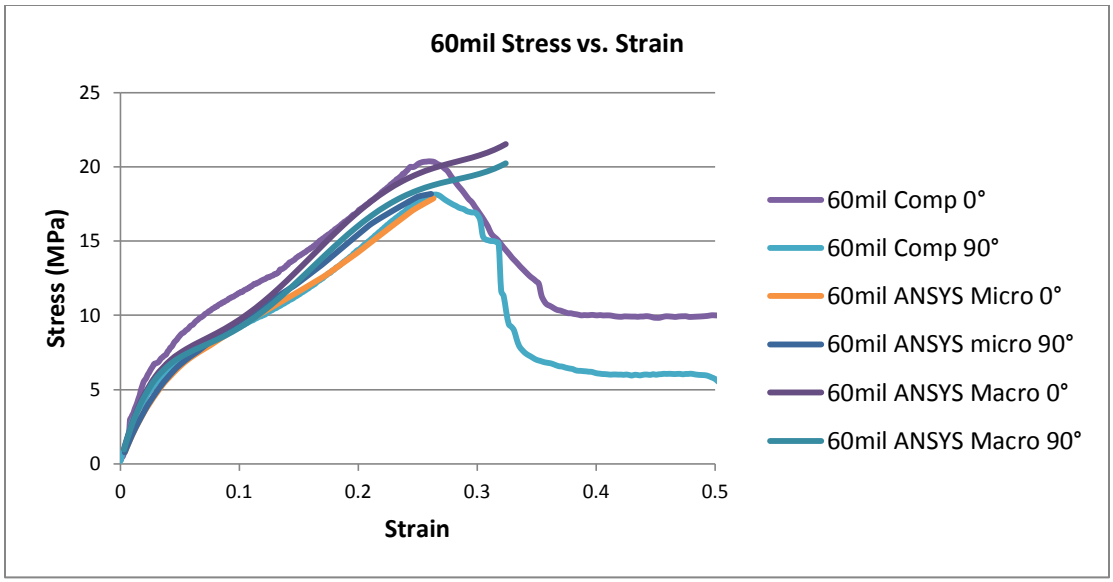

Figure 5-34 - Stress vs. Strain Comparison for 60mil MD (0°) and CMD (90°) Cut Tensile Specimens and Finite Element Results

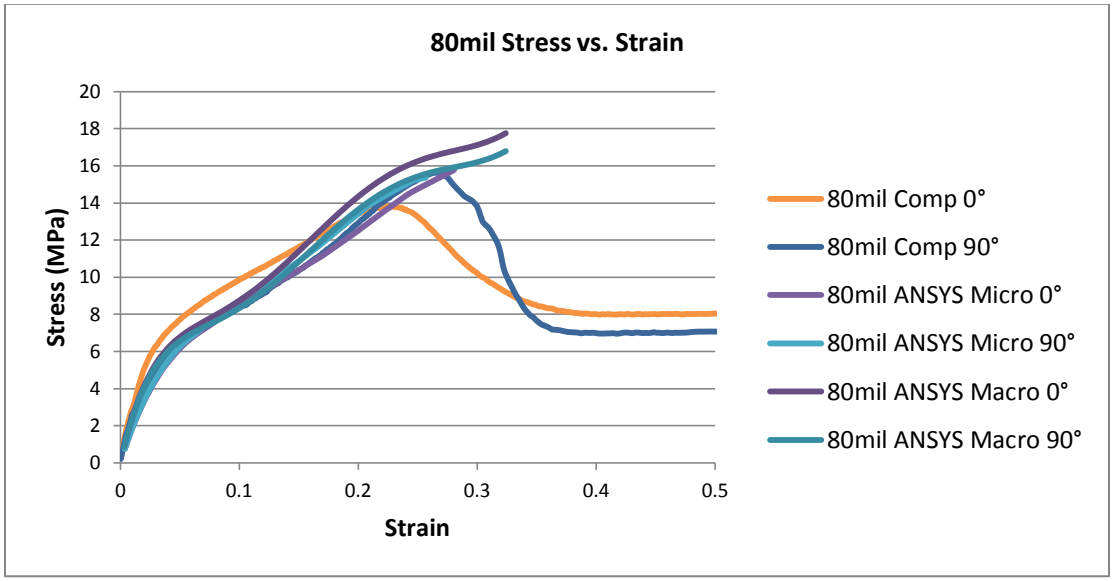

Figure 5-35 - Stress vs. Strain Comparison for 80mil MD (0°) and CMD (90°) Cut Tensile Specimens and Finite Element Results

Further validation for the success of the model taking thickness variation into account will be discussed in the next section where the wind uplift experimental test results are compared to the finite element model.

5.5.2 ANSI FM 4474 Results Comparison

A half-symmetry model was used in order to reduce the number of elements and computational requirements associated with this volume. The schematic for this model can be seen below in Figure 5-36 which is created in accordance with the manufacturer's installation specifications. A 457.2mm (18") spacing scenario was also examined in accordance with the investigative experiments performed by GAF. This spacing value could be used to reduce the installation cost and time if the performance can be upheld. This topic will be discussed further below.

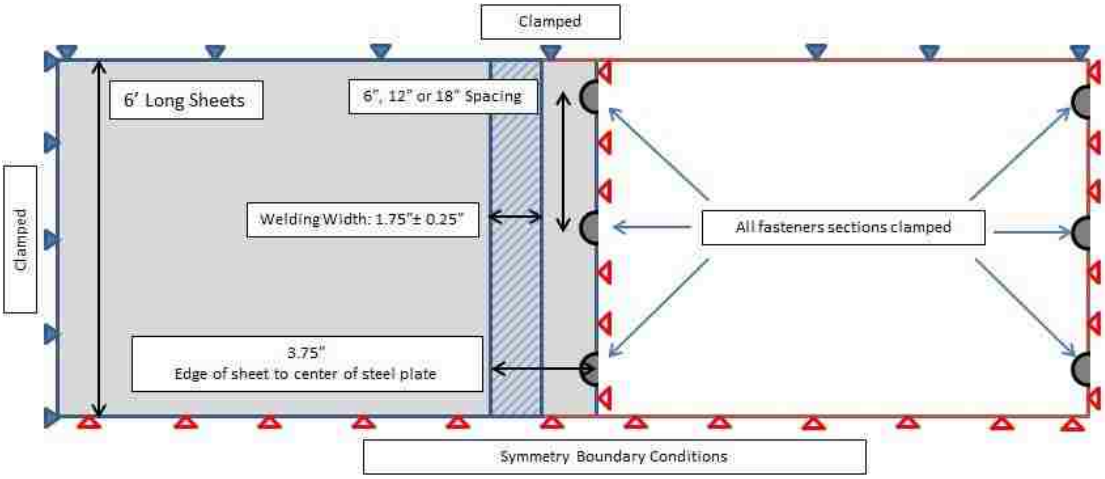

Figure 5-36 - Half Symmetry Roof System Schematic

In an ideal setting, a full 3D model with individual elements for each constituent and CZM related properties between each element in order to analyze the delamination failure associated with the seam failure would be used. Unfortunately this would be far too computationally intensive as discussed earlier. With the current model in mind, seam failure was assessed by gathering the internal reaction

forces of elements immediately neighboring the CZM area and comparing these values to the maximum allowable force values observed in the T-peel and shear seam tests mentioned above. This technique was employed in lieu of available delamination related stress data that could be provided by a fully 3D model.

In addition to this, stress distribution along the entire sheet was examined and, as expected, the maximum stresses of the composite did not reach anywhere near the maximum values observed in the tensile tests. A final failure mode was investigated near the steel plate fasteners in order to assess whether the pull-out failure scenarios would occur. Again, the forces in the elements surrounding the point of interest were examined in lieu of puncture data that would further complicate the model. Failure in the real world test scenarios has been observed to occur through membrane failure, plate rupture, or fastener pull-out, where the screw used to affix the steel plate to the roof deck experiences failure.

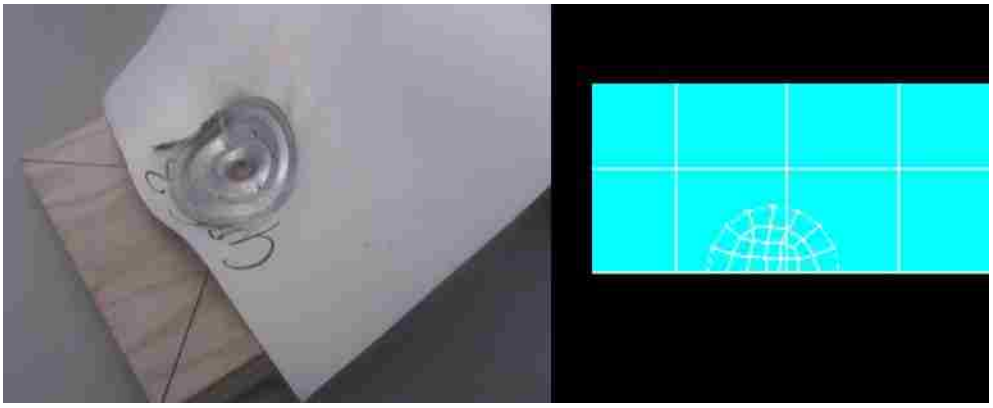

Figure 5-37 - Pull-Out Test Results (Left) Element Correlation (Right)

Good correlation between Finite Element simulation and FM wind-uplift test for the 45mil product was observed as seen in Table 3. The actual test procedure includes increasing the pressure every 718 Pa (15psf) and holding for one minute to check for failure. Since the actual model allows for the time-step analysis, more precise measurements can be captured for the pressure at which failure begins. This allows the discrepancies observed in the table below to be deemed satisfactory since they fall within the anticipated ranges.

Table 3 - Failure Point Comparisons between FM Wind Uplift and Simulations for 45mil Roofing Material

Fastener Size	Weight	Fastener Spacing	Weld Width	FM Rating	GAF Model Prediction (psf)	FM Failure Mode	Model Failure Mode
2 3/8"	45mil	6"	1.75"	1-105	112	Seam Delamination	Seam Delamination
2 3/8"	45mil	12"	1.75"	1-60	63	Plate Rupture	Failure Near Plate
2 3/8"	45mil	18"	1.75"	1-30	28	Failure Near Plate	Failure Near Plate
2 3/4"	45mil	6"	1.75"	1-120	115	Seam Delamination	Seam Delamination
2 3/4"	45mil	12"	1.75"	1-90	83	Failure Near Plate	Failure Near Plate
Benton	45mil	Benton	6"	1-105	120	Seam Delamination	Seam Delamination

The final entry in Table 3 is the Benton Bar where a 322.6mm (1”) wide, 0.762mm (30mil) thick piece of aluminum spans a 1.524m (5ft) long sheet in the same type of wind uplift scenario as previously discussed. This method is used to analyze the 152.4mm (6”) wide seams that are created using an adhesive based system, which results in a much lower seam peel strength. With the established values taken into

account, good agreement between the experimental and simulation results was observed.

As explored earlier, thickness variations were also simulated in order to compare to experimental results. Again, good correlation between the failure points was observed as seen in Table 4

Table 4 - Failure Point Comparisons between FM Wind Uplift and Simulations for 60mil Roofing Material

Fastener Size	Weight	Fastener Spacing	Weld Width	FM Rating	GAF Model Prediction (psf)	FM Failure Mode	Model Failure Mode
2 3/8"	60mil	6"	1.75"	1-120	120	Seam Delamination	Seam Delamination
2 3/4"	60mil	12"	1.75"	1-90	102	Plate Rupture	Failure Near Plate
2 3/4"	60mil	18"	1.75"	1-45	40	Plate Rupture	Failure Near Plate

5.5.3 Theoretical Changes

Simulation results using alternate spacing showed promise, but construction methods deny the ability to explore many of these possibilities. Additional items that were examined include wider heat welds, a different seam creation method involving adhesive tape, and changes in polymer and fiber material properties. Of these alternatives, only the adhesive tape seam creation was accompanied by known physical data. Results below in Table 5 are compared to the standard 44.45mm (1.75”) weld created with heat rolling. Due to the lower peel strength, the adhesive based seams exhibited much lower failure points.

Table 5- Additional Failure Comparisons 45mil Roofing Material

Fastener Size	Fastener Spacing	Weld Width	GAF Model Prediction (psf)	Model Failure Mode	Comparison	Notes
2 3/8"	6"	4"	84	Seam Delamination	-28	*20lbf data for T-peel
2 3/8"	12"	4"	57	Failure Near Plate	-6	
2 3/8"	6"	6"	84	Seam Delamination	-28	*20lbf data for T-peel
2 3/8"	12"	6"	57	Failure Near Plate	-6	

Failure analysis for the remaining items was difficult to perform as experimental data for many of these circumstances is not yet available. Instead, assumptions used will be noted as failure points were based on other known values. Comparisons between standard material properties of the corresponding spacing can be seen in Table 6 and Table 7. In these tables, the percent increases refer to changes in the strength of the TPO and/or fiber as compared to the original 45mil material properties.

Table 6 - 6" Spacing Comparisons to Theoretical Changes

Fastener Size	Fastener Spacing	Weld Width	GAF Model Prediction (psf)	Model Failure Mode	Comparison	Notes
2 3/8"	6"	1.75"	109	Both Failures at Same Point	-3	1300 Denier Fiber *Used 60mil Pull-out data 45mil seam strength
2 3/8"	6"	1.75"	115	Failure Near Plate	3	Fiber -25%
2 3/8"	6"	1.75"	120	Pass	8	TPO +25% *use failure data for 60mil
2 3/8"	6"	1.75"	114	Seam Delamination	2	TPO -25%
2 3/8"	6"	1.75"	120	Pass	8	TPO/Fiber +25% *Use Failure data for 60mil

Table 7- 12" Spacing Comparisons to Theoretical Changes

Fastener Size	Fastener Spacing	Weld Width	GAF Model Prediction (psf)	Model Failure Mode	Comparison	Notes
2 3/8"	12"	1.75"	77	Both Failures at Same Point	14	1300 Denier Fiber *Used 60mil Pull-out data 45mil seam strength
2 3/8"	12"	1.75"	82	Failure Near Plate	19	Fiber +25% *Used 60mil Pull-Out data
2 3/8"	12"	1.75"	83	Failure Near Plate	20	Fiber -25%
2 3/8"	12"	1.75"	84	Failure Near Plate	21	TPO +25% *use failure data for 60mil
2 3/8"	12"	1.75"	82	Failure Near Plate	19	TPO -25%
2 3/8"	12"	1.75"	67	Failure Near Plate	4	TPO/Fiber +25% *Use Failure data for 60mil

Pending additional verification of alternate design behaviors, it would appear that the fastener spacing and size have the greatest impact on the wind-uplift performance of the single-ply roofing system. To further verify this trend, additional theoretical simulations were performed based on ideas that were believed to have potential to improve the uplift performance.

Table 8 - Additional Theoretical Simulation Results

Fastener Size	Weight	Fastener Spacing	Weld Width	GAF Model Prediction (psf)	Model Failure Mode	Notes
2 3/8"	120mil	6"	1.75"	180	No Failure	Based on trend, Fastener pull-out assumed to be 800lbf
2 3/8"	120mil	12"	1.75"	85	Failure Near Plate	
2 3/8"	60mil	Benton	1.75"	180	No Failure	Found limits of 60mil seam
2 3/8"	45mil	6"	1.75"	68	Failure Near Plate	Double area in fastener/seam area
2 3/8"	45mil	12"	1.75"	30	Failure Near Plate	

The most interesting result found in Table 8 is the 60mil Benton test. As discussed earlier, the Benton test does not employ individual fasteners, but rather a continuous strip used to hold the edge of the membrane to the test deck. This

allows for failure analysis that concentrates on the seam strength of the system rather than the local failure that occurs near the fasteners. In this simulation, the 60mil product was able to withstand pressures much beyond the 5.75kPa (120psf) threshold that is desired and even past a loading level of 8.62kPa (180psf). This further validates the theory that the localized failure near the fasteners is the main area of concern.

The remaining items in Table 8 are based on changing the thickness of the membrane either locally near the fastener and seam area or globally with the overall material thickness increased to an estimated 120mil scenario. Although the 120mil simulation showed greatly improved wind uplift capability, failure criteria assumptions were based on current trends found in the increased thicknesses levels already established by GAF. This scenario would also greatly increase the material cost of covering such large roofing areas as are found in commercial applications. The local thickness model was based on affixing an additional 152.4mm (6”) wide strip along the edge of the current 45mil product, thereby doubling the effective thickness in the area highlighted in Figure 5-38.

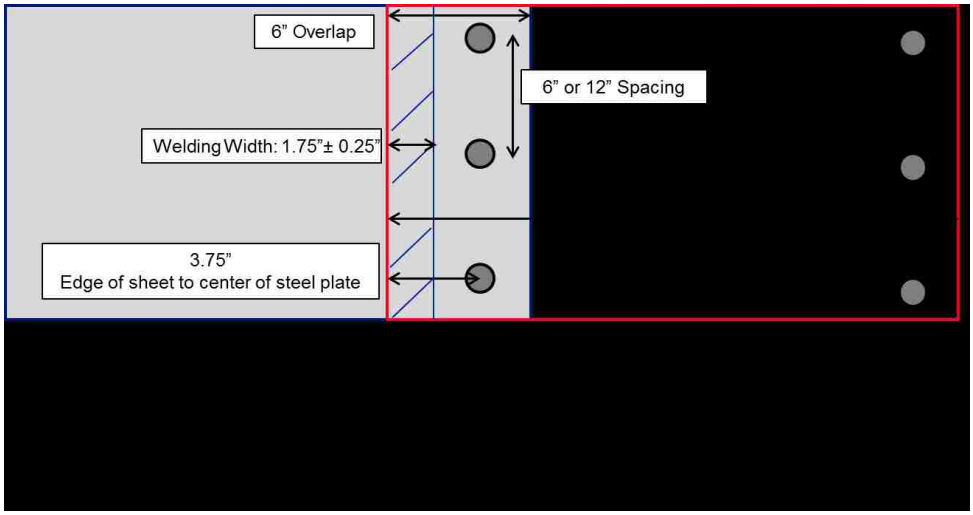

Figure 5-38 - Schematic of Double Thickness Area

Due to the sudden change in thickness and effective stiffness, this scenario resulted in a stress discontinuity at the transition point between the two different types of elements. This discontinuity is believed to be the cause of the much lower wind uplift performance.

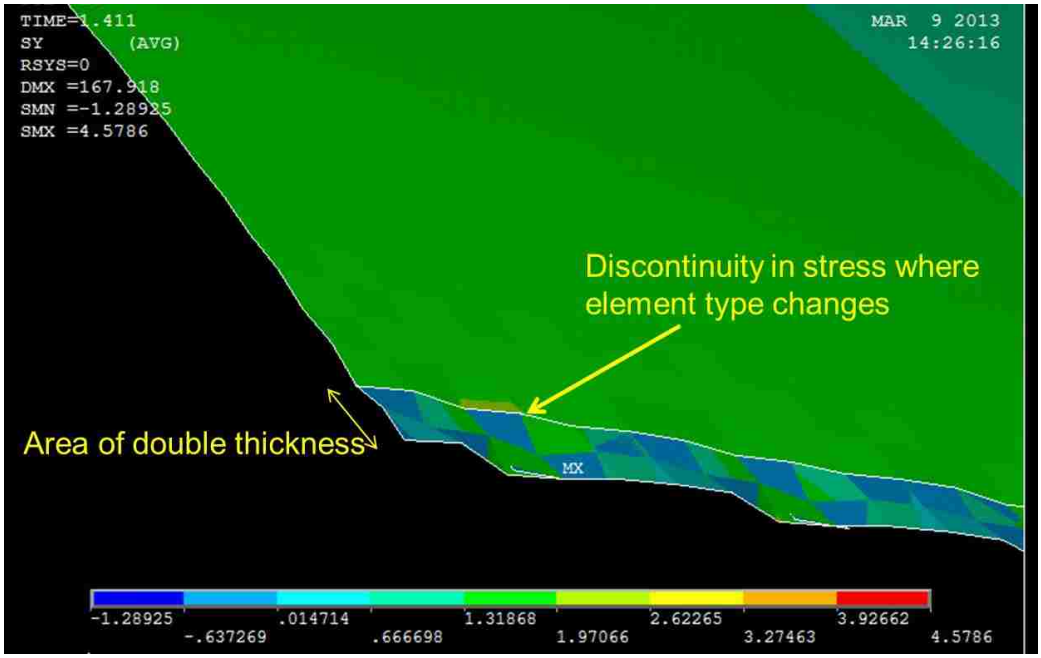

Figure 5-39 - Stress Discontinuity in Double Thickness Model

5.6 Discussion and Conclusion

As mentioned above, the failure near the fastener is the most prominent area that needs improvement. Based on the theoretical model results discussed above, localized changes in thickness near the fasteners will not help in improving the failure in this area, but rather will actually decrease the wind uplift performance as compared to the original arrangement. Since the material thickness changes will have a drastic impact on the cost associated with the roofing systems, examining changes in the fiber reinforcement materials, scrim geometry and thickness will be the recommended course of action for improving the wind uplift performance. If the larger spacing systems can provide the same performance as the closer spacing

systems, the installation and material costs associated with the roofing systems will decrease greatly.

Upon completion of the large scale finite element model the results and comparisons outlined in the previous sections show that a flexible composite simulation can be created much beyond the micro-scale fiber/yarn interaction models found in the literature. This scaling and successful implementation of predictive methods for the commercial roofing application results in a significant improvement in the standard tools implemented in the industry. Through the use of this type of modeling, additional adjustments and changes can be investigated before the creation of large prototypes that would be required to accurately test the effect any changes might have on the real world behavior. Significant improvement in construction material and installation techniques could also be achieved through the use of the predictive model developed.

References

[1] Callister Jr. W. D., 2003, Materials Science and Engineering: An Introduction, 6th Edition, John Wiley & Sons, Inc.

[2] Ramakrishna S., Ming Huang Z., and Yew H. M., 1999, "Development of a novel flexible composite material," Journal of Materials Processing Technology, **89-90**, pp. 473–477.

[3] Wu D. Y., Meure S., and Solomon D., 2008, "Self-healing polymeric materials: A review of recent developments," Progress in Polymer Science, **33**(5), pp. 479–522.

[4] Leong K. H., Ramakrishna S., Huang Z. M., and Bibo G. A., 2000, "The potential of knitting for engineering composites—a review," Composites Part A: Applied Science and Manufacturing, **31**(3), pp. 197–220.

[5] Ning H., Vaidya U., Janowski G. M., and Husman G., 2007, "Design, manufacture and analysis of a thermoplastic composite frame structure for mass transit," Composite Structures, **80**(1), pp. 105–116.

[6] Zinno A., Fusco E., Prota A., and Manfredi G., 2010, "Multiscale approach for the design of composite sandwich structures for train application," Composite Structures, **92**(9), pp. 2208–2219.

[7] Mamalis A. ., Robinson M., Manolakos D. E., Demosthenous G. A., Ioannidis M. B., and Carruthers J., 1997, "Crashworthy capability of composite material structures," Composite Structures, **37**(2), pp. 109–134.

[8] Ning H., Pillay S., and Vaidya U. K., 2009, "Design and development of thermoplastic composite roof door for mass transit bus," Materials & Design, **30**(4), pp. 983–991.

[9] Torre L., and Kenny J. ., 2000, "Impact testing and simulation of composite sandwich structures for civil transportation," Composite Structures, **50**(3), pp. 257–267.

[10] Schubel P. M., Luo J.-J., and Daniel I. M., 2007, "Impact and post impact behavior of composite sandwich panels," Composites Part A: Applied Science and Manufacturing, **38**(3), pp. 1051–1057.

[11] Choi I. H., 2006, "Contact force history analysis of composite sandwich plates subjected to low-velocity impact," Composite Structures, **75**(1-4), pp. 582–586.

[12] Foo C. C., Chai G. B., and Seah L. K., 2008, "A model to predict low-velocity impact response and damage in sandwich composites," Composites Science and Technology, **68**(6), pp. 1348–1356.

[13] Ghasemi Nejhad M. N., and Parvizi-Majidi A., 1990, "Impact behaviour and damage tolerance of woven carbon fibre-reinforced thermoplastic composites," Composites, **21**(2), pp. 155–168.

[14] Hebert M., Rousseau C.-E., and Shukla A., 2008, “Shock loading and drop weight impact response of glass reinforced polymer composites,” Composite Structures, **84**(3), pp. 199–208.

[15] Reyes G., and Sharma U., 2010, “Modeling and damage repair of woven thermoplastic composites subjected to low velocity impact,” Composite Structures, **92**(2), pp. 523–531.

[16] Winkel J. D., and Adams D. F., 1985, “Instrumented drop weight impact testing of cross-ply and fabric composites,” Composites, **16**(4), pp. 268–278.

[17] Atas C., and Sayman O., 2008, “An overall view on impact response of woven fabric composite plates,” Composite Structures, **82**(3), pp. 336–345.

[18] Chocron S., Anderson C. E., Samant K. R., Figueroa E., Nicholls A. E., and Walker J. D., 2010, “Measurement of strain in fabrics under ballistic impact using embedded nichrome wires, part II: Results and analysis,” International Journal of Impact Engineering, **37**(1), pp. 69–81.

[19] Cheeseman B. a., and Bogetti T. a., 2003, “Ballistic impact into fabric and compliant composite laminates,” Composite Structures, **61**(1-2), pp. 161–173.

[20] Nilakantan G., Keefe M., Wetzel E. D., Bogetti T. a., and Gillespie J. W., 2011, “Computational modeling of the probabilistic impact response of flexible fabrics,” Composite Structures, **93**(12), pp. 3163–3174.

[21] Roberts J. C., Merkle a C., Biermann P. J., Ward E. E., Carkhuff B. G., Cain R. P., and O’Connor J. V, 2007, “Computational and experimental models of the human torso for non-penetrating ballistic impact.,” Journal of biomechanics, **40**(1), pp. 125–36.

[22] Dhakal H. N., Zhang Z. Y., Richardson M. O. W., and Errajhi O. a. Z., 2007, “The low velocity impact response of non-woven hemp fibre reinforced unsaturated polyester composites,” Composite Structures, **81**(4), pp. 559–567.

[23] Bekisli B., and Nied H. F., 2010, “MECHANICAL PROPERTIES OF KNITTED-FABRIC REINFORCED ELASTOMERIC COMPOSITES,” Polymer Processing Society 26th Annual Meeting.

[24] Huysmans G., Verpoest I., and Van Houtte P., 2001, “A damage model for knitted fabric composites,” Composites Part A: Applied Science and Manufacturing, **32**(10), pp. 1465–1475.

[25] Takano N., Zako M., Fujitsu R., and Nishiyabu K., 2004, “Study on large deformation characteristics of knitted fabric reinforced thermoplastic composites at forming temperature by digital image-based strain measurement technique,” Composites Science and Technology, **64**(13-14), pp. 2153–2163.

[26] Cox B. N., and Davis J. B., 2001, “Knitted composites for energy absorption under tensile loading,” Composites Part A: Applied Science and Manufacturing, **32**(1), pp. 91–105.

[27] Gommers B., Verpoest I., and Van Houtte P., 1996, “Modelling the elastic properties of knitted-fabric-reinforced composites,” Composites Science and Technology, **56**(6), pp. 685–694.

[28] Huang Z. M., Ramakrishna S., and Tay a. a. O., 2000, “Modeling the stress/strain behavior of a knitted fabric-reinforced elastomer composite,” Composites Science and Technology, **60**(5), pp. 671–691.

[29] Miao Y., Zhou E., Wang Y., and Cheeseman B. a., 2008, “Mechanics of textile composites: Micro-geometry,” Composites Science and Technology, **68**(7-8), pp. 1671–1678.

[30] Lau K. W., and Dias T., 1994, “Knittability of High Modulus Yarns,” Journal of the Textile Institute, **85**(2), pp. 173–190.

[31] Philips D., Verpoest I., and Raemdonck J. Van, 1997, “Optimising the mechanical properties of 3d-knitted sandwich structures,” International Conference on Composite Materials, Queensland, pp. 201–210.

[32] Chou S., Chen H.-C., and Lai C.-C., 1992, “The fatigue properties of weft-knit fabric reinforced epoxy resin composites,” Composites Science and Technology, **45**(4), pp. 283–291.

[33] Andersson C. H., Christensson B., Wickberg A., and Pisanikovski T., 1996, “Handleability of Fibres, Machinability of Composites and the Working Environment,” European Conference on Composite Materials, London, pp. 415–420.

[34] Andersson C. H., Christensson B., Dartman T., and Krantz S., 1999, “DUST EMISSION AND STRENGTH LOSSES DUE TO HANDLING OF REINFORCEMENT FIBRES,” International Conference on Composite Materials, Paris.

[35] Aslan Z., Karakuzu R., and Okutan B., 2003, “The response of laminated composite plates under low-velocity impact loading,” Composite Structures, **59**(1), pp. 119–127.

[36] Aretxabaleta L., Aurrekoetxea J., Urrutibeascoa I., and Sánchez-Soto M., 2005, “Characterisation of the impact behaviour of polymer thermoplastics,” Polymer Testing, **24**(2), pp. 145–151.

[37] Richeton J., Ahzi S., Vecchio K. S., Jiang F. C., and Makradi a., 2007, “Modeling and validation of the large deformation inelastic response of amorphous polymers over a wide range of temperatures and strain rates,” International Journal of Solids and Structures, **44**(24), pp. 7938–7954.

[38] Cantwell W. J., and Morton J., 1991, “The impact resistance of composite materials — a review,” Composites, **22**(5), pp. 347–362.

[39] Liu Y., and Liaw B., 2009, “Drop-weight impact tests and finite element modeling of cast acrylic/aluminum plates,” Polymer Testing, **28**(8), pp. 808–823.

[40] Sayer M., Bektaş N. B., and Sayman O., 2010, “An experimental investigation on the impact behavior of hybrid composite plates,” Composite Structures, **92**(5), pp. 1256–1262.

[41] Tai N. ., Yip M. ., and Lin J. ., 1998, “Effects of low-energy impact on the fatigue behavior of carbon/epoxy composites,” Composites Science and Technology, **58**(1), pp. 1–8.

[42] Zhang Z. Y., and Richardson M. O. W., 2005, “Visualisation of barely visible impact damage in polymer matrix composites using an optical deformation and strain measurement system (ODSMS),” Composites Part A: Applied Science and Manufacturing, **36**(8), pp. 1073–1078.

[43] Hirai Y., Hamada H., and Kim J., 1998, “Impact response of woven glass-fabric composites—I.,” Composites Science and Technology, **58**(1), pp. 91–104.

[44] Stevanović M. M., and Stecenko T. B., 1992, “Mechanical behaviour of carbon and glass hybrid fibre reinforced polyester composites,” Journal of Materials Science, **27**(4), pp. 941–946.

[45] Tai N., 1999, “Effects of thickness on the fatigue-behavior of quasi-isotropic carbon/epoxy composites before and after low energy impacts,” Composites Science and Technology, **59**(11), pp. 1753–1762.

[46] “NDE/NDT Resource Center” [Online]. Available: http://www.ndt-ed.org.

[47] Shivakumar K. N., Elber W., and Illg W., 1985, “Prediction of Impact Force and Duration Due to Low-Velocity Impact on Circular Composite Laminates,” Journal of Applied Mechanics, **52**(3), p. 674.

[48] BEAUMONT P. W. R., RIEWALD P. G., and ZWEBEN C., “Methods for improving the impact resistance of composite materials,” ASTM special technical publication, (568), pp. 134–158.

[49] Evci C., and Gülgeç M., 2012, “An experimental investigation on the impact response of composite materials,” International Journal of Impact Engineering, **43**, pp. 40–51.

[50] Thomason J. L., 2009, “The influence of fibre length, diameter and concentration on the impact performance of long glass-fibre reinforced polyamide 6,6,” Composites Part A: Applied Science and Manufacturing, **40**(2), pp. 114–124.

[51] Thomason J. L., 1999, “The influence of fibre properties of the performance of glass-fibre-reinforced polyamide 6,6,” Composites Science and Technology, **59**(16), pp. 2315–2328.

[52] Sutherland L. S., and Guedes Soares C., 2004, “Effect of laminate thickness and of matrix resin on the impact of low fibre-volume, woven roving E-glass composites,” Composites Science and Technology, **64**(10-11), pp. 1691–1700.

[53] De Morais W. a., and D’Almeida J. R. M., 2005, “Effect of the laminate thickness on the composite strength to repeated low energy impacts,” Composite Structures, **70**(2), pp. 223–228.

[54] Jensen R., and Mcknight S., 2006, “Inorganic–organic fiber sizings for enhanced energy absorption in glass fiber-reinforced composites intended for structural applications,” Composites Science and Technology, **66**(3-4), pp. 509–521.

[55] Kim J.-K., and Mai Y., 1991, “High strength, high fracture toughness fibre composites with interface control—A review,” Composites Science and Technology, **41**(4), pp. 333–378.

[56] Bekisli B., 2010, “Analysis of Knitted Fabric Reinforced Flexible Composites and Applications in Thermoforming.”

[57] ANSYS Inc., “Release 13.0 Documentation for ANSYS.”

[58] Sadd M. H., 2005, Elasticity Theory, Applications, and Numerics, Elsevier Butterworth-Heinemann.

[59] Fung Y. C., and Tong P., 2001, Classical and Computational Solid Mechanics, World Scientific Publishing Co. Pte. Ltd.

[60] Barbero E. J., 2008, Finite Element Analysis of Composite Materials, CRC Press, Boca Raton, FL.

[61] Cheney W., and Kincaid D., 2008, Numerical Mathematics and Computing, Thomson Brooks/Cole.

[62] Yoganandan N., Zhang J., Pintar F. a, and King Liu Y., 2006, “Lightweight low-profile nine-accelerometer package to obtain head angular accelerations in short-duration impacts.,” Journal of biomechanics, **39**(7), pp. 1347–54.

[63] Taylor T. J., and Yang L.-Y. “Tammy”, 2010, “Physical Testing of Thermoplastic Polyolefin Mebranes and Seams,” Interface: Membranes, pp. 4–9.

[64] Prevatt D. O., Schiff S. D., Stamm J. S., and Kulkarni A. S., 2008, “Wind Uplift Behavior of Mechanically Attached Single-Ply Roofing Systems: The Need for Correction Factors in Standardized Tests,” Journal of Structural Engineering, **134**(3), pp. 489–498.

[65] Yang L.-Y. T. ., Xing L., and Taylor T., 2009, “A BRIGHT FUTURE – SINGLE PLY THERMOPLASTIC POLYOLEFIN ROOFING,” Society of Plastics Engineers Annual Technical Conference, pp. 1509–1515.

[66] Payne J., Nied H. F., and Yang L.-Y. “Tammy”, 2013, “MODELING of SINGLE PLY THERMOPLASTIC POLYOLEFIN ROOFING,” Society of Plastics Engineers Annual Technical Conference, pp. 2020–2024.

[67] Mooney M., 1940, “A Theory of Large Elastic Deformation,” Journal of Applied Physics, **11**(9), p. 582.

[68] Ogden R. W., 1972, “Large Deformation Isotropic Elasticity - On the Correlation of Theory and Experiment for Incompressible Rubberlike Solids,” Proceedings of the Royal Society A: Mathematical, Physical and Engineering Sciences, **326**(1567), pp. 565–584.

[69] Rivlin R. S., 1948, “Large Elastic Deformations of Isotropic Materials. IV. Further Developments of the General Theory,” Philosophical Transactions of the Royal Society A: Mathematical, Physical and Engineering Sciences, **241**(835), pp. 379–397.

Vita

Jeremy Payne is originally from Portville, NY where he graduated from Portville Central School. He is the son of Wendy Eaton and Jeffrey Payne and the stepson of John Eaton. Jeremy attended Youngstown State University in Youngstown, OH where he earned a Bachelor's of Engineering degree in Mechanical Engineering as a member of Youngstown State's University Scholars program. Also while at Youngstown, Jeremy worked for General Electric's Ohio Lamp Plant in Warren, OH. Jeremy was also very active in his fraternity Sigma Tau Gamma. Following graduation from Youngstown, he attended Lehigh University for his graduate studies. After completion of the Master of Science degree under Prof. Herman F. Nied, Jeremy continued his studies at Lehigh University in the PhD program in Mechanical Engineering, also under Prof. Nied. His current research interests are in the fields of finite element modeling, composite materials, and material testing.